PhD-FSTC-2017-22
The Faculty of Sciences, Technology and Communication

DISSERTATION

Defence held on 31/03/2017 in Luxembourg

to obtain the degree of

DOCTEUR DE L'UNIVERSITÉ DU LUXEMBOURG

EN SCIENCES DE L'INGÉNIEUR

by

Mohammad MOHSENI
Born on 16 December 1981 in Tehran (Iran)

DRYING AND CONVERSION ANALYSIS OF BIOMASS BY A DEM-CFD COUPLING APPROACH

Dissertation defence committee

Dr-Ing. Bernhard Peters, dissertation supervisor
Professor, Université du Luxembourg

Dr-Ing. Manfred Greger, Chairman
Professor, Université du Luxembourg

Dr-Ing. Michael Beckmann, Vice Chairman
Professor, Technische Universität Dresden

Dr. Algis Dziugys
Lithuanian Energy Institute

Dr. Amirhoushang Mahmoudi
Demcon Bunova Institute

UNIVERSITY OF LUXEMBOURG

Abstract

Faculty of Science, Technology and Communication
Engineering Department

Doctor of Philosophy

Drying and Conversion Analysis of Biomass by a DEM-CFD Coupling Approach

by Mohammad Mohseni

Biomass materials as a type of renewable energy sources have attracted many attention nowadays to decrease fossil fuel usage due to ecological and economical benefits. The main objective of this PhD thesis is studying the drying and conversion of biomass materials with employing a hybrid four-way DEM-CFD coupling approach in which considers the solid particulates as discrete elements coupled via heat, mass and momentum transfer to the surrounding gas as continuous phase. Where a comprehensive three-dimensional numerical model is developed and applied to investigate the complex phenomena taking place during biomass drying and conversion in a reactor. That is referred to take into account the physical and chemical processes as heat-up, drying, pyrolysis, gasification and combustion including the essential heterogeneous and homogeneous reactions which is considered as an interactive solid-gas multiphase system. In the proposed model, the motion and thermodynamic state of the particles are involved with employing the relevant governing equations. Where the conductive and radiative heat transfer between particles as well as convective heat transfer between particles and gas phase are taken into account. In addition, some interfaces are extended for coupling the solid particles and the gas phase to consider the interactions in between. At first, the importance of biomass resources is discussed and then the mathematical modeling employed in the PhD thesis is explained thoroughly. To apply the model, four different cases are assessed where two chapters discuss the drying behavior of biomass particles in two different situations. Afterwards, the motion of solid particles in a bubbling fluidized bed is examined. Finally, the conversion of wood materials in a bubbling fluidized bed is determined.

Acknowledgements

Here it is my opportunity to acknowledge all people who I have been working with during my PhD study at the University of Luxembourg in the past four years. First of all, I would like to thank my supervisor Prof. Bernhard Peters. It has been a great honor to be one of his PhD students in the research team Luxembourg Extended Discrete Element Method (LuXDEM). I appreciate all his contributions of time and thoughts to make my PhD valuable as well as for creating such a nice research environment in which I have been engaged with PhD students and postdocs who have influenced and enhanced my research project.

I am immensely grateful for the collaborations with Soil-Concept company established by Marc Demouling to give me an outstanding chance to do experimental works necessary for my thesis project. My particular gratefulness goes to Alex Kolomijtschuk as an instructive friend with giving practical skills during the experimental tests for the vibrating grate dryer case in the company. For this dissertation I would like to mainly thank my committee members Prof. Manfred Greger, Prof. Michael Beckmann and Dr. Algis Dziugys for their time and interest for reading my thesis as well as productive comments during the PhD defense.

My special thank goes to Amir Mahmoudi for effective discussions and aids during my doctoral study including friendly and intimate time having together. I am deeply thankful to Xavier Besseron for great IT support which was an essential point to cope with the project. Also I need to extremely appreciate my comrades Florian Hoffmann and Alvaro Estupinan for their compassionate tips and opinions which raised the quality of my work. I should distinctly thank my office mates Andrew Ignatenko and Yu-Chung Liao for being together for a long time warmly and cordially.

I highly admire the kermani couple Maryam and Mehdi Baniasadi for tight communications during the coffee breaks, social and common events. My huge gratitudes go to the members of LuXDEM team that I have had the pleasure to work with Gabriele Pozzetti, Edder Santana, Pascal Loew, Brice Kabore, Alban Rousset, Wahid Chekaraou and Mark Michael that have contributed largely to my personal and professional aspects at Luxembourg University through extraordinary cooperations and advices.

In regards to supporting my PhD thesis financially, I gratefully acknowledge the funding source, the Fonds National de la Recherche (FNR) in Luxembourg to make my PhD research feasible. Finally, I would like to strongly appreciate my family for all love, supports and encouragements during my living time from my childhood so far.

Contents

List of Figures

List of Tables

Abbreviations

CCDM	**C**ombined **C**ontinuum and **D**iscrete **M**odel
CFD	**C**omputational **F**luid **D**ynamics
CPP	**C**lean **P**ower **P**lan
DEM	**D**iscrete **E**lement **M**ethod
EIA	**E**nergy **I**nformation **A**dministration
IEO	**I**nternational **E**nergy **O**utlook
MC	**M**oisture **C**ontent
XDEM	e**X**tended **D**iscrete **E**lement **M**ethod
IFP	**I**nternational **F**uel **P**rices

Physical Constants

Individual Gas constant of Air	R	=	286.9 J/kg K
Universal Gas constant	R_u	=	8.314 J/mol K
Stefan-Boltzmann constant	σ	=	5.67×10^{-8} W/m^{2}K^4
Atmospheric pressure	p	=	1.013 bar

Symbols

A	pre-exponential factor	1/s
c	damping coefficient	Ns/m
c_p	specific heat capacity at constant pressure	J/kgK
d_p	particle diameter	m
D	Diffusion coefficient	m^2/s
e	restitution coefficient	-
E	Activation energy	J/mol
E	Young's modulus	N/m^2
F	force	N
g	gravity	m/s^2
G	Shear modulus	N/m^2
h	specific enthalpy	J/kg
H	enthalpy	J/mol
I	moment of inertia	J/kg
k	spring stiffness	N/m
K	permeability	m^2
K_i	reaction rate constant for specie i	1/s
l	length	m
L_v	specific latent heat of evaporation	J/kg
m	mass	kg
$\dot{m}$	mass flow rate	kg/s
p	pressure	Pa
Pr	Prandtl number	-
$\dot{q}$	heat flux	W/m^2
r	radius; radial coordinate	m

Re	Reynolds number	-
$S_{a,char}$	internal surface area of char	m^2
t	time	s
T	temperature	K
$\mathbf{T}$	torque	Nm
$\mathbf{v}$	velocity	m/s
V	volume	m^3
$\dot{w}$	reaction rate	mol/s
X	moisture content	g water/g dry solid

Greek Symbols

δ	differential operator	-
Δ	difference	-
α	heat transfer coefficient	W/m^2K
β	mass transfer coefficient	m/s
ε	porosity	-
λ	thermal conductivity	W/mK
μ	dynamic viscosity	kg/ms
$\boldsymbol{\mu}$	friction coefficient	-
ν	kinematic viscosity	m^2/s
ρ	density	kg/m^3
τ	tortuosity	-
$\boldsymbol{\tau}'$	viscous stress tensor	Pa
ω	angular velocity	rad/s
γ	partition coefficient	-

Subscripts

D	drag
f	fluid
fp	fluid-particle interaction
l	liquid
g	gas
i	specie i

ij	effective
n	normal
p	particle
s	solid
R	radius
t	tangential
0	initial value

To Mother

Chapter 1

Introduction

1.1 Background and Motivation

Fossil fuels such as oil, coal and natural gas are effective energy resources that have fulfilled the world energy demands suitably in the last centuries. Although, the main issue particularly in the recent decades is that fossil fuel resources deliver high carbon dioxide emission which leads to global warming. In addition, fossil fuels are ending in the near future since they are significantly limited. Therefore, replacing fossil fuels has been a controversial issue in the world recently. In this case, the alternative resources as solar energy, wind energy, geothermal energy, hydrogen and biomass could be the remedy to overcome this issue. The latter is concern of this thesis where the most important privilege of biomass is renewability. This means they can be reproduced in a short time which makes it a great source for energy production compared to the fossil fuels that take millions of years to develop.

Thereby, using biomass as a renewable energy source is attracting more attention nowadays because of global warming and fossil fuel depletion. This is evidenced based on the published statistics in International Energy Outlook 2016 through the growth rate of renewable energy consumption shown in fig.1.1. However, due to initial moisture content of biomass, drying process prior to conversion leads to increase reactor efficiency, improve system operation and better produced gas quality. Hence, it is of major importance to remove the moisture content in beforehand. In general, biomass materials are initially wet containing moisture content of $25 - 65$ %. For the systems needing clean gases to run engines as it is the concern of this research, it is required to reach the moisture content of materials around 10 % for raising the quality of biofuel produced in the gasifying reactor. The most commercial biomass as renewable energy source is forestry or agricultural residues. Based on the biomass material type and properties,

the bulk density could be between $50 - 500\ kg/m^3$. Anyhow, the difficulty of moisture removal from biomass is affected by several factors such as initial moisture content and size distribution.

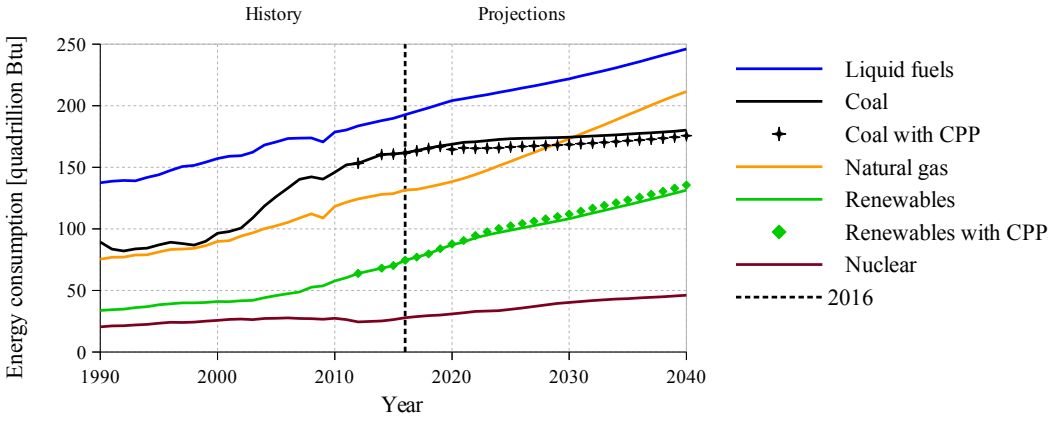

FIGURE 1.1: World energy consumption by energy source, 1990-2040 (International Energy Outlook 2016, EIA)

The first biomass gasification investigation was carried out by Thomas Shirley in 1659 that discovered gas from coal mine. During 1850-1940 the gas made from coal was used mainly for lighting homes and streets and for heating. Between 1975-2000 gasification has been used commercially in chemical feedstock production which traditionally came from petroleum. Since 2000, because of global warming, instability in oil production and price, gasification has been drawing more attention as a natural choice for conversion of renewable *carbon-neutral* biomass into gas. To highlight the importance of biomass usage as energy source, it is stated that among the vast amount of available biomass, only 5% (13.5 billion metric tons) can be potentially mobilized to produce energy. This quantity is still large enough to provide about 26% of the world's energy consumption, which is equivalent to 6 billion tons of oil (IFP, 2007). [1]

However, the bulky and inconvenient form of biomass is a major barrier to a rapid shift from fossil to biomass fuels. Unlike gas or liquid, biomass cannot be handled, stored, or transported easily. This provides a great motivation for the conversion of solid biomass into gaseous fuels, which can be achieved through biochemical (fermentation) and thermochemical (pyrolysis, combustion, gasification) processes. The former is not concern of this study. In a nutshell, combustion involves high-temperature conversion of biomass in excess air into carbon dioxide and steam, while gasification includes a chemical reaction in an oxygen-deficient environment. Also pyrolysis takes place at a relatively low temperature in the total absence of oxygen. Regarding the global warming concerns, biomass has no net contribution to CO_2 emission to the atmosphere. This is explained as in biomass production, carbon dioxide is absorbed by the plants for

photosynthesis while during burning it is released to atmosphere. Thus, according to statistics published in IEO2016 [2], it could be stated that the net release of CO_2 via biomass conversion is considered as zero [1]. Where fig.1.2 demonstrates the rate of yearly carbon dioxide release by fuel type which is exclusively from fossil fuels.

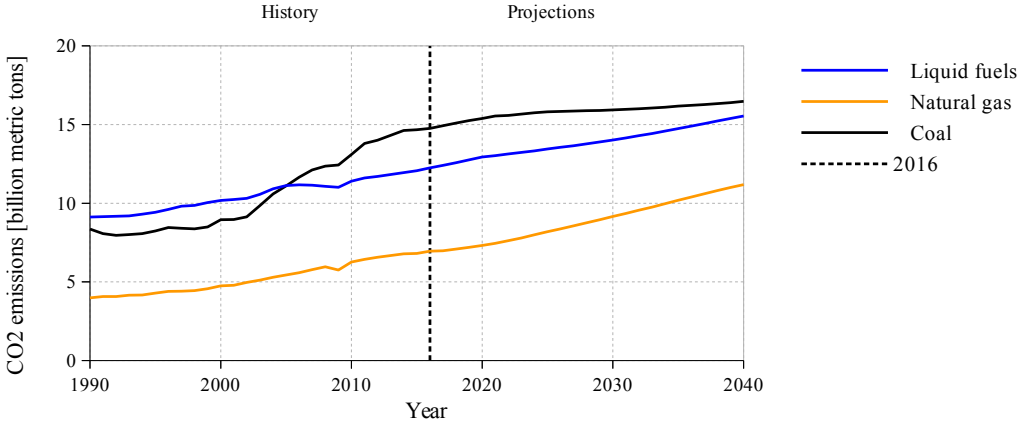

FIGURE 1.2: World energy-related carbon dioxide emissions by fuel type, 1990-2040 (International Energy Outlook 2016, EIA)

On the other hand, conversion of biomass into usable energy sources represents a vital method of reducing fossil fuel dependence and greenhouse gas emission. The low levels of impurities in biomass leads to lower SO_x and NO_x emission during conversion and thus reduced contribution to acid rain [3]. More reasons that biomass is being used increasingly as a clean energy are ecological and economic advantages. Basically, three types of primary fuels that could be produced from biomass are noted as *I) liquid* fuels like ethanol and methanol; *II) gaseous* fuels like CH_4, CO_2, CO, H_2; and *III) solid* fuel like char. From these, four significant categories of yields are produced from conversion of various types of biomass as waste and low-price resources shown in fig.1.3.

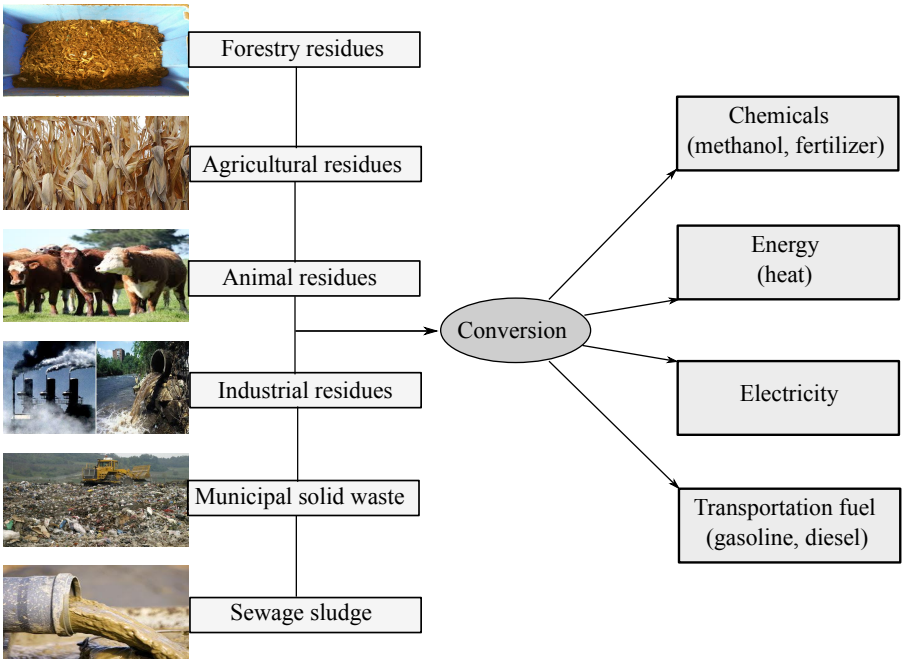

FIGURE 1.3: Biomass resources (left) conversion to different products (right)

1.2 Outline of the Thesis

The objective of this thesis is to present a comprehensive numerical model to simulate multiphase systems including solid-gas phase to describe the physical and chemical processes, particularly drying and conversion of biomass fuel. The goal is to improve the efficiency of the considered apparatus. That is to say, investigating how to optimize the dryer and gasifying reactor to reach the desired amount of final moisture content as well as better quality of the produced gas fuel. This requires to control the accomplished operations according to the defined input parameters which are investigated in this thesis. To fulfill this scope, a four-way DEM-CFD approach is presented where the solid particles are considered as discrete elements coupled to the surrounding gas phase via determined interfaces. Where the coupling includes heat, mass, momentum and species transfer between biomass solid particles and continuous gas phase.

1.3 Structure of the thesis

- Chapter 2: The theoretical modeling of DEM-CFD coupling approach including the governing equations related to solid-gas phase are discussed. Where the interfaces as heat, mass, momentum and species transfer are presented.
- Chapter 3: Using the implemented DEM-CFD model, drying analysis of biomass particles in a rotary dryer is investigated, and the influence of surface area between particles and gas flow on drying process is studied.
- Chapter 4: To complement the previous chapter, drying of biomass particulates on a vibrating fluidized bed dryer in industrial scale is experimentally and numerically predicted. The goal is optimizing the facility to reach the favorable final moisture content with suitable residence time through adjusting the input parameters of dryer.
- Chapter 5: The purpose of this chapter is hydrodynamics analysis of spherical particles in a bubbling fluidized bed with cold flow injection experimentally and numerically. The aim is to investigate the effect of various input parameters on the minimum fluidization velocity of the bed.
- Chapter 6: With applying the DEM-CFD method, conversion of solid biomass involving complex processes in a bubbling fluidized bed is studied. Where the main intention is verifying the behavior of multiphase solid-gas system inside the reactor during conversion and evaluating the produced gas species.
- Chapter 7: At last, the total conclusion of the thesis including the outcomes is presented in this chapter.

Chapter 2

eXtended Discrete Element Method

2.1 Introduction

Since the experiment is highly effortful and costly to realize the complex processes in the multiphase flow systems, a full scale numerical simulation is desired to investigate the solid-gas behavior. In multiphase systems where the particles interact with fluid flow, there are two approaches to describe the behavior of different phases as Eulerian and Lagrangian. The Eulerian approach considers the flow as continuous while the Lagrangian approach tracks the properties of each particle as it traverses in the flow [4]. Apart from compatibility of Eulerian approach for fluid flow, employing this approach for solid phase leads to miss particulates properties during simulation which decreases the accuracy of results.

Recent advances in computational capabilities have given rise to a wide variety of modeling strategies to model granular flows. Among the available modeling approaches, the most widely used are the two fluid model (TFM) and the DEM-CFD coupling method. The TFM ([5] [6] [7]) is an Eulerian-Eulerian approach where both solid and fluid phases are considered to be two distinct interpenetrating continua. This approach is suitable for modeling large industrial scale gasifiers with low to moderate resolution of the flow field. On the other hand, DEM-CFD is a high fidelity Lagrangian-Eulerian approach which tracks each individual particle, providing a much better flow field resolution compared to TFM. However, this approach is more suited for small lab scale simulations as it is restricted by the computational expense. [8]

In both approaches, depending on the treatment of the fluid-particle and particle-particle interactions, the numerical methods can be categorized as one-way coupling (fluid-to-particle action only), two-way force coupling (fluid-particle mutual interactions) [9], and four-way coupling (fluid-particle interactions and particle-particle collisions) [10]. The latter is considered in this thesis where the mathematical modeling is based on DEM-CFD coupling and it is named eXtended Discrete Element Method (XDEM). The substantial advantage of XDEM is resolving the continuous fluid phase with Eulerian approach with employing OpenFOAM tool, while Lagrangian approach is implemented to track each entity of the granular material. Fig.2.1 describes the schematic DEM-CFD coupling modules that are explained in the next sections.

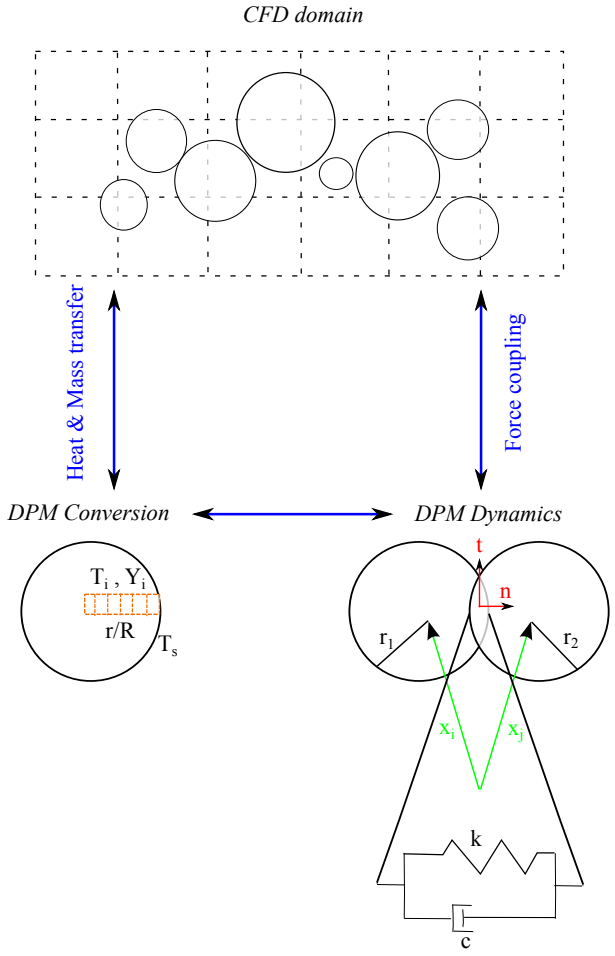

FIGURE 2.1: Schematic DEM-CFD modules

In the present approach, the interaction between solid-gas phase as heat, mass, momentum and species transfer is modeled. This advanced numerical method in multiphysics systems treats the dynamics of particulates with using the classical discrete element method originally proposed by Cundal and Strack [11], in addition to include the thermodynamic state of each particle such as temperature and interior species. The latter

is mentioned as the unique privilege of this approach rather than other DEM-CFD methods. The behavior of fluid continuous phase via employing OpenFOAM as computational fluid dynamics (CFD) tool is coupled to the discrete phase to make a robust and reliable tool to deal with many physical and chemical applications in industry such as heating-up, drying, pyrolysis, combustion and gasification. The interface is referred to mutual heat, mass, momentum and species transfer between the granular materials and the fluid flow. This means the particulates are considered as heat and mass sources inside the continuous gas phase. The gas properties in the particle region are then transferred from CFD to DEM and the resulting heat and mass sources are transferred back to CFD.

In this DEM-CFD coupling module, all processes inside each particle is described by one-dimensional and transient conservation equations which is accurate enough based on Man [12]. With summing up individual particle processes, the total process is established for the packed bed of particles. The arrangement of particles within the surrounding gas is expressed as void space. In this case, the flow through the void space of the packed bed is modeled as the flow through a porous medium with considering the interaction between the solid-gas phase by heat, mass, momentum and species transfer [13]. In other words, in multiphase flows to investigate the effect of solid material in the fluid flow, the porous media concept is employed. Porous medium by definition is a material involving a solid matrix with an interconnected void so that the solid matrix could be either rigid (the usual situation) or it sustains small deformation. The interconnectedness of the void spaces allow the fluid to flow through the material in which by a single fluid (gas or liquid) is called single-phase flow or with both liquid and gas sharing the void space is named two-phase flow. But the shape and size of pores are irregular in the porous medium. [14]

Basically, in porous media the continuum mechanics deals with transition from the molecular scale to the micro-scale (pore-scale) to resolve the flow in pore spaces. This is done by replacing the molecular properties by averaged properties over a large number of molecules. That is, instead of each molecule, the overall fluid flow is considered with averaged fluid properties such as density and viscosity. In addition, in the fluid mechanics a continuum needs to be considered at the macro-scale. To fulfill the transition from micro-scale to macro-scale, the micro-scale is expressed as a grid cell including porous structure. In this case, the micro-scale properties are averaged over a representative elementary volume (REV) to obtain a macro-scale description of the system so that the effective parameters are porosity and intrinsic permeability. Fig.2.2 shows the volume averaging transition from micro-scale to macro-scale as well as porous structure thereby the DEM-CFD approach in this study is based on.

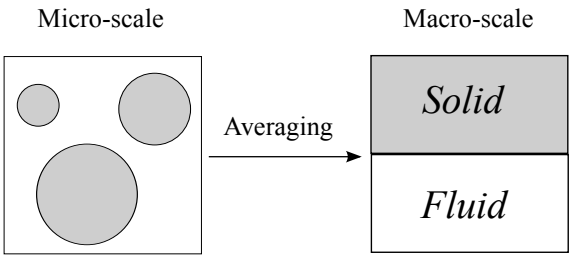

FIGURE 2.2: Volume averaging from micro-scale to macro-scale in a typical 2D cell

Generally speaking, many studies have implemented hybrid DEM-CFD model to simulate dynamics ([8] [15] [5] [10]) and conversion ([9] [16]) behavior of particulates in various kinds of fluidized beds. In spite of the fact that the motion of particles are described by Newtonian equations and gas phase is resolved by Navier-Stokes equations. The Newtonian equations of motion are solved for each particle in a Lagrangian framework and the coupling force between fluid and particles is then related to the particles velocity relative to the locally averaged fluid velocity, and to the local concentration of the particle assembly [5]. Furthermore, Sakai et al. in [17] [18] has studied gas-solid two phase flow in a fluidized bed chamber with employing a DEM-CFD algorithm for grain particles. The minimum fluidization velocity is evaluated based on comparing the bed expansion and pressure drop as a function of the superficial gas velocity. This procedure is employed in Chapter5 as the base criteria. Moreover, Aibing Yu team in [19] [20] [21] [22] has worked on DEM-CFD approach to study the fundamentals of different particle-fluid flow systems of granular materials in different kinds of fluidized beds. In addition, Kuipers group has developed a Eulerian-Lagrangian model in [23] [24] [25] to predict mesoscale particle structures under different flow conditions. The proposed model is used in [26] for coupled heat and mass transfer in a spout fluidized bed with liquid injection.

Thus, in the following sections the intention is describing the DEM-CFD approach through defining three major modules as solid dynamics and conversion, as well as fluid flow governing equations where the mathematical modeling as a unified method is applied in Chapters 3, 4, 5 and 6 in various case studies. The interfaces between solid-gas phase are also explained throughly where required and all utilized variables and constants are introduced particularly.

2.2 Dynamics of Solid Elements

For granular materials, the particulate properties and interaction laws play an important role to predict the motion of particles in the system. In order to solve the equations of motion for a system of interacting particles, two different strategies can be used to resolve the particle-particle collisions as soft sphere and hard sphere approaches. The soft sphere approach considers the multiple particle interactions where a packed bed of particles is involved in the system. While the hard sphere technique is based on the momentum change on physical basis and only accounts for binary collisions which is suitable for diluted particle laden flows. Discrete element method is based on the soft sphere model which is applied in this thesis where each collision is modeled according to the overlap between two particles. A particular pair of particles in collision has a normal and tangential linear spring and dash-pot arrangement (see fig.2.1). Where the collision impact forces generated due to the overlap are calculated based on nonlinear Hertz-Mindlin model in this thesis. The reason is in contrast to the linear models such as spring-dashpot model, the spring stiffness is estimated according to the material properties in each time step to realize the collision properly. In this model a spring governs the deflection of the particle after collision, whereas the dashpot dissipates the energy of the particle, thus giving rise to inelastic collisions. In the tangential direction an additional sliding element is in series with the spring mass damper. The slider allows the particles to slide against each other limiting the maximum magnitude of the tangential force. [8]

2.2.1 Particle Motion

The interaction between particles is described by kinetic theory of the granular flow which is based on the kinetic gas theory. In the multiphase systems including solid-gas phase like fluidized beds, there exist two regions with low and high porosity. In the low porosity systems the frictional forces are dominant while in high porosity systems the collisional impacts are prevailing. According to Newton's second law, the motion of each particle as translational and rotational are defined as:

$$m_i \frac{d\vec{\mathbf{v}}_{p,i}}{dt} = \vec{\mathbf{F}}_{c,i} + \vec{\mathbf{F}}_{fp,i} + m_i \vec{\mathbf{g}} \tag{2.1}$$

$$I_i \frac{d\vec{\omega}_i}{dt} = \vec{\mathbf{T}}_i \tag{2.2}$$

where i denotes each particle; m_i and I_i are mass and moment of inertia; $\overrightarrow{\mathbf{v}}_{p,i}$ and $\overrightarrow{\omega}_i$ are particle velocity and angular velocity; $\overrightarrow{\mathbf{F}}_{c,i}$, $\overrightarrow{\mathbf{F}}_{fp,i}$, $m_i\overrightarrow{\mathbf{g}}$ and $\overrightarrow{\mathbf{T}}_i$ are contact force between particle-particle and particle-wall, drag force acting on particles by gas flow, gravitational force and torque acting on particles by tangential component of impact force, respectively. In order to calculate the impact inter-particle force which could be decomposed into tangential and normal components ($\overrightarrow{\mathbf{F}}_{c,i} = F_n\overrightarrow{\mathbf{n}} + F_t\overrightarrow{\mathbf{t}}$), there are various models such as linear and non-linear models. In linear contact models, a linear repulsive and a linear dissipative force is included except volume and dissipation where the spring stiffness coefficient is constant. The more realistic models are non-linear contact models in which considers dissipation and calculated spring stiffness coefficient such as Hertz-Mindlin model which is implemented in this work.

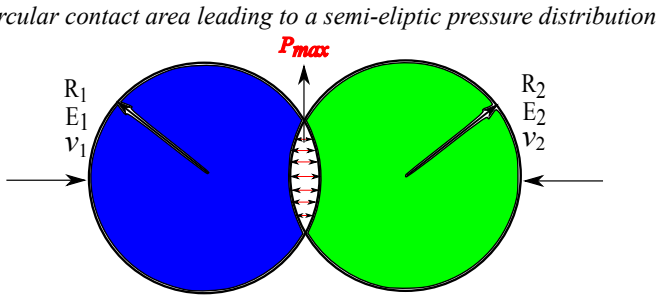

FIGURE 2.3: Graphical contact between two spheres

When two particles collide (fig.2.3), the interaction force is calculated according to the overlap between them. The overlap δ between two colliding particles is calculated according to their radius and positions as:

$$\delta = (r_i + r_j) - (\overrightarrow{\mathbf{x}}_i - \overrightarrow{\mathbf{x}}_j)\overrightarrow{\mathbf{n}} \tag{2.3}$$

In non-linear Hertz-Mindlin model, the normal contact force F_n is calculated based on the Hertz theory [27] to model the normal elastic force and the normal energy dissipation is evaluated according to the Mindlin theory [28].

$$F_n = m_{ij}\ \ddot{\delta} = -\left(c_n\ \delta^{\frac{1}{4}}\dot{\delta} + k_n\ \delta^{\frac{3}{2}}\right) \tag{2.4}$$

Where m_{ij}, E_{ij} and R_{ij} are effective mass, Young's modulus and radius belonging to a pair of contacting two particles. Also $\dot{\delta}$, k_n and c_n are relative velocity in normal direction, normal spring stiffness and viscous damping coefficient in normal direction based on Tsuji [29] and Zhang [30].

$$\dot{\delta} = (v_j - v_i).\overrightarrow{\mathbf{n}} \tag{2.5}$$

$$k_n = \frac{4}{3} E_{ij} \sqrt{R_{ij}} \tag{2.6}$$

$$c_n = ln\ e\ \sqrt{\frac{5 m_{ij} k_n}{\pi^2 + ln\ e^2}} \tag{2.7}$$

And e is the restitution coefficient that quantifies the ratio of relative velocities after and before the collision. In the absence of no damping, an energy balance equation is written between the start of the collision and an arbitrary point during the contact as [28]:

$$\frac{1}{2} m_{ij}\ \dot{\delta}_0^2 = \frac{1}{2} m_{ij}\ \dot{\delta}^2 + \frac{2}{5} k_n\ \delta^{\frac{5}{2}} \tag{2.8}$$

The maximum overlap happens when the relative velocity $\dot{\delta}$ is zero and therefore can be derived from the energy balance equation as [28]:

$$\delta_{max} = 1.09 \left(\frac{m_{ij}}{k_n}\right)^{\frac{2}{5}}\ \dot{\delta}_0^{\frac{4}{5}} \tag{2.9}$$

The behavior of particle during contact is analogized as a damped harmonic oscillatory motion so that the total contact time can also be derived from the energy balance (Eq.2.8) in no damping status. This can be done by integrating the time of contact over the loading and unloading phases explained in Eq.2.10 [28]. It is of major importance to evaluate contact time before implementing DEM so that the dynamics time step must be smaller than the estimated contact time otherwise it leads to instability in the system.

$$t_{contact} = 2 \int_0^{\delta_{max}} \frac{\partial \delta}{\dot{\delta}} = 2 \int_0^{\delta_{max}} \frac{\partial \delta}{\sqrt{\dot{\delta}_0^2 - \frac{4 k_n}{5 m_{ij}} \delta^{\frac{5}{2}}}} = 3.21 \left(\frac{m_{ij}^2}{k_n^2 \dot{\delta}_0}\right)^{\frac{1}{5}} \tag{2.10}$$

Also the tangential contact force which is a function of static and dynamic friction is written as:

$$F_t = min(k_t\delta_t + c_t\dot{\delta},\ \mu F_n) \tag{2.11}$$

where δ_t is the tangential displacement or slip, k_t is the tangential stiffness, G_{ij} is the effective shear modulus and c_t is the tangential dissipation coefficient.

$$k_t = 8G_{ij}\sqrt{R_{ij}\delta} \tag{2.12}$$

$$\frac{1}{G_{ij}} = \frac{2-v_i}{G_i} + \frac{2-v_j}{G_j} \tag{2.13}$$

$$c_t = ln\ e\ \sqrt{\frac{5(4m_{ij}k_t)}{6(\pi^2 + ln\ e^2)}} \tag{2.14}$$

In DEM to capture and resolve correctly the collisions between particles in the simulation, a suitable dynamics time step is required. In this thesis, the critical time step for inter-particle collision proposed by Tsuji et al. [31] and used in [8] is introduced in Eq.2.15 where ς denotes a constant defined based on the restitution coefficient. Thus, the critical time step for particles collision in this work is calculated as 4.5×10^{-4}, and for better accuracy the time step of 1×10^{-5} is taken into account.

$$\begin{cases} \Delta t_{cr} = \dfrac{\pi}{\sqrt{\frac{k_n(1-\varsigma^2)}{m_{ij}}}} \\ \varsigma = \dfrac{-ln(e)}{\sqrt{\pi^2 + ln(e)^2}} \end{cases} \tag{2.15}$$

Moreover, in each time step after calculating the total force and then acceleration according to Newton's second law, the particles velocities and positions are estimated step by step as follows in which in this work the Velocity-Verlet scheme (explained in [28]) is employed.

$$acceleration \longrightarrow velocity \longrightarrow position \tag{2.16}$$

Then, according to the particles positions in each time step, the porosity ε of each computational cell is calculated. Afterwards with solving the mass and momentum equations in the gas phase, the velocity and pressure fields are estimated. This procedure is repeated in each time step until the end of simulation as described in the algorithm below.

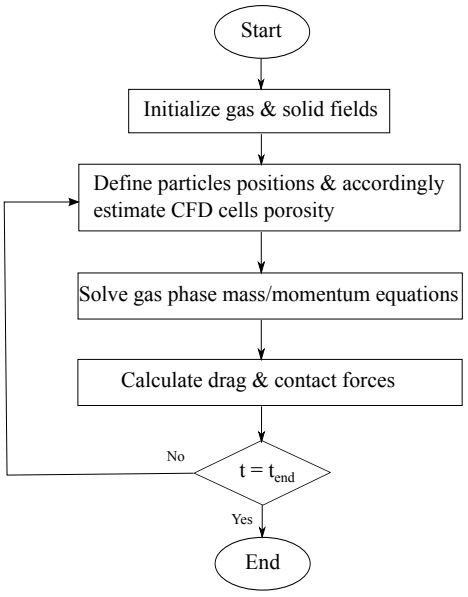

FIGURE 2.4: DEM-CFD algorithm

2.3 Conversion of Solid Elements

In order to describe the gas behavior within pore spaces of granular materials, the conservation equation of mass, momentum, energy and species are discussed in this section.

2.3.1 Continuity equation

Mass transfer of gas species through the pores of solid material is based on continuity equation with considering solid volume fraction according to the porous media basis. Where ε_p, ρ_f, $\mathbf{v}_f$ and S_{mass} denote particle porosity, gas density, gas velocity and mass source, respectively. The latter refers to interface for mass transfer of gas species between discrete-continuous phases. The variable r is defined based on different domains as an infinite plate ($n = 0$), an infinite cylinder ($n = 1$) and a sphere ($n = 2$) which is suitable for this work since spherical woody particles are employed.

$$\frac{\partial}{\partial t}\left(\varepsilon_p\langle\rho_f\rangle\right)+\frac{1}{r^n}\frac{\delta(r^n\varepsilon_p\langle\rho_f\rangle\langle\overrightarrow{\mathbf{v}}_f\rangle)}{\delta r}=S_{mass} \tag{2.17}$$

2.3.2 Momentum equation

To consider gas species transport through the pores of solid material, the Darcy law [32] is implemented where Eq.2.18 shows the conservation equation of linear momentum for compressible gas flow within porous media where K^* and μ_f are gas permeability and viscosity.

$$\frac{\varepsilon_p\mu_f}{K^*}\langle\overrightarrow{\mathbf{v}_f}\rangle=-\frac{\delta(\varepsilon_p p)}{\delta r} \tag{2.18}$$

2.3.3 Energy equation

The first law of thermodynamics states that energy cannot be created or destroyed but can be transformed from one form to another or transferred as heat or work. Eq.2.19 illustrates the energy conservation equation of solid phase where the impact of gas phase is neglected since the specific capacity of gas is far lower than solid specific capacity ($c_{p,g} \ll c_{p,s}$). Thermal equilibrium between gas-solid phases is assumed in energy conservation equation [33]. λ_{eff} is the effective thermal conductivity [34] and the last RHS term represents the enthalpy from reaction rate of species i ($i = 1...k$).

$$\frac{\delta\langle\rho c_p T\rangle}{\delta t}=\frac{1}{r^n}\frac{\delta}{\delta r}\left(r^n\lambda_{eff}\frac{\delta\langle T\rangle}{\delta r}\right)+\sum_{i=1}^{k}\dot{w}_i H_i \tag{2.19}$$

$$\lambda_{eff}=\varepsilon_p\lambda_g+\eta\lambda_{solid}+(1-\eta)\lambda_{char}+\lambda_{rad} \tag{2.20}$$

$$\lambda_{rad}=\frac{4\varepsilon_p}{1-\varepsilon_p}\sigma T^3 \tag{2.21}$$

2.3.4 Species equation

The species transport within the pore spaces of particles (Eq.2.22) is defined as conservation equation of each specie (i) transfer in time and space between solid-gas phases during drying process [35].

$$\frac{\delta Y_{i,f}}{\delta t}+\frac{1}{r^n}\frac{\delta(r^n Y_{i,f}\langle\overrightarrow{\mathbf{v}}_f\rangle)}{\delta r}=\frac{1}{r^n}\frac{\delta}{\delta r}\left(r^n D_{i,eff}\frac{\delta\langle Y_{i,f}\rangle}{\delta r}\right)+\dot{w}_{i,f} \tag{2.22}$$

$D_{i,eff}$, D_i, $Y_{i,f}$. τ and $\dot{w}_{i,f}$ are effective diffusion coefficient, molecular diffusion coefficient of i species, species (i) concentration, tortuosity and species reaction rate as a source term.

$$D_{i,eff} = D_i \frac{\varepsilon_p}{\tau} \tag{2.23}$$

2.3.5 Boundary conditions

Eq.2.24-2.23 denote the required boundary conditions implemented in this work so that further details are mentioned in [36].

$$-\lambda_{eff} \frac{\delta \langle T \rangle}{\delta r}\Big|_{r=0} = 0 \tag{2.24}$$

$$-\lambda_{eff} \frac{\delta \langle T \rangle}{\delta r}\Big|_{r=R} = \alpha(T_R - T_\infty) + \dot{q}_{rad} + \dot{q}_{cond} \tag{2.25}$$

$$-D_{i,eff} \frac{\delta \langle c_i \rangle}{\delta r}\Big|_{r=R} = \beta_i \big(c_{i,R} - c_{i,\infty}\big) \tag{2.26}$$

$$\alpha = \frac{\dot{m}_g \; c_{p,g}}{exp\big(\dot{m}_g \; c_{p,g}/\alpha_0\big) - 1} \tag{2.27}$$

$$\beta = \frac{\dot{m}_g/\rho_g}{exp\big(\dot{m}_g/\rho_g \beta_0\big) - 1} \tag{2.28}$$

2.4 Computational Fluid Dynamics

In computational fluid dynamics the fluid flow is described by a set of conservation equations of mass, momentum, energy and species that are discussed in this section. The continuous gas flow field containing a bed of particles is characterized as a type of porous media in which fluid flow behaves more like an external flow. And the governing equations of the fluid flow are described by implementing porous media into conservation equations as proposed in Faghri and Zhang [4]. The finite volume method is used to discretize the equations on a structured mesh and all variables are stored in the cell centers which means collocated grid is used. [10]

The flow could be accurately described for a continuum approach by averaging relevant variables and parameters on a coarser level. Hence, although the solid particles are

considered as a separate phase, but fluid flow in the bed is treated as one homogeneous continuum. For this reason macroscopic governing equations are obtained from the corresponding microscopic equations through an averaging process over a representative elementary volume (REV). For a given system three characteristic length scales are introduced:

(i) a macroscopic length scale l_{mac} for the global system

(ii) a representative elementary volume length scale l_{REV} related to the dimension of this volume

(iii) a microscopic length scale l_{mic} representative of the pore space

For any real porous flow it holds $l_{mic} \ll l_{REV} \ll l_{mac}$ and in that case the medium is considered homogeneous within one REV. Hence this approach for multiphase systems is extended to obtain the formulation for porous media [13] thereby the compressible conservation equations of the gas phase introduced here is based on Faghri and Zhang. [4]

2.4.1 Continuity equation

The continuity equation generally states that the rate of change of the density in a fluid element is equal to the net flow of mass through its boundaries wherein the effect of porosity ε_f is considered as a multiplying factor (Eq.2.29). The first term refers to the compressible flow when the density of a fluid element changes in time.

$$\frac{\partial}{\partial t}\left(\varepsilon_f \langle \rho_f \rangle\right) + \nabla.\left(\varepsilon_f \langle \rho_f \rangle \langle \overrightarrow{\mathbf{v}}_f \rangle\right) = S_{mass} \tag{2.29}$$

2.4.2 Momentum equation

By applying the Newton's second law to a fluid element, the Navier-Stokes equations can be derived to describe the momentum transfer of fluid flow. Eq.2.33 is the momentum equation of gas flow within porous media as particles so that the pressure gradient (∇p) is explained according to Darcy-Forchheimer relations [4] [37] where K^* and C are intrinsic permeability and passability coefficient obtained from empirical relations. This equation deals with the fixed bed of particles.

$$\frac{\partial}{\partial t}\left(\varepsilon_f\langle\rho_f\rangle\langle\overrightarrow{\mathbf{v}}_f\rangle\right)+\nabla.\left(\varepsilon_f\langle\rho_f\rangle\langle\overrightarrow{\mathbf{v}_f}\overrightarrow{\mathbf{v}_f}\rangle\right)=\nabla.\left(\varepsilon_f\langle\overrightarrow{\boldsymbol{\tau}'_f}\rangle\right)-\frac{\mu_f\ \varepsilon_f^2}{K^*}\langle\overrightarrow{\mathbf{v}_f}\rangle-\frac{\varepsilon_f^3\ \langle\rho_f\rangle}{C}\ |\langle\overrightarrow{\mathbf{v}_f}\rangle|\ \langle\overrightarrow{\mathbf{v}_f}\rangle \tag{2.30}$$

$$K^*=\frac{d_p^2\varepsilon_f^3}{150(1-\varepsilon_f)^2}\quad[4] \tag{2.31}$$

$$C=\frac{d_p\varepsilon_f^3}{1.75(1-\varepsilon_f)}\quad[4] \tag{2.32}$$

On the other hand, when the particles are moving with the gas flow motion, this equation changes based on the momentum coupling between solid-gas phase. That is calculating the fluid drag force acting on the particles. Thus, instead of defining pressure gradient term (∇p) according to Darcy-Forchheimer, the equation is altered as:

$$\frac{\partial}{\partial t}\left(\varepsilon_f\langle\rho_f\rangle\langle\overrightarrow{\mathbf{v}}_f\rangle\right)+\nabla.\left(\varepsilon_f\langle\rho_f\rangle\langle\overrightarrow{\mathbf{v}_f}\overrightarrow{\mathbf{v}_f}\rangle\right)=-\nabla p+\nabla.\left(\varepsilon_f\langle\overrightarrow{\boldsymbol{\tau}'_f}\rangle\right)-\overrightarrow{\mathbf{F}}_{fp} \tag{2.33}$$

The last term ($\overrightarrow{\mathbf{F}}_{fp}$) refers to the drag force caused by gas flow acting on the particles which is the solid-fluid interaction coupling force explained as follows.

2.4.2.1 Drag force definition

The last term in the momentum equation $\overrightarrow{\mathbf{F}}_{fp}$ refers to the solid-fluid interaction force which implies drag force influence on particles [10] specified as:

$$\overrightarrow{\mathbf{F}}_{fp}=\sum_{i=1}^{N_c}\frac{\varepsilon_f\mathbf{f}_{d,i}}{V_c} \tag{2.34}$$

where c and i are cell and particle index; N_c and V_c are number of cells and cell volume; and $\mathbf{f}_{d,i}$ denotes the drag force applied on each particle in the cell which is correlated to the particle and fluid velocities [10]:

$$\mathbf{f}_{d,i}=B_i(\overrightarrow{\mathbf{v}}_{fi}-\overrightarrow{\mathbf{v}}_{pi}) \tag{2.35}$$

In order to predict the interactive drag force between the particles and the surrounding fluid phase, many studies have concentrated to calculate the interfacial momentum exchange or the drag correlation B_i with developing different methods. The Gidaspow model is reported as the best fitted approach in [38] via investigating through various methods compared to experimental data. The reason that Gidaspow model [39] has employed successfully in many works is it includes both high and low porosity regions due to the fact that the void fraction has great influence on the drag force calculation. The Gidaspow drag model is a combination of Ergun equation and Wen-Yu model. The Ergun equation is related to the dense beds and considers the drag force as pressure drop through porous media. On the other hand, the Wen-Yu model observes the high porosity regions when the viscous forces are dominant. While the first part of the the Ergun equation describes low Reynolds number, the second part explains high Reynolds number flow.

$$B_i = \begin{cases} 150\mu \dfrac{(1-\varepsilon)^2}{\varepsilon\ d_{pi}^2} + 1.75(1-\varepsilon)\ \dfrac{\rho}{d_{pi}} |\overrightarrow{\mathbf{v}}_{fi} - \overrightarrow{\mathbf{v}}_{pi}| & \text{for } \varepsilon \leq 0.8 \quad (Ergun) \\ \dfrac{3}{4}\rho\ C_D\ \dfrac{\varepsilon(1-\varepsilon)}{d_{pi}} |\overrightarrow{\mathbf{v}}_{fi} - \overrightarrow{\mathbf{v}}_{pi}|\ \varepsilon^{-2.7} & \text{for } \varepsilon > 0.8 \quad (Wen-Yu) \end{cases} \tag{2.36}$$

And the particle drag coefficient depending on the particle Reynolds number is expressed as:

$$C_D = \begin{cases} \dfrac{24}{\varepsilon\ Re_{pi}} \Big[1 + 0.15(\varepsilon\ Re_{pi})^{0.687}\Big] & \text{for } Re_{pi} < 1000 \\ 0.44 & \text{for } Re_{pi} \geq 1000 \end{cases} \tag{2.37}$$

$$Re_{pi} = \frac{\varepsilon\ \rho\ d_{pi}}{\mu} |\overrightarrow{\mathbf{v}}_{fi} - \overrightarrow{\mathbf{v}}_{pi}| \tag{2.38}$$

2.4.3 Energy equation

Heat transfer can be defined as the transmission of energy from one region to another as a result of a temperature difference between them. Eq.2.39 denotes the energy conservation equation of gas flow in porous media estimated through volume averaging of the relevant gas and solid energy equations. The last term is the energy source term $(\sum_{i=1}^{k} \dot{w}_i H_i)$ that refers to the heat transfer interface between discrete-continuous phases.

$$\frac{\partial}{\partial t}\left(\varepsilon_f\langle\rho_f\rangle\langle h_f\rangle\right)+\nabla.\left(\varepsilon_f\langle\rho_f\rangle\langle\overrightarrow{\mathbf{v}}_f h_f\rangle\right)=\frac{\partial\langle p_f\rangle}{\partial t}+\varepsilon_f\ \langle\overrightarrow{\mathbf{v}}_f\rangle.\nabla\langle p_f\rangle+\sum_{i=1}^{k}\dot{w}_i H_i \tag{2.39}$$

2.4.4 Species equation

Eq.2.40 indicates the species transfer in the fluid flow within the porous media. The intensity of species mass exchange between discrete-continuous phases is defined as a source term $\dot{w}_{i,f}$ in the species equation of gas flow in porous media. The latter is the interface between solid-gas phase used in both energy and species equations. It is defined as the reaction rate related to existent species which is described in the next sections.

$$\frac{\partial}{\partial t}\left(\varepsilon_f\langle\rho_{f,i}\rangle\right)+\nabla.\left(\varepsilon_f\langle\rho_{f,i}\rangle\langle\overrightarrow{\mathbf{v}}_f\rangle\right)=\dot{w}_{i,f} \tag{2.40}$$

2.4.4.1 Drying

Basically, when biomass fuels enter to the reactor like fluidized beds, they face with the hot flow that leads to take place various physical and chemical processes simultaneously. They are mentioned as drying, devolatilization, combustion and gasification. This section describes the drying rate while the next sections evaluates the rate of devolatilization, combustion and gasification reactions. In order to estimate the drying rate, there are three approaches as heat sink model, first order kinetic evaporation rate and equilibrium model. In this work a heat sink model is used, in which more heat available above the saturation temperature T_{sat} is consumed for evaporation of moisture content of the solid particles. Eq.2.41 calculates the drying rate where the saturation temperature (T_{sat}) is predicted based on particle operating pressure (P) defined in Eq.2.42 as an empirical correlation function.

$$\dot{w}_{H_2O}=\begin{cases}\dfrac{\rho_g\ C_p(T-T_{sat})}{H_{sat}\ \delta t}, & \text{for } T\geq T_{sat}\\ 0 & \text{for } T<T_{sat}\end{cases} \tag{2.41}$$

$$T_{sat}=342.473+36.4857(P/10^5)-6.5274(P/10^5)^2+0.5056(P/10^5)^3 \tag{2.42}$$

In this model, the particle containing water is heated from the initial temperature T_0 and pressure P_0. The initial phase of the water is called sub-cooled liquid. The heat is

added to the water and it boils at saturation temperature based on P_0 and the water will be in saturated liquid state. Additional heat causes the liquid to vaporize at constant temperature so that the particle will contain both liquid and vapor which is called a saturated mixture. When all water vaporizes at T_{sat}, the vapor is called a saturated vapor. If more heat is added at this point, the temperature will start to increase producing superheated vapor until reaching the steam temperature [36]. In this thesis for all case studies, since the system is carried out at ambient pressure, the saturation temperature is estimated $100°C$ so that below this temperature no drying occurs. Thus, the heat-up process is neglected since the focus is drying, and thereby the particles are initiated at temperature $95°C$.

2.4.4.2 Pyrolysis

After finishing the water content of the particles inside the reactor, with increasing heat to reach the solid temperature around $380°C$, the particles commence to decompose to char, tar and volatiles which are defined as three different reactions shown bellow. By definition, pyrolysis is thermochemical decomposition of biomass into useful products where large complex hydrocarbon molecules of biomass are broken down into smaller and simpler molecules. The quality of products depends on several factors such as the reactor design, biomass characteristics, pyrolysis temperature, residence time and heating rate. Tab.2.1 introduces the decomposition reactions which take place through heterogeneous reactions in the solid phase. Where α_i are the mass fractions of the volatile species taken from D. Blasi [40] listed in tab.2.3. Generally, in the gasifying reactor after drying process, pyrolysis is a crucial pre-step reaction prior to combustion and gasification.

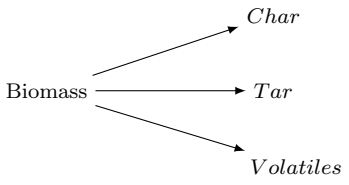

2.4.4.3 Combustion/Gasification

The volatile matters released from devolatilization process react with existing oxygen in the system and produce required heat for the endothermic reactions. The *homogeneous* reactions in tab.2.1 are employed in this work for modeling combustion of volatiles. Moreover, the released char is also combusted and gasified according to the *heterogeneous* reactions in tab.2.1. Where all reaction rates are presented in tab.2.2 and the reaction rate constant is calculated based on Arrhenius form ($K_i = A_i\ exp(E_i/RT)$). To describe

the turbulence/chemistry interaction, the Partially Stirred Reactor concept (PaSR) is applied which is explained in app.A.1. That is, in addition to considering heat, mass and momentum transfer in the system, the kinetics of reactions (in tab.2.4) is involved to evaluate produced char, tar and volatile matters at any operating condition. It is assumed that involved gases in all processes are ideal gas and nitrogen as an inert has no contribution in the chemical reactions. Regarding the char combustion reaction (No.9 in tab.2.1), the value of the partition coefficient (γ) depends on the temperature inside the system and lies between 1-2 so that the defined expression below is commonly used in [41] [42] [16] where T_p is the surface temperature of char at any operating time.

$$\gamma = \frac{2(1 + 4.3\ exp(-3390/T_p)}{2 + 4.3\ exp(-3390/T_p)} \tag{2.43}$$

Generally, under similar conditions, combustion reactions are faster than gasification reactions. Another important difference between char gasification and combustion reactions in a reactor is that during gasification the temperature of the char particle is nearly the same as the bed temperature because of simultaneous exothermic and endothermic reactions on it. In combustion, the char particle temperature can be much hotter than the bed temperature [1]. The rate of char combustion and gasification are calculated according to Evan and Emmons [43], which are based on partial pressure of the oxidizing and gasifying agent within the particle.

TABLE 2.1: Stoichiometric equations of pyrolysis, combustion and gasification for modeling thermal conversion of wood

Reaction No.	*Reaction definition*
Pyrolysis reactions:	
1	$Wood \rightarrow Char$
2	$Wood \rightarrow Tar$
3	$Wood \rightarrow \alpha_1\ CH_4 + \alpha_2\ CO + \alpha_3\ CO_2 + \alpha_4\ H_2 + \alpha_5\ H_2O$
Homogeneous reactions:	
4 – *CO combustion*	$2CO + O_2 \rightarrow 2CO_2$
5 – CH_4 *combustion*	$CH_4 + 2\ O2 \rightarrow CO_2 + 2\ H_2O$
6 – H_2 *combustion*	$2H_2 + O_2 \rightarrow 2H_2O$
7 – *Tar combustion*	$Tar + 2.9O_2 \rightarrow 6CO + 3.1H_2$
Heterogeneous reactions:	
8 – *Char combustion*	$\gamma C(s) + O_2 \rightarrow 2(\gamma - 1)CO + (2 - \gamma)CO_2$
9 – *Steam gasification*	$C(s) + H_2O \rightarrow CO + H_2$
10 – *Boudouard*	$C(s) + CO2 \rightarrow 2CO$

TABLE 2.2: Reaction rate estimation

Reaction No.	$\dot{w}_i =$	*Ref.*
1	$\frac{\delta \rho_{wood}}{\delta t} = K_1\ \rho_{wood}$	
2	$\frac{\delta \rho_{wood}}{\delta t} = K_2\ \rho_{wood}$	
3	$\frac{\delta \rho_{wood}}{\delta t} = K_3\ \rho_{wood}$	
4	$\frac{\delta [CO]}{\delta t} = K_5\ [CO]\ [O_2]^{0.25}\ [H_2O]^{0.5}$	
5	$\frac{\delta [CH_4]}{\delta t} = K_6\ [CH_4]^{0.7}\ [O_2]^{0.8}$	
6	$\frac{\delta [H_2]}{\delta t} = K_7\ [H_2]\ [O_2]$	
7	$\frac{\delta [tar]}{\delta t} = K_8\ T\ [tar]^{0.5}\ [O_2]$	
8	$\frac{\delta \rho_{O_2}}{\delta t} = K_9\ P_{O_2}\ S_{a,char}$	[43]
9	$\frac{\delta \rho_{CO_2}}{\delta t} = K_{10}\ P_{CO_2}\ S_{a,char}$	[43]
10	$\frac{\delta \rho_{H_2O}}{\delta t} = K_{11}\ P_{H_2O}\ S_{a,char}$	[43]

TABLE 2.3: Volatiles mass fraction of the pyrolysis reaction No.3

	CH_4	CO	CO_2	H_2	H_2O
α_i [44]	0.031	0.156	0.271	0.021	0.521

TABLE 2.4: Reactions kinetic data to calculate K_i

Reac No.	**A**	**E**(kj/mol)	**ΔH**(kj/kg)	*Ref.*
1	$3.27\ \times 10^{6}$	111.7	-418	[44]
2	$1.08\ \times 10^{10}$	148	-418	[44]
3	$4.38\ \times 10^{9}$	152.7	-418	[44]
4	$2.24\ \times 10^{12}$	167.36	10110	[45]
5	$11.58\ \times 10^{13}$	202.5	50187	[45]
6	$2.19\ \times 10^{9}$	109.2	120900	[45]
7	$9.2\ \times 10^{6}$	80.2	17473	[46]
8	$2.54\ \times 10^{-3}$	74.8	*Change with* γ	[43]
9	$1.81\ \times 10^{-2}$	130	-14370	[43]
10	$1.81\ \times 10^{-2}$	130	-10940	[43]

2.4.5 Boundary conditions

Eq.2.44-2.46 are the boundary equations used to complete the formulation of the conservation equations in the gas phase.

$$-K\frac{\partial\langle T\rangle}{\partial r}\Big|_{wall} = 0 \tag{2.44}$$

$$\langle\overrightarrow{\mathbf{v}}_f\rangle\Big|_{in} = (u_{in}, 0, 0) \tag{2.45}$$

$$\langle\overrightarrow{\mathbf{v}}_f\rangle\Big|_{wall} = (0, 0, 0) \tag{2.46}$$

Chapter 3

Drying in a rotary drum dryer

3.1 Introduction

Drying mechanism refers to providing heat to a bed of particles by contacting with hot gas medium to reduce the water content. The latter is transferred as water vapor into the gas phase. During drying process, the particle temperature remains at saturated temperature of water which is at atmospheric pressure around $100°C$ so that adding heat leads to vaporize water content. The drying starts from surface of particles where the heat provided by gas phase is transferred by convection. After depletion of the water content on the surface, more heat is transferred inside particles via conduction to evaporate remaining water inside particles. This means there is a propagating plane from surface to the core of particles from dry to still wet area. Regarding the contact between solid-gas flow, the drying process is categorized to direct (conductive) and indirect (convective) technologies. The common drying media are air, superheated steam and flue gas. The comprehensive definition of drying is referred to [47]. The sources of heat could be provided by exhaust flue gas from hot furnace, engine or gas turbine; superheated steam from a steam or combined cycle plant; warm air from an air-cooled condenser in a steam or combined cycle plant; and steam from dedicated combustion of surplus biomass, or diverted product gas, char or bio-oil. [48]

Generally, there are three transport phenomena inside a dryer that happen simultaneously during drying as *i*) heat transfer between particle and gas; *ii*) particle transportation; and *iii*) water vapor transportation from particle to gas. The heat and mass transfer during transportation of particles inside dryer highly depend on the surface area and the contact time between particles and gas phase [47]. The basic idea for the treatment of particle-to-fluid heat transfer in porous media is to consider the situation for the individual particle. Appropriate quantities for the length scale and the velocity with a

geometrical function are sufficient to correlate the results of the single particle with the packed bed. These characteristic quantities are combined to the statistical parameter of the porous medium which is the void fraction with quantities that are accessible such as the particle size and mean fluid velocity. [49]

The particulate drying with superheated steam as an alternative to air has some advantages such as increased efficiency, improved safety due to the reduced risk for fires and explosions, no odorous or particulate emissions, a combination of drying with material sterilization and pasteurization, and faster drying rates [47, 50]. At larger scales in steam co-generation applications, the use of steam dryers may offer efficiency advantages. It makes recovery of low pressure steam or hot water for district heating possible. The exhaust gases are cleaned mostly with bag filters and cyclones, and the waste waters are treated with sand beds and their pH is adjusted prior to being led to the sewer. [51]

Recently, the use of steam drying techniques is increased so that it enables the integration of the dryer into existing energy sources where Fagernas et al. [48] has reviewed various types of dryers. The most common dryers are rotary dryers, fluidized bed dryers and conveying dryers. In fact, there is a lack of studies concerning vibrating grate dryers in which the main feature is transporting particles from the inlet to the outlet of the dryer via oscillatory motion of the grate. In band conveyor dryers, the particles are transported by blowing the drying medium through a thin static layer of material on a horizontally moving permeable band. In fluidized bed dryers, the gas is blown upward through a layer of particles such that all particles are suspended in the upward flowing gas [48]. This section states the biomass drying in a rotary dryer while the next section deals with a vibrating fluidized bed dryer specifically.

Generally, the rotary dryers are a kind of convective heat transfer devices which provide remarkable advantages such as good energy efficiency, better particle mixing and more effective drying. The operation of the rotary dryers is complicated due to the simultaneous heat and mass transfer between the solid and gas phases in addition to transport of particles through the dryer. The basic mechanism of drying consists of providing heat to the particles from the hot gas and evaporating water from particles into the gas phase. The water evaporation largely happens during the close contact between solid and gas phases that occurs in the fall stage and drying efficiency is closely related to the time of contact between two phases [52]. Each particle is heated up on its way from the inlet to the outlet of the dryer thereby the temperature varies along the length of the dryer but it is constant in width direction [53]. During drying process the particle temperature remains at saturated temperature of water so that at atmospheric pressure it is around $100°C$. Due to the gas-solid flow characteristics, the rotary dryers are suitable for dealing with homogeneous and heterogeneous materials as well as sticky ones.

Recently, rotary dryers have been employed to dry solid waste from processing of olives, woody biomass chips, carton packaging waste, alfalfa, as well as sewage sludge produced by wastewater treatment plants, which can be used as fertilizer [54].

The most important parameters that affect biomass drying are concluded in several works ([55], [56], [57]) as the initial gas temperature and solid moisture content. Besides, Johnson [58] has studied the importance of particle size distribution on the disintegration of wet distiller spent grain compacts during drying in superheated steam. The results show that a decrease in particle size of the compact results in a decrease in the expansion of the compact during the warm-up period of superheated steam drying. And Stroem [50] evaluates the drying behavior of Brewer's spent grain in a pilot-scale rotary superheated steam dryer. The evaluation is based on product moisture content, measurements of sticking and energy consumption. The results of an experimental design for three system parameters (steam temperature, steam velocity and feeding rate) are presented so that the critical parameters with the most significant effect on the moisture content are feed rate and inlet steam temperature. Also Castano [59] shows that the evaporation rate of the residual biomass inside a co-current rotary dryer depends on the gas temperature, gas flow speed, grain moisture content and grain size. It is stated that characteristics of particles and dimensions of dryers affect the drying time.

Therefore, in this chapter the mentioned DEM-CFD coupling model is applied to simulate a bed of wood particles moving in a rotary dryer to investigate the motion of particles on drying process. The aim is to investigate the influence of particle size distribution on drying parameters such as drying rate and time, particle bed mean temperature and moisture content. Also the motion of particles inside the drum is modeled whereby the particles move through the rotary cylinder via rolling and sliding on the wall and then fall at the bottom of the bed which leads to better contact with the gas phase and better heat transfer. The following assumptions are considered to simplify the complex drying process in the simulation of both rotary and vibrating grate dryers:

- Granular materials are isotropic with spherical shapes
- Heat-up is neglected since the initial particles temperature is $95°C$
- Shrinkage of solid material during drying is negligible
- Heat and mass transfer inside particles are in radial direction
- The dryer is perfectly insulated
- Superheated steam is used as gas medium
- Biomass beechwood is used as material

3.2 Validation of single particle drying

This section displays the validation of implied DEM-CFD coupling module with drying experiment of a single particle by Looi et al. [60]. The experimental device includes a drying chamber and a single particle located inside it. The inside diameter and the length of the drying chamber are approximately 25 and 100 mm, respectively. The apparatus is designed such that the rate of mass loss and the internal temperature of the particle could be continuously and simultaneously measured when drying is carried out in a pressurized superheated steam environment. The steam inlet is located at the lower end of the chamber and the steam exit at the top end. The particle is considered as a spherical wet coal of diameters $10, 12$ mm for cases **A** and **B** that the input variables are shown in Tab.3.1. The experiments are performed at the pressure of 2.4 bar, and the superheated steam temperature at $170°C$, as well as the steam velocity at 2.7 m/s.

TABLE 3.1: Input parameters of the experiments

Experiment by Looi [60]	A	B
Particle Diameter $d_p(mm)$	10	12
Gas Pressure $P(bar)$	2.4	2.4
Gas Temperature $T_g(°C)$	170	170
Gas Velocity $v_g(m/s)$	2.7	2.7
Initial moisture content $X_0(g\ water/g\ dry\ solid)$	1.60	1.60

Fig.7.2 shows prediction of particle core temperature done by DEM-CFD coupling module compared to the experiments. It could be seen that in case **A**, the temperature rises from saturation after 20 s while in case **B** it rises after 27 s which affirms smaller particle is dried faster as expected. Also it is noted that at the end of drying in both cases the particle temperature reaches the gas temperature ($170°C$) as anticipated. In total, the prediction of particle core temperature is in good agreement with the experiments.

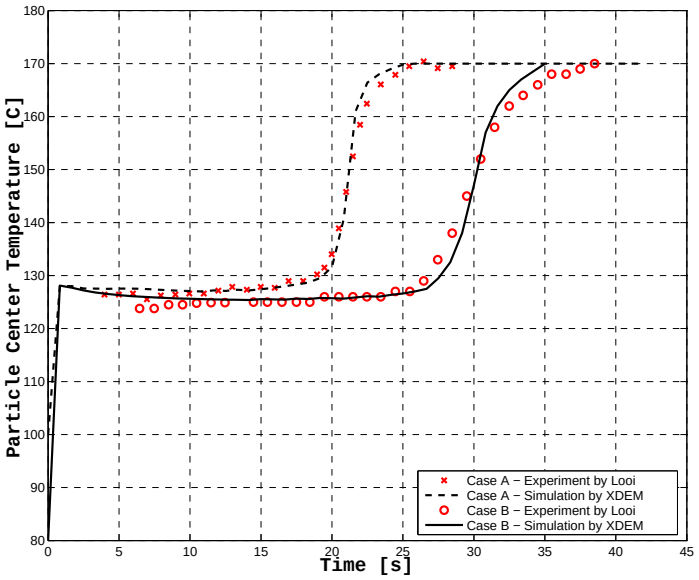

FIGURE 3.1: Particle size effect on drying of a coal particle— Case A: $d_p = 10mm$, $P = 2.4bar$, $T_a = 170°C$, $v_g = 2.7m/s$; Case B: $d_p = 12mm$, $P = 2.4bar$, $T_a = 170°C$, $v_g = 2.7m/s$

In addition, Fig.7.3 shows the drying rate behavior according to the moisture content for case **B** with experiment temperature $170°C$ and pressure 2.4 *bar* (tab.3.1). The AB part on the curve represents a warming-up period of the particle. The BC part is the constant-rate period where the particle temperature is constant during this period since heat transfer into the surface is constant and the heat is consumed just for water evaporation. While the surface temperature is constant, the free water during constant-rate period is evaporated. When the free water is finished, the temperature starts to rise. This point is shown as point C, where the constant-rate ends and the drying rate begins falling that is termed the critical-moisture content. The curved portion CD is termed the falling-rate period and is typified by a continuously changing rate throughout the remainder of the drying cycle [61]. It is also shown the prediction of moisture content of the particle compared to the experiment. As can be seen the initial moisture content (60 $db\%$) is vanished after drying completion.

Furthermore, the mentioned DEM-CFD approach is capable to model internal thermo-physical properties such as temperature and species inside the particle. The later is denoted as water content particularly in this chapter. The particle could be divided into arbitrary number of cells from the center to surface so that higher number of cells improves the accuracy of the results. Generally, the drying process occurs at a drying front determined from the surface to center of particle where it is considered a singular saturated condition on drying front. While the wet zone between the drying front and the particle center remains below the saturated temperature. And the temperature of dry

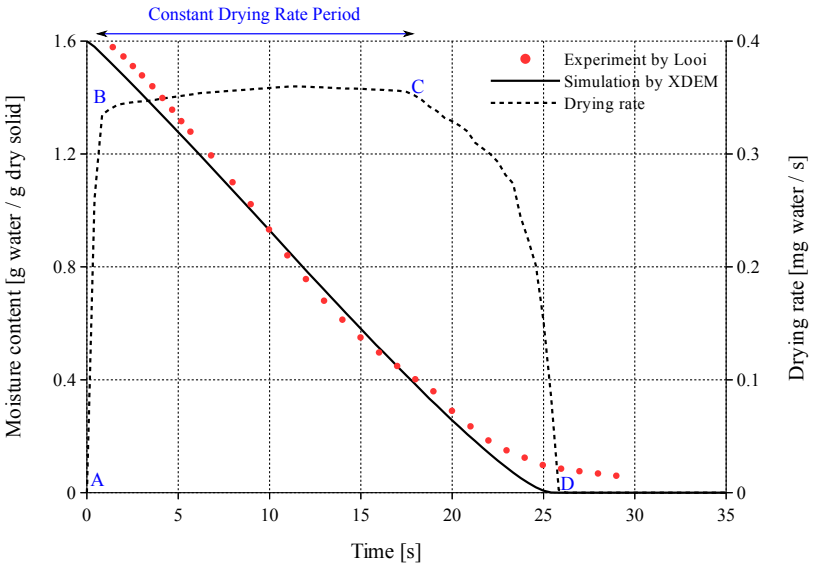

FIGURE 3.2: Drying rate and moisture content vs. time— case **B**: $d_p = 12mm$, $P = 2.4bar$, $T_a = 170°C$, $v_g = 2.7m/s$

zone which is between the drying front and the particle surface increases progressively until reaching the steam temperature. Fig.3.3 shows the temperature behavior inside the particle versus time and radius for case **B** (tab.3.1). As stated, the particle is initiated at $95°C$ and in the beginning of simulation the surface temperature reaches the saturation status ($100°C$). In this moment, the drying front is on the particle surface. After diminishing the moisture content on the surface, the temperature increases gradually and drying front moves towards the center. This is carried out by propagating heat from the surrounding steam into the particle. This procedure continues until the drying front reaches the center whereas all moisture content is evaporated. In this time, the drying process is finished and the particle temperature ascends towards the steam temperature. In addition, fig.3.4 illustrates the normalized moisture content inside the particle versus time and radius. It remarks the behavior of drying front starting from the surface to the core of particle based on water evaporation. Where in the beginning of simulation, the surface includes the water content so that with further heat transfer, the drying front moves from the surface to the core of particle with regards to water elimination.

Thus, the drying validation of a single particle ensures the proposed DEM-CFD coupling module as a reliable tool to simulate drying process in industrial applications such as rotary dryers which is investigated in this chapter and vibrating fluidized bed dryers discussed in next chapter.

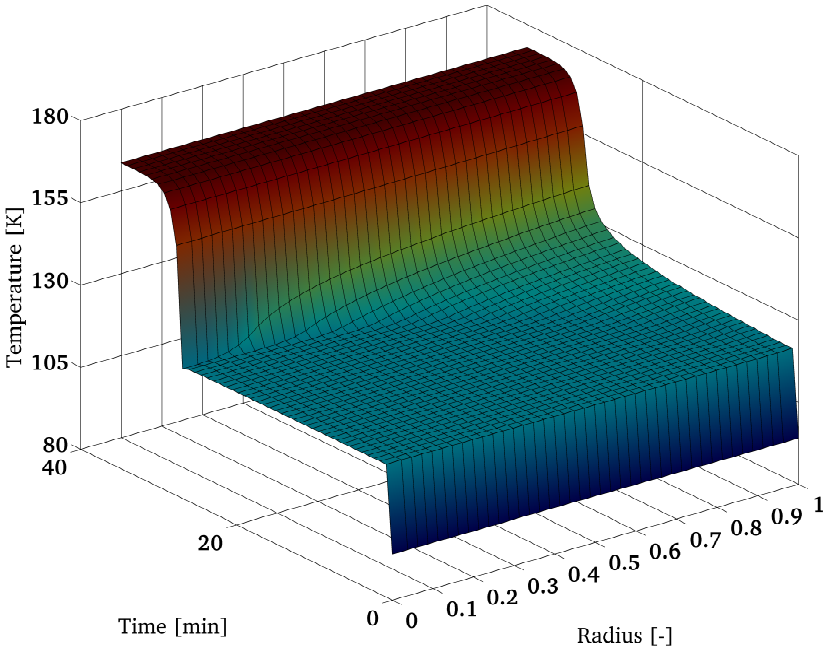

FIGURE 3.3: Temperature distribution inside particle vs. time and radius

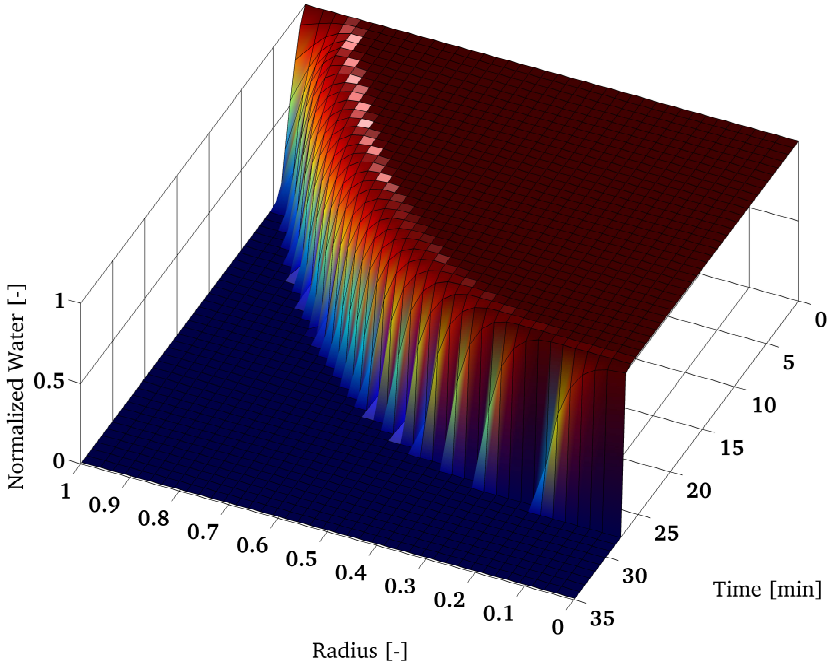

FIGURE 3.4: Normalized water content inside particle vs. time and radius

3.3 Case definition

The case study is a rotary cylinder with geometry as length of 200 mm and diameter of 40 mm so that the drum axis is horizontal and the particles are transported through the drum because of the flow drag and the cylinder rotational velocity as 5 $[2\pi/s]$. The gas phase medium is specified as hot air that is in direct contact with the particles. Three different sizes of particles are considered as diameter of 2 mm, half size 1 mm and fifth size 0.4 mm; so that the particle properties are shown in tab.3.2. In order to evaluate the effects of particle size distribution, three main cases (Case1-3 in tab.3.3) are defined so that the mass of the bed remains constant at 156.6 g. At the first case, all particles have the same diameter of 2 mm (Fig.3.5(b)). For the second and third cases, the procedure is keeping half the mass (78.3 g) with diameter of 2 mm, and the other half of mass with diameter of 1 mm and 0.4 mm (see Fig.3.5(c),3.5(d)), but the total mass of the bed remains constant. As can be seen in the tab.3.3 with decreasing the particle size, the number of particles and thus the surface area of the bed increases so that it influences the heat transfer between the solid and gas phases which is discussed later. The Fig.4.2 shows the drum case geometry including a packed bed of particles with different sizes as distributed randomly. As can be seen, the hot air enters the drum and encounters with particles while drum is rotating that helps to speed up drying and the cool air exits the drum after exchanging heat with particles.

TABLE 3.2: Input properties of solid and gas phases for drum simulation

Material Properties	*Value*
Softwood	
Density $\rho_p(kg/m^3)$	590
Porosity ε_p	0.64
Specific heat $c_p(kJ/kgK)$	1551
Conductivity $\lambda(W/mK)$	0.47
Permeability $K(-)$	0.02
Pore Diameter (m)	50×10^{-6}
Tortuosity $(-)$	1
Initial moisture content $X_0(g\ water/g\ dry\ solid)$	1.05
Initial temperature $T_0(°C)$	95
Superheated Steam Conditions	
Pressure $P(bar)$	1
Density $\rho_g(kg/m^3)$	0.59

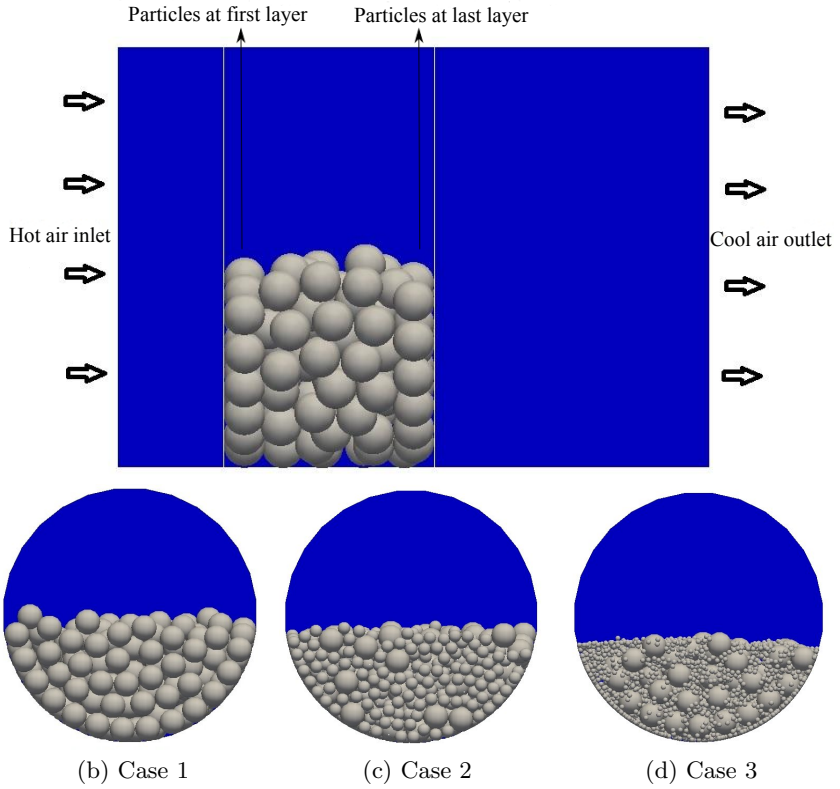

(b) Case 1 (c) Case 2 (d) Case 3

FIGURE 3.5: Schematic of the rotary dryer including different particle size distribution

TABLE 3.3: particle size distribution specified for different cases

Case	$d_p[mm]$	*Particles No.*	*Bed Mass*$[g]$	$SA[m^2]$	$SA_{total}[m^2]$	*SA change*
1	2	25	78.3	0.03416	0.06832	–
	2	25	78.3	0.03416		
2	2	25	78.3	0.03416	0.09699	+42 %
	1	200	78.3	0.06283		
3	2	25	78.3	0.03416	0.22540	+230 %
	0.4	3125	78.3	0.15708		
4	1	200	78.3	0.06283	0.21991	+222 %
	0.4	3125	78.3	0.15708		
5	1	200	78.3	0.06283	0.12566	+84 %
	1	200	78.3	0.06283		
6	0.4	3125	78.3	0.15708	0.31416	+360 %
	0.4	3125	78.3	0.15708		

3.4 Result and discussion

The most important parameters that influence the drying process in the rotary dryers are the gas temperature/velocity and the particle surface. In this section the effects of these parameters on the particle temperature and moisture content are assessed. Moreover, the effects of size distribution on the drying rate and the heat loss are discussed and finally the temperature distribution of particles in different instances during drying are visually exhibited.

3.4.1 Effect of surface area on drying rate

Fig.3.6 demonstrates drying rate behavior at the gas temperature of $350°C$, pressure of 1 bar and velocity of 1 m/s. During the drying process in the rotary dryers, there is no constant-rate period which means that drying happens only in the falling-rate period [57]. Due to the rotary motion of particles, the contact face of particles to the gas phase change suddenly and continuously which leads to chaotic drying of particles. Thus the constant-rate does not take place and only falling-rate occurs. This is shown in Fig.3.6 so that after reaching to the highest rate, instead of staying at constant rate similar to part AB for single particle (Fig.7.3), it falls down till finishing the moisture content. On the other hand, in addition to an increase in the gas flow rate which causes an increase in heat transfer rate between gas-particles and the drying rate augments [55], changing particle size distribution to raise surface area also boosts the drying rate. According to the Tab.3.3 which represents increasing surface area with regards to different combination of particle size distribution, it could be seen that higher surface area leads to grow the critical moisture content and reduce the drying time. In other words, comparing the Case 1 (the base case with homogeneous particle size of 2 mm) and the Case 6 (distribution of size 0.4 mm and 2 mm), with increasing the surface area to 360% (tab.3.3) the drying rate is enhanced from 0.00024 $[kg\ water/s]$ to 0.00052 $[kg\ water/s]$ so that the drying rate growth is considerably more than twice. From time point of view, at Case 1 all particles are dried completely after 2 s while at Case 6 the drying time is shortened to 0.6 s which displays effect of surface area increment to reduce residence time.

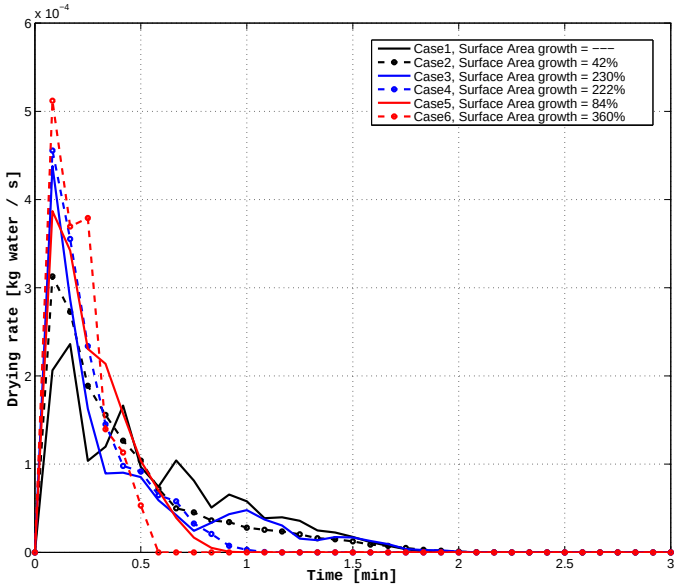

FIGURE 3.6: Drying rate for Case1-6 with different surface area growth vs. time, at gas $T = 350°C$; $P = 1\ bar$; $V = 1\ m/s$ and bed mass $= 78.3\ g$

3.4.2 Effect of surface area on heat loss

This section significantly depicts the influence of surface area growth on heat loss quantity. In Fig.3.7 three cases (Case 1-3) at the gas temperature of $350°C$, pressure of 1 *bar* and velocity of 1 m/s, are considered so that increasing surface area leads to rising the bed mean total energy earlier and faster drying. The lines show the cases with adiabatic wall and the dash-lines represent non-adiabatic wall with initial ambient temperature. As expected, all cases start from the same point and they finish at the same point when there is no heat exchange between particles and drum wall (adiabatic). In order to investigate the effect of surface area, the dash-lines represent the cases when the drum wall is non-adiabatic. That is, there exist conductive and radiative heat transfer between the particles and drum wall which leads to heat loss. The relation below comes from evaluation of Fig.3.7 that shows maximum energy value of Case 1-3.

blue-dashline (Case 3) > black-dashline (Case 2) > red-dashline (Case 1)

This means that with increasing surface area, the heat loss is reduced which makes the drying more efficient. The reason is increasing surface area improves the rate of convective heat transfer between solid-gas that leads to reduce the energy loss.

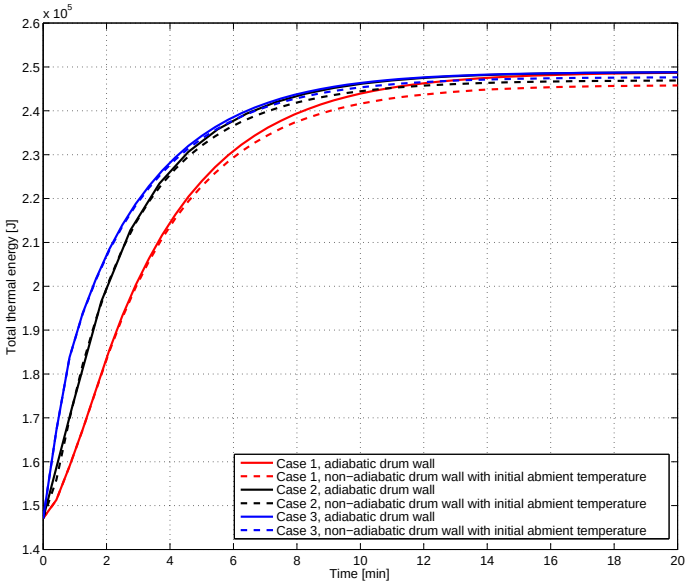

FIGURE 3.7: Total thermal energy for Case1-6 with different surface area growth vs. time, at gas $T = 350°C$; $P = 1\ bar$; $V = 1\ m/s$ and bed mass = 78.3 g

3.4.3 Inlet gas velocity

Fig.3.8(a) and 3.8(b) compare prediction of particle bed mean temperature and moisture content based on the different inlet gas velocity (1, 1.5, 2 m/s) for Case 1-2. As stated, higher inlet gas velocity leads to better heat transfer rate and enhanced drag force acting on the particles which causes more dispersed bed, leading to less drying time. This is expressed according to dominant convective heat transfer rather than conductive heat transfer inside particle which is not effected by gas flow rate. It could be seen from Fig.3.8(a) that the bed mean temperature starts at initial temperature of $95°C$ (heat-up is not considered) and finishes to the gas temperature ($350°C$) expectedly. Increasing inlet gas velocity leads to rise the bed mean temperature sooner and thus drying is faster. Similarly, the behavior of the bed moisture content is shown in Fig.3.8(b) which is started from initial value defined as 5 $db\%$ and total drying occurs when all water is evaporated and it reaches zero. Then the added heat is used to raise particle temperature until gas temperature. Obviously, with increasing gas velocity the bed moisture content drops sooner and consequently drying is quicker.

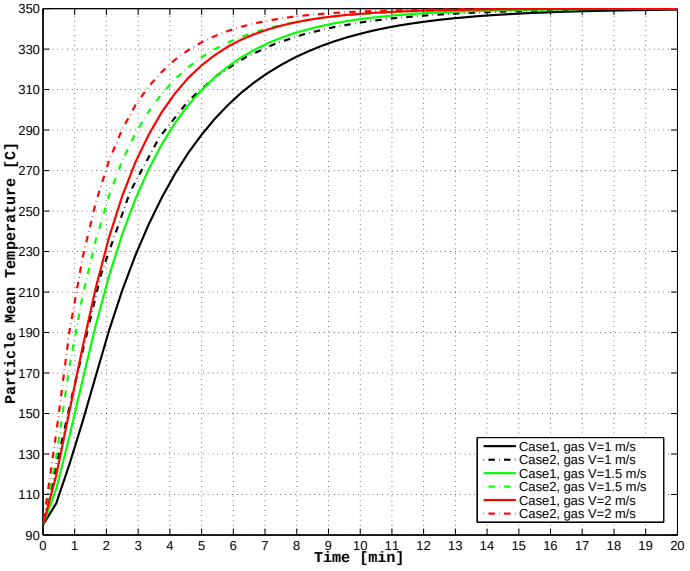

(a) Bed mean temperature with different inlet gas velocity for Case1-2 vs. time

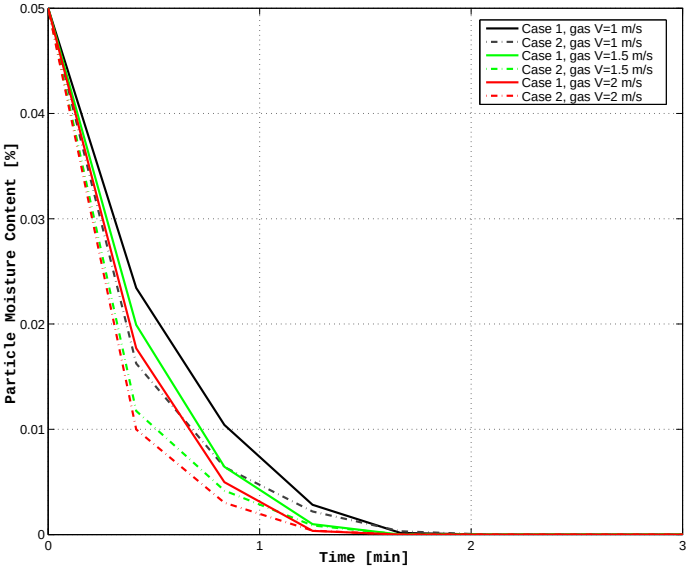

(b) Bed mean moisture content with different inlet gas velocity for Case1-2 vs. time

FIGURE 3.8: Effect of inlet gas velocity on (a) bed mean temperature (b); bed moisture content

3.4.4 Inlet gas temperature

The influence of gas temperature on the particle bed mean temperature and bed moisture content are shown in Fig.3.9(a) and 3.9(b) for Case 1-2. The strict and dash lines show different gas temperatures for Case 1 and 2, respectively. The dash lines show that at the same temperature with 42% higher contact surface area of Case 2 rather than Case

1, the drying is faster as discussed previously. In addition, with increasing inlet gas temperature (210, 280 and 350°C), it could be seen that the particle mean temperature rises earlier and moisture content of the bed evaporates sooner. This means that higher gas temperature increases the conductive heat transfer and consequently leads to faster drying.

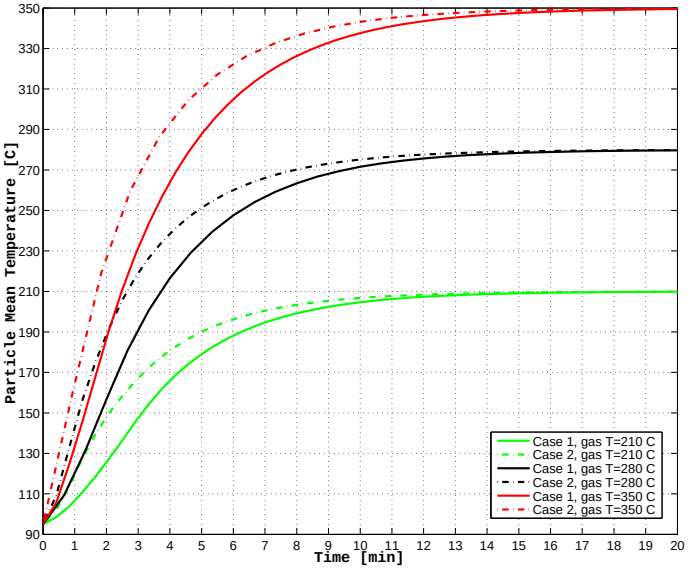

(a) Bed mean temperature with different inlet gas temperature for Case1-2 vs. time

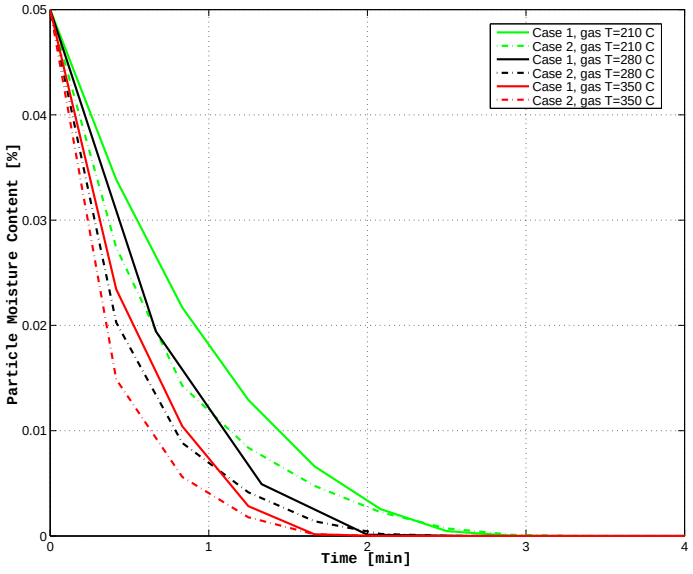

(b) Bed mean moisture content with different inlet gas temperature for Case1-2 vs. time

FIGURE 3.9: Effect of inlet gas temperature on (a) bed mean temperature (b); bed moisture content

3.4.5 Temperature distribution of particles

The temperature distribution of particles is visually presented in fig.3.10-3.11 at four different instances $(10, 60, 150, 240s)$ in order to investigate the influence of particle size distribution. After $10s$, the particles in Case 1 are homogeneously close to saturation temperature (below $100°C$) but drying is not started yet. In Case 2 the small particles at first layer (which are close to the gas inlet) start to dry, while the particles through the bed reach the saturation temperature subsequently. In Case 3 the smallest particles at the first layer are dried while rear ones start to dry. By injecting hot gas continuously, at $60s$ the surface temperature of particles in Case 1 passed the saturation temperature which shows the surface is dried and the drying front is traversed from the surface towards the particle core. While in Case 2 the surface temperature of smaller particles are higher than big ones owing to the lower surface area. And that is why in Case 3, the surface temperature of smallest particles at first layer are quite near gas temperature. As a result, with passing the time to $150s$ and $240s$ according to the fig.3.11 (left and right), the comparison of surface temperature of particles shows that smaller particles dry faster due to the faster heat transfer from the surface to the core of particles.

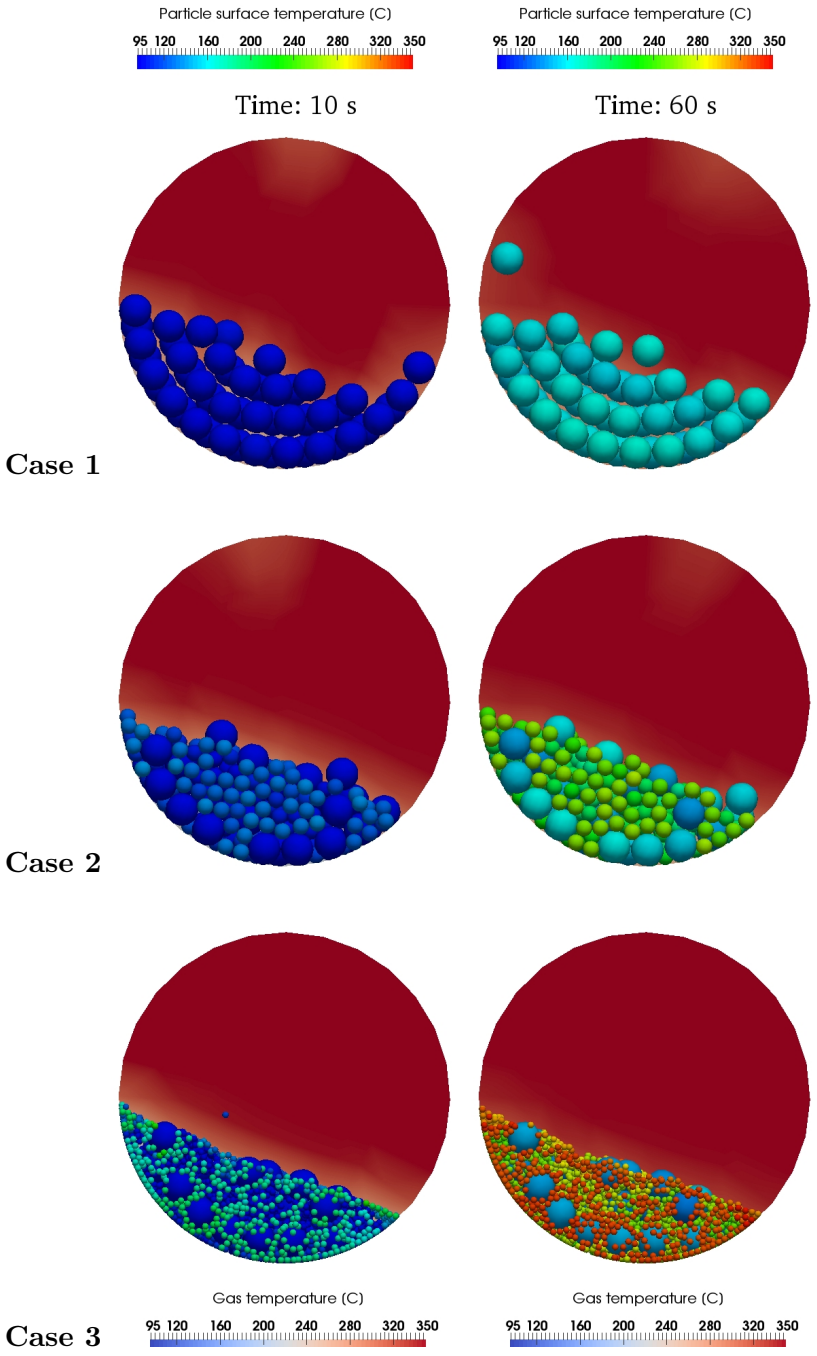

FIGURE 3.10: Temperature distribution of particles for Case1-3, left: at 10s, right: at 60s

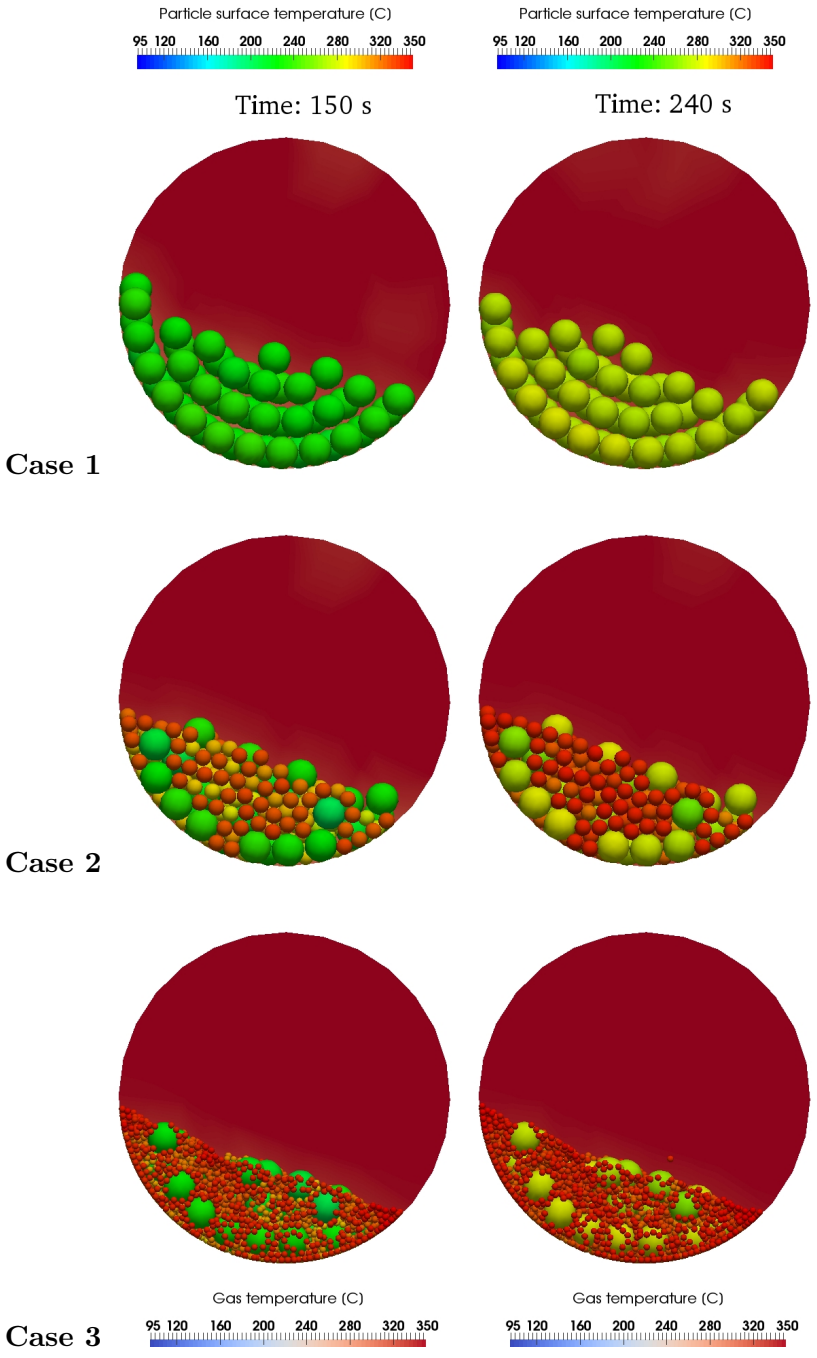

FIGURE 3.11: Temperature distribution of particles for Case1-3, left: at 150s, right: at 240s

3.5 Conclusion

In this chapter, the drying process of wet spherical wood particles in a rotary drum is investigated. Dynamics motion of particles is considered with employing the implied DEM-CFD module. A comparison of temperature and moisture content between experiment and simulation for a single particle show a good agreement. The case study is a drum rotating with a constant angular velocity involving moist particles as a packed bed at the beginning of process. The focus was verifying the effect of particle size distribution on drying rate and heat loss. In case of drying rate, there is no constant-rate period and it takes place in falling-rate period only. It is shown that smaller particles have higher critical drying rate and higher heat loss to the wall. This is due to lower conduction and radiation heat transfer between particles and wall. That is, with decreasing the particle size with constant mass of the bed, the surface area is increased. This leads to higher convective heat transfer rate and faster drying. Moreover, the bed mean temperature and water content graphs demonstrate that with increasing gas inlet temperature and velocity, the drying time is lower. Finally, the temperature distribution of particles are shown visually at four different instances during drying which represent the smaller particles dry faster. The reason is mentioned that heat transfer inside the small sizes of particles is faster.

Chapter 4

Drying in a vibrating grate dryer

4.1 Introduction

The vibrating grate dryers are a combination of conveying and fluidized bed dryers. That is, the transportation of particles from inlet to outlet is added to fluidization with gas phase. This enables the vibrating grate dryers as efficient and powerful drying facilities in industrial applications. Also the entrainment phenomenon could happen when the grate motion and the gas flow rate are relatively high. In a typical vibrating dryer, the particles are transferred to the dryer where the bottom grate has an oscillatory motion in both vertical and horizontal directions. Simultaneously, the particles face the drying medium which leads to fluidize and move the particles forward until exiting from the system. Whereby, the particles and gas phase mix properly leading to better heat transfer and consequently better drying.

In general, the vibrating fluidized bed dryers are used for drying cohesive, sticky, and agglomerated materials that cannot be well fluidized; for wet particles, or a very thin bed layer. The flow of particles could be considered as plug-flow which means the vibration intensity in addition to the gas flow are significant factors that affect the drying rate, particle mean residence time and particle dispersion [62]. The vibrating fluidized bed of solid particles is a modification of the conventional bubbling fluidized bed dryers where vibration energy is used to transfer the bed of particles from packed to fluidized state. Application of vibrating fluidized bed dryers in several unit operations (drying, granulation, coating, etc.) in chemical, food, pharmaceutical, and other industries is increasing due to the following advantages compared to a conventional fluidized bed dryer which can significantly reduce the energy consumption and drying time. [63]

- Controllable residence time and mixing intensity via amplitude/frequency of vibration
- Better heat and mass transfer due to well mixing of solid-gas phase
- Higher efficiency for drying of sticky and pasty materials

In another words, the wet solid particles enter the dryer by a screw feeder and are fluidized smoothly via the grate vibration combined with superheated steam flow leading to an effective mixing of the particles and gas flow. Because of mechanical vibration in both vertical and horizontal directions as well as the flow drag force, the solid particles move forward along the dryer and a partially dry product exits at the end so that the temperature of the solids progressively increases from inlet to outlet of the dryer. In this chapter, the following assumptions are performed to simplify the complex processes in the vibrating dryer.

- Solid fuel is considered as isotropic with spherical shapes
- Heat-up process is neglected
- Shrinkage of solid material during drying is negligible
- Heat and mass transfer inside particles are in radial direction
- The dryer is perfectly insulated
- Superheated steam is used as gas medium
- Biomass beechwood is used as material

In the previous chapter, drying of wood particles in a rotary dryer is investigated with emphasis on the bed surface area effects through different particle size distribution. As a complementary work, the same approach is used to analyze drying of biomass particles on a vibrating grate in this section. Also the motion of particles inside the vibrating grate dryer is modeled in which the particles move forward inside the dryer by oscillatory motion of vibrating grate plate as well as drag force by gas medium. The aim is investigating the effect of following operational conditions on the temperature and moisture content of particles, drying rate and residence time.

- Gas temperature
- Gas velocity

- Initial dryer temperature
- Initial moisture content of the particles
- Vibration intensity
- Particle size distribution

4.2 Experiment

In the previous chapter, drying of a single particle is verified with the experiments done by Looi et al. [60]. While in this chapter, drying of a moving bed of particles on a vibrating fluidized bed is validated with experiment carried out in Soil-Concept company located in Diekirch, Luxembourg. In the experiment procedure, firstly some samples from stored biomass beechwood are chosen and their volume and bulk mass are measured. Three different experiments are done and the results are presented graphically in fig.4.1. Then the samples are separately held in an oven (at Soil-Concept) for a while to dry slowly and the volume and bulk mass are measured again. This procedure is continued until evaporating the whole water and the remaining bulk mass is specified as the final mass. With regards to Eq.4.1 the initial moisture content is calculated according to the measured initial and final bulk mass.

$$MC_{wb} = \frac{W_i - W_f}{W_i} \times 100 \tag{4.1}$$

Where MC_{wb}, W_i and W_f are wet-basis moisture content, initial and final sample weight. To estimate the initial and final moisture content, this procedure is repeated for each drying experiment test both at the beginning and at the end. The goal is using an initial moisture content for the simulation and reaching the final moisture content according to the residence time recorded in experiment. Tab.4.1 illustrates three different experiments with the initial and final moisture content so that the mean value is considered for the simulation. That is, the initial moisture content of 51.5 $wb\%$ and the initial density of 250.6 kg/m^3 are used to validate the simulation case with the aim of reaching the final moisture content of 9.2 $wb\%$.

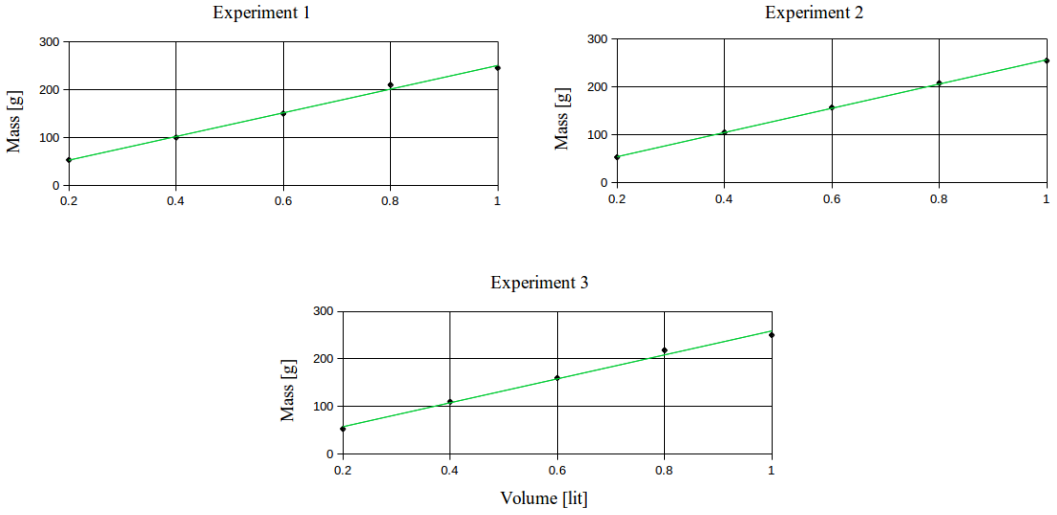

FIGURE 4.1: Three different experiments to estimate the density of wet beechwood material

TABLE 4.1: Experiment properties

Exp.	***before drying***				***after drying***		
	$W_i[g]$	$W_f[g]$	$MC_i[wb\%]$	$\rho\ [kg/m^3]$	$W_i[g]$	$W_f[g]$	$MC_f[wb\%]$
1	245.5	119.8	51.2	247.5	345.8	313.3	9.4
2	254.8	118.9	53.3	253.3	334.9	300.4	10.3
3	251.1	125.8	49.9	251.1	349.5	321.5	8.0
mean	254.4	121.5	51.5	250.6	343.4	311.7	9.2

After estimating the initial moisture content and the initial density of the particles, and according to the beechwood material properties (tab.4.2) and input parameters (tab.4.3), the experiment in the dryer is carried out in order to validate the simulation result. Fig.4.2 shows the industrial scale vibrating grate dryer including the solid-gas inlets and outlets where the system is properly isolated. In addition, fig.4.3 illustrates the vibrating grate plate inside the dryer where the particles fall down on it. To heat up the system before drying, the steam is injected into the dryer until the gas temperature inside the dryer exceeds 100 $°C$. Then the biomass feeding starts using a screw feeder which transports the biomass into the dryer with the rate of 100 t/h for 5 s. The feedstock is forest residues and the measured size distribution of particles is shown in Fig.4.4. The exhaust gases are cleaned by bag filters and cyclone.

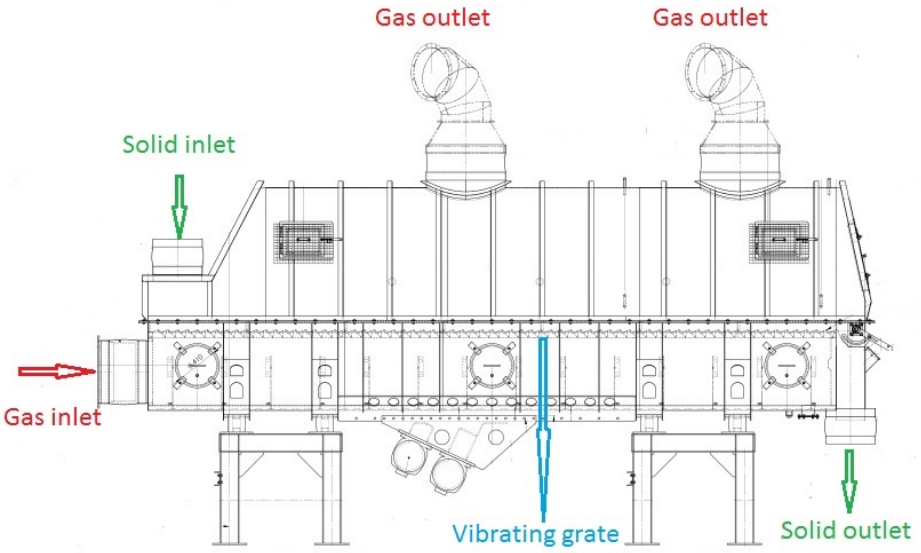

FIGURE 4.2: Schematic vibrating grate dryer

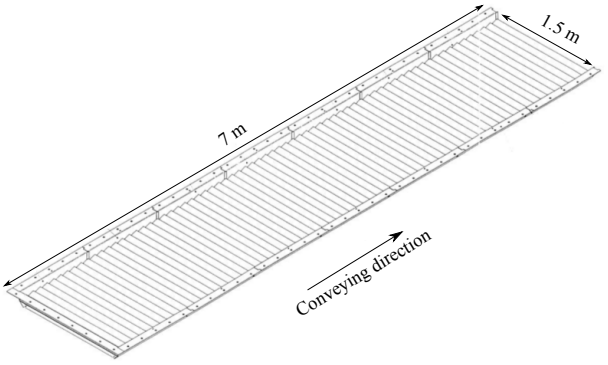

FIGURE 4.3: Vibrating grate plate

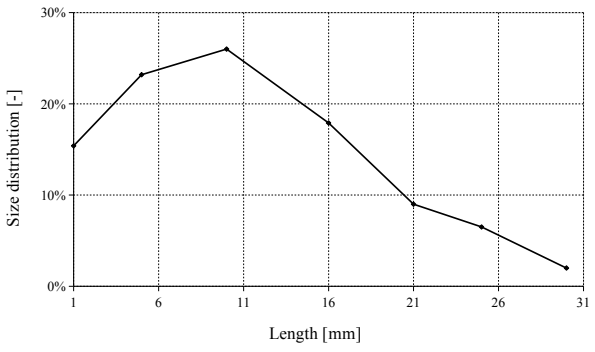

FIGURE 4.4: Measured size distribution of beechwood particles

TABLE 4.2: Beechwood material properties used for simulation

Density $\rho_p(kg/m^3)$	250.6
Porosity ε_p	0.52
Specific heat $c_p(kJ/kgK)$	1.551
Conductivity $\lambda(W/mK)$	0.47
Permeability $K(-)$	0.02
Pore Diameter (m)	50×10^{-6}
Tortuosity $(-)$	1
Initial moisture content $(wb\%)$	51.5
Initial temperature $T_0(°C)$	95
Particles No. (app)	16000

TABLE 4.3: Input parameters of the vibrating grate experiment used for simulation

Experiment	**Case 0**
particle size distribution	Fig.4.4
steam pressure $P(bar)$	1
steam temperature $T_g(°C)$	210
steam velocity $v_g(m/s)$	1.6
steam density $\rho_g(kg/m^3)$	0.59
initial dryer temperature $T_g(°C)$	100
grate frequency $Fr(Hz)$	11
grate amplitude $A_x - A_z(mm)$	6-3

4.3 Case definition

Dryer geometry in *length*, *width* and *height* directions are 7, 1.5 and 2.2 m, respectively. While the case study used for the simulations has the same geometry as the experimental facility except *width* direction. This is to reduce the running time of the simulation, since the temperature gradient is constant in *width* direction, thereby one slice of the dryer (as 0.1 m) is performed in this side. However, two periodic boundary walls are considered to predict the motion of particles properly. The particles are transported through the horizontal axis due to the vibrating motion of the grate and the gas flow drag force. The gas phase medium is the superheated steam which is in direct contact with the particles. The superheated steam enters to the dryer and encounters the wet particles. And after heat exchange with particles, the cooled air exits the dryer through two upper outlets. The simulation domain with boundary specifications is illustrated in Fig.4.5. To evaluate the effect of particle size distribution in accordance with the experimental test; and to track each particle size for investigating the density and moisture content variation accordingly, five different sizes are considered for simulations shown in Fig.4.6. This is according to the measured experimental size distribution in Fig.4.4.

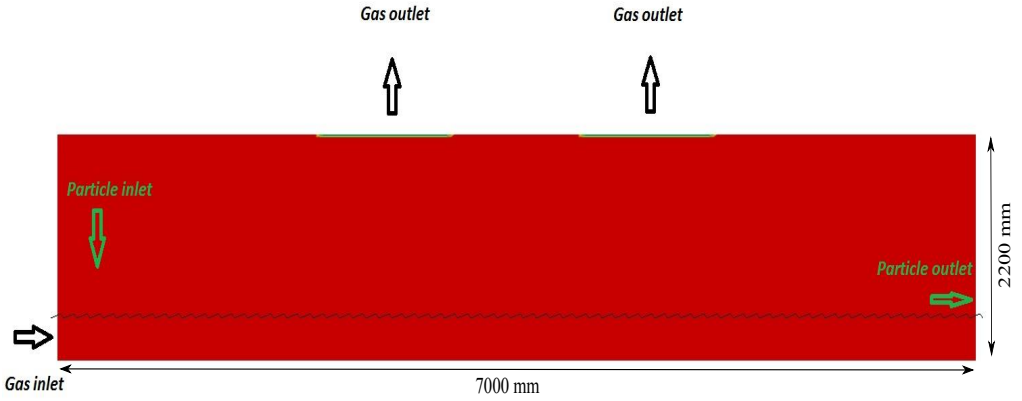

FIGURE 4.5: The simulation domain of vibrating grate dryer

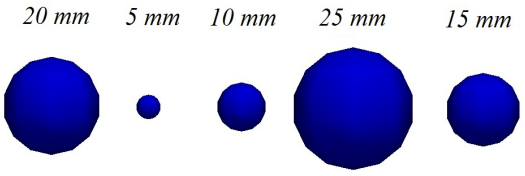

FIGURE 4.6: Size distribution of beechwood particles used for simulation

4.4 Validation

Fig.4.7 is showing the mean moisture content between simulation and experiment for *Case 0* (defined in tab.4.4 according to experiment). With comparing the final moisture content value in the simulation and experiment as 10.5 $wb\%$ and 9.2 $wb\%$, the difference is 1.3 $wb\%$. This small error shows good agreement between experimental and numerical predictions that demonstrates the mentioned procedure and setup are succeeded. Thus, it could be considered for more investigation of biomass drying on the vibrating grate dryer with the implied DEM-CFD coupling approach. It is also shown the drying rate trend in fig.4.7 where part AB denotes the warming-up period of the solids. Point B is the maximum rate and part BC is the falling-rate period meaning there is no constant-rate term. This states that drying in the vibrating grate occurs only in falling-rate period which is similar to drying behavior in the rotary drum.

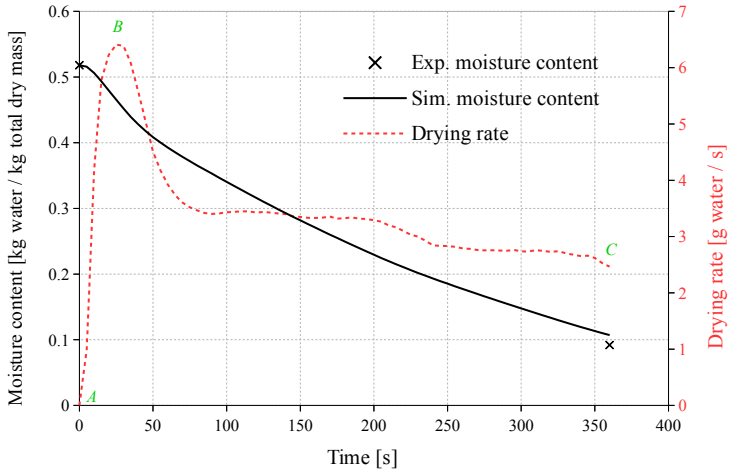

FIGURE 4.7: Validation of moisture content with experiment vs. drying rate

In addition, fig.4.8 shows the effect of particle size distribution on the mean temperature for *Case 0* (tab.4.4) with regards to the total residence time as 360 s. The initial temperature of all particles is 95 $°C$ and after reaching 100 $°C$, the water content starts to evaporate. Then the particle temperature rises with more provided heat. It is clear that drying time for various sizes is different as anticipated. For the smallest particle size ($5mm$), the fastest drying time occurs which is around 30 s. With increasing the size, the drying time increases accordingly so that for the largest particle size ($25mm$), the drying finishes at the end of simulation ($330s$). This means for the largest particle size, the drying process occurs through the whole length of the vibrating dryer so that the drying time is close to the total residence time. Thus, smaller particles have lower drying time due to faster heat transfer from the surface to center of particle.

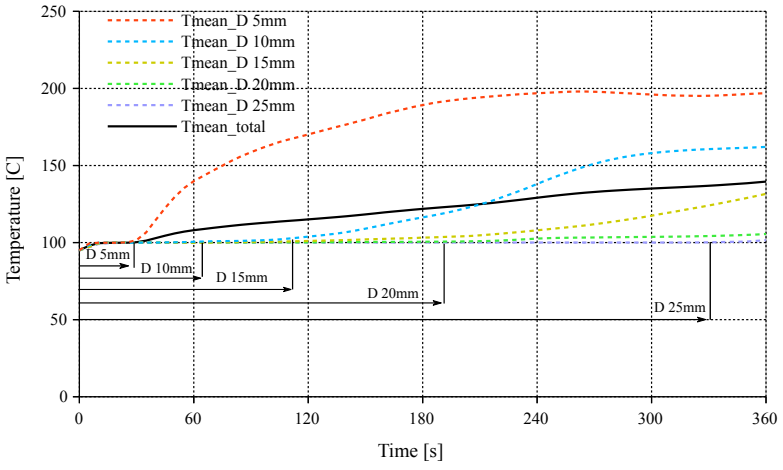

FIGURE 4.8: Particle mean temperature of various sizes $d_p = 5,\ 10,\ 15,\ 20,\ 25\ mm$ for the validation case

4.5 Result and discussion

In this section, drying of beechwood materials in the vibrating grate dryer is studied numerically based on the described DEM-CFD coupling approach. The predictions are for the effective parameters shown in Tab.4.4 as red values that will be discussed in details. Thereby, the effect of inlet gas temperature and velocity, initial temperature of dryer, initial moisture content of biomass and oscillatory motion of the grate on the particle temperature and moisture content as well as residence time and drying time are assessed. At the end, the temperature distribution of particles in various instances during drying are visually shown to investigate the effect of particle size distribution on drying.

TABLE 4.4: Case studies

Case No.	*gas* T_g $[°C]$	*gas* V_g $[m/s]$	*dryer* T_i $[°C]$	*MC* $[wb\%]$	*grate Fr* $[Hz]$	*grate* A_x $[mm]$	*grate* A_z $[mm]$
0 (base case)	210	1.6	100	51.8	11	6	3
1	200	1.6	100	51.8	11	6	3
2	220	1.6	100	51.8	11	6	3
3	230	1.6	100	51.8	11	6	3
4	210	1.45	100	51.8	11	6	3
5	210	1.72	100	51.8	11	6	3
6	210	1.85	100	51.8	11	6	3
7	210	1.6	110	51.8	11	6	3
8	210	1.6	120	51.8	11	6	3
9	210	1.6	130	51.8	11	6	3
10	210	1.6	100	56	11	6	3
11	210	1.6	100	60	11	6	3
12	210	1.6	100	51.8	10	6	3
13	210	1.6	100	51.8	12	6	3
14	210	1.6	100	51.8	13	6	3

4.5.1 Gas temperature

Fig.4.9 illustrates the mean temperature of all particles with various sizes for different inlet gas temperature. The base initial gas temperature according to the experiment is $T_i = 210\ °C$ and it is considered a lower value as $200\ °C$ and two higher values as $220,\ 230\ °C$ for other simulations. By the fact that the total drying time is similar but the

total mean temperature of the particles increases with increasing the gas temperature. This is because of higher energy of the gas flow given to the particles after finishing the drying process. Therefore, it can be observed that for the purpose of drying in this setup, there is no need to raise the gas temperature leading to optimize the energy consumption and make the system efficient.

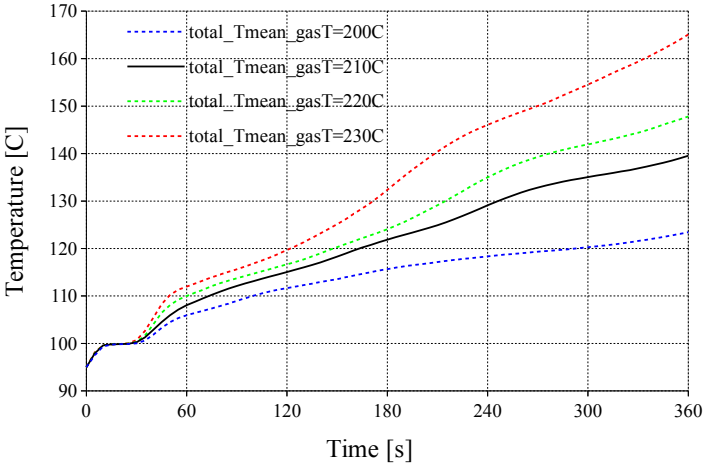

FIGURE 4.9: Total mean temperature of the bed in different gas flow temperature

4.5.2 Gas velocity

Here, the effect of gas flow rate on drying process is investigated. Fig.4.10(a) shows the drying rate behavior according to the different gas flow rate. It is obvious that with increasing the gas velocity, the critical drying rate is higher which leads to faster drying. The reason is that higher gas flow rates provide more total energy leading to faster heat transfer. As a result, it is also shown in fig.4.10(b) that increasing the gas flow rate reduces the mean moisture content of the bed during drying. Therefore, to decrease the final moisture content of particles, a feasible solution is increasing the gas flow rate.

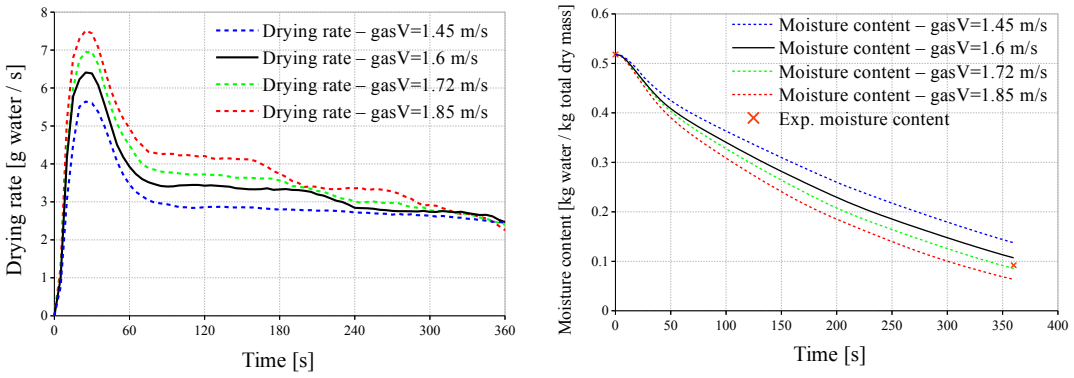

(a) (b)

FIGURE 4.10: Effect of gas flow velocity on (a) total drying rate of the bed; (b) total moisture content of the bed

4.5.3 Dryer temperature

Fig.4.11 illustrates the effect of initial gas temperature inside the dryer on total drying rate. The base temperature according to experiment is 100 $°C$ and it is considered $110, 120, 130$ $°C$ for three different simulations. With comparing the results, it is obvious that with increasing the initial gas temperature inside the dryer, the drying rate increases and consequently drying time is smaller. This could be explained as higher temperature of the dryer at initial point has more energy and this evaporates faster the water content of the fed particles.

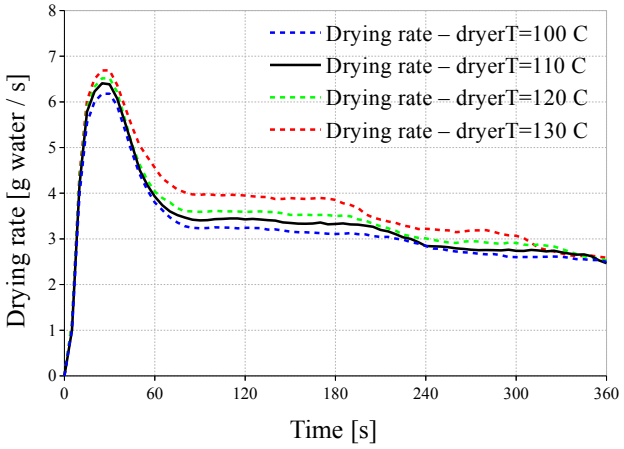

FIGURE 4.11: Total drying rate of the Case 0 for different initial dryer temperatures

4.5.4 Moisture content

According to the experiment, the base moisture content value of the solid biomass is 51.5 $wb\%$. Here, two higher values of 56 $wb\%$ and 60 $wb\%$ are considered in order to investigate the effect of moisture content on drying and residence time. Fig.4.12(a) shows the mean temperature of three particle sizes as $d_p = 5,\ 10,\ 15\ mm$ with regards to three defined moisture contents. For each particle size, the comparison of different moisture contents shows the bed mean temperature rises at the same time for three cases, while the particles with higher moisture contents have longer residence time. This is due to the fact that the particles with higher moisture content have higher weight which leads to move in the system relatively slower. That is, the residence time to dry the particles with higher initial moisture content is longer. Also the terminal temperature of the particles at the outlet of apparatus is lower. This outcome is also shown in fig.4.12(b) for the total mean temperature of the bed including all sizes with different initial moisture contents $MC = 51.5,\ 56,\ 60\ wb\%$.

4.5.5 Grate motion

The effect of particle size distribution on drying and residence time based on the grate motion is investigated here. That is, for various grate frequencies, the residence time for each particle size is compared and the relation between drying time and residence time is assessed. Fig.4.13 shows the influence of grate intensity on residence and drying time for particles with $d_p = 5, 10, 15, 20, 25\ mm$ as well as average of all particles. In case of the smallest particles (5 mm) in fig.4.13(a) it is clear that the drying time for all intensities is similar while the final temperature is different. That is, higher intensity results in accelerating the particles motion so that the residence time decreases and consequently the final particles temperature is reduced. This trend is also the same for larger particles except 25 mm. That means at higher intensities for particles with $d_p = 10, 15, 20\ mm$; the residence time is decreased while drying takes place properly. This leads to less energy consumption. But according to fig.4.13(e) the particles with size of 25 mm need more residence time to dry properly due to bigger size and contact surface area. This means to dry properly the particle size $25mm$, the higher intensities as $Fr = 12,\ 13\ Hz$ are not suitable.

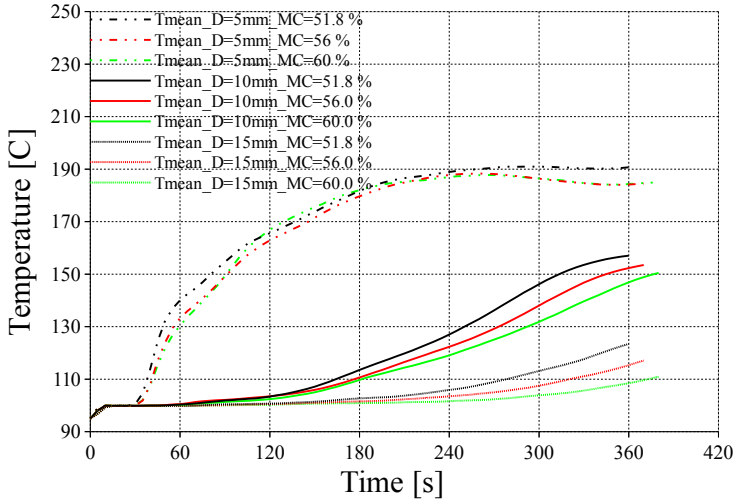

(a) $d_p = 5, 10, 15\ mm$

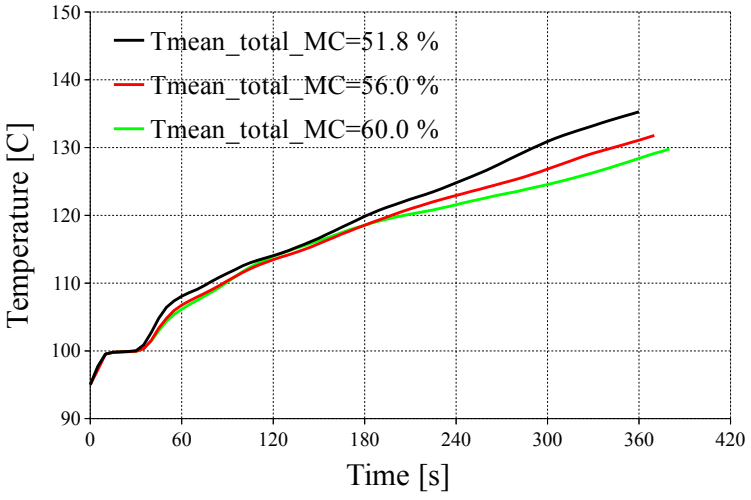

(b) *total*

FIGURE 4.12: Particle mean temperature for different initial moisture contents = 51.8, 56, 60 $wb\%$

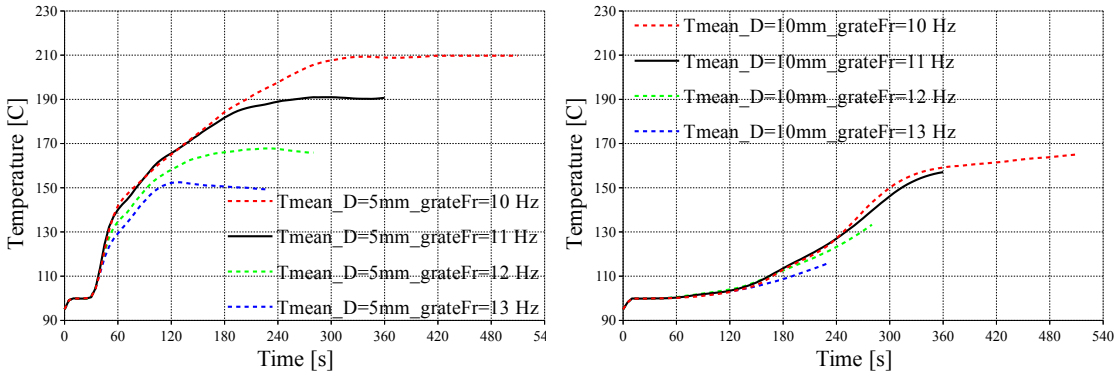

(a) 5mm

(b) 10mm

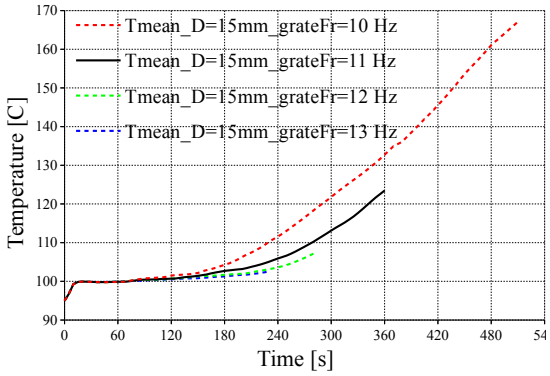

(c) 15mm

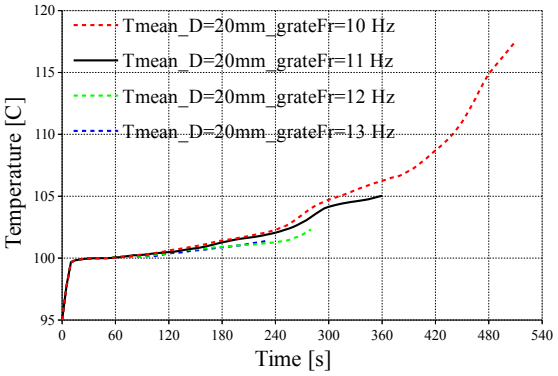

(d) 20mm

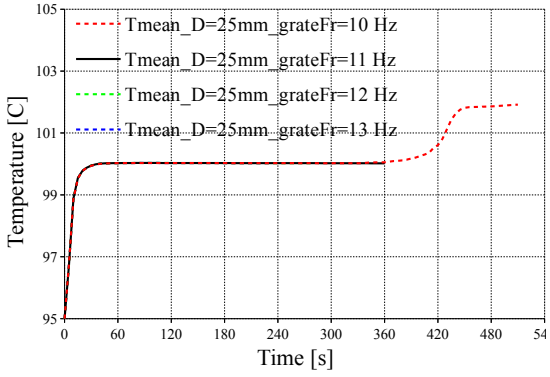

(e) 25mm

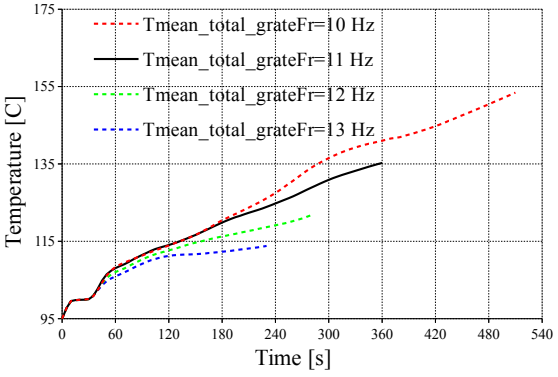

(f) *total*

FIGURE 4.13: Particle mean temperature based on grate intensity for various particle sizes

4.5.6 Instantaneous particle temperature

To evaluate the effect of particle size on drying, the particle temperature distribution at five instances $5, 30, 120, 240, 360$ s is visually shown in fig.4.14-4.15. This is for *Case 0* (based on the experiment) with the expressed setup in tab.4.4 and the residence time as $360s$. The focus of fig.4.14 is forward motion of the bed on the vibrating grate as well as temperature distribution of the gas phase. While fig.4.15 illustrates the particles in zoomed view to assess how the temperature of particles change during drying at different instances.

By the fact that the solid feeding time is $5s$, fig.4.14(a) and fig.4.15(a) show the particles falling down onto the grate after $5s$. Initial gas temperature inside the dryer is 100 $°C$ and with feeding the particles, inlet gas with temperature 210 $°C$ is injected. As shown in fig.4.2 and fig.4.5 the gas inlet is on the left side under the vibrating grate. With encountering the hot gas (210 $°C$) with fed particles (with 95 $°C$), the bed temperature starts to increase. Since the particles at the bottom of the bed are in direct contact with the hot gas, their temperature is rising faster than the particles through the bed. That is, the particles newly fed at the top of the bed have the initial temperature of 95 $°C$, while temperature of the base particles reach the saturation temperature around 100 $°C$. The temperature distribution of particles can be seen as color bar above the bed.

After $30s$ shown in fig.4.14(b) and fig.4.15(b), the bed height is changed to uniform configuration and the smallest particles move up further due to lower weight. In this moment, the surface temperature of particles reach the saturation while the smallest particles specially before $1m$ in the system are dried with higher temperature than saturation (according to the color bar above). This is due to facing gas of higher energy close to the gas inlet.

Fig.4.14(c) and fig.4.15(c) show the system at $120s$. In this moment, some particles left the dryer at saturation status. This is in accordance with the scope of the experiment as reaching the total moisture under 10 $\%wb$. While at the middle of the vibrating dryer between $3 - 4m$, the small particles are dried and their temperature passed the saturation status reaching the gas temperature. And the large particles are mostly dried based on the temperature higher than 100 $°C$.

Most of the particles after $240s$ left the domain which is shown in fig.4.14(d) and fig.4.15(d). While the particles inside the system still receive more energy and their temperature rises. This procedure continues until the particle temperature reaches the gas temperature (210 $°C$). It is clear that only small particles could achieve the gas temperature. This is due to the smaller size that leads to transfer the energy from hot

gas to the particles center faster. While the large particles at the end of dryer are dried but their temperature is still beneath gas temperature.

At the end of the simulation and residence time ($360s$) as shown in fig.4.14(e) and fig.4.15(e), all particles are out of the dryer domain. And the gas temperature is uniformly 210 $°C$ since there is no more solid element for heat transfer. With looking at the exterior bed closely in fig.4.15(e), it is obvious that the upper part has a temperature close to the gas phase 210 $°C$ while the bottom part has the saturation status temperature (100 $°C$). This is explained as the particles at the top had more residence time and consequently their temperature could exceed the saturation. While the particles within the bed have lower temperature due to less residence time so that the underneath particles are in saturation status.

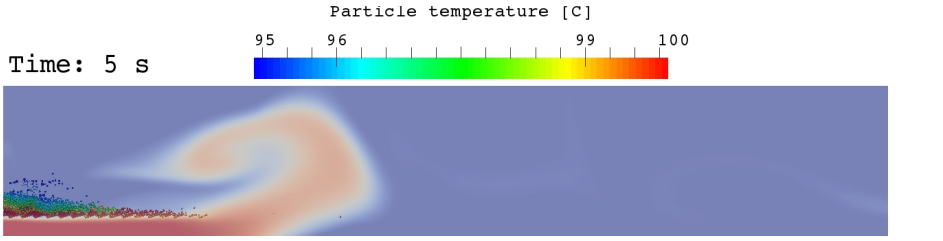

(a)

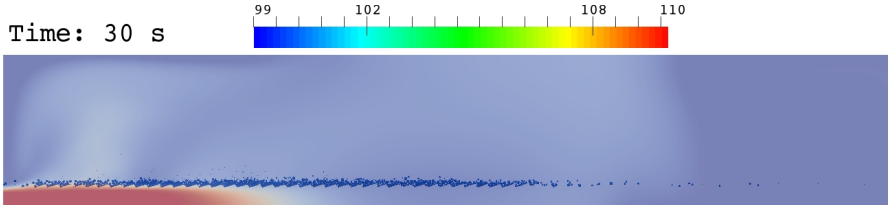

(b)

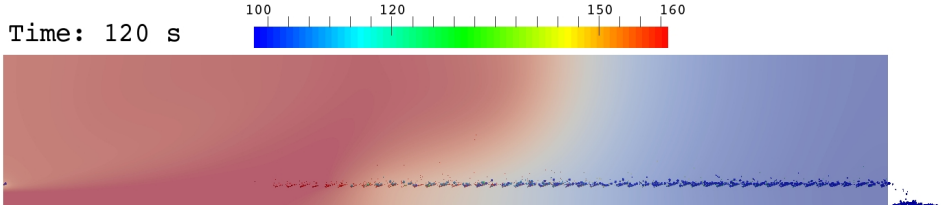

(c)

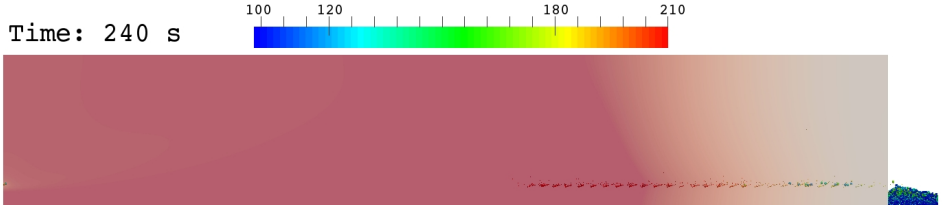

(d)

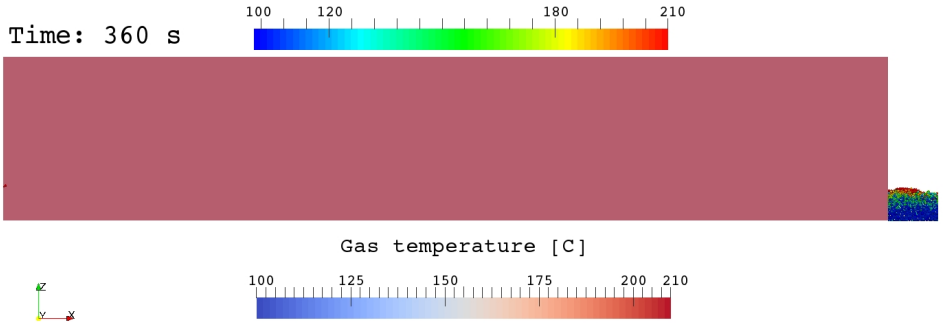

(e)

FIGURE 4.14: Temperature distribution of the gas and particles at different instances

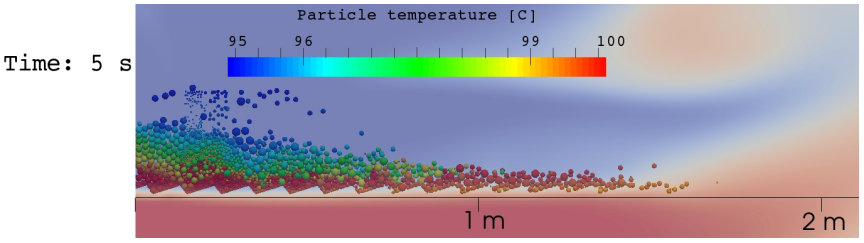

(a)

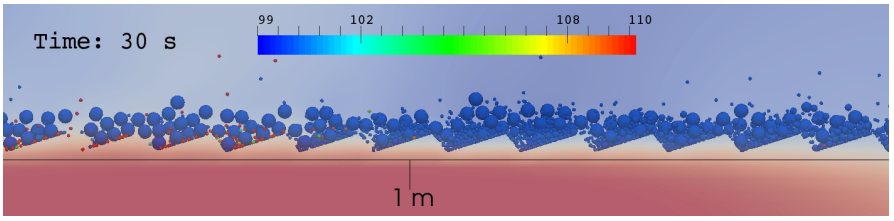

(b)

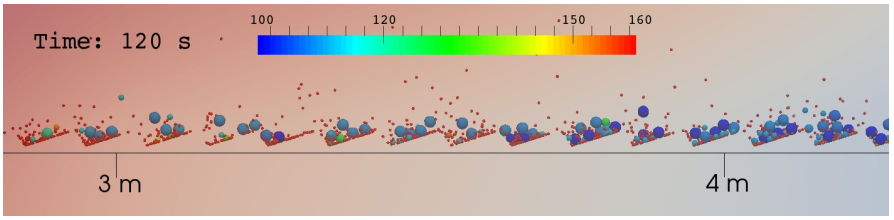

(c)

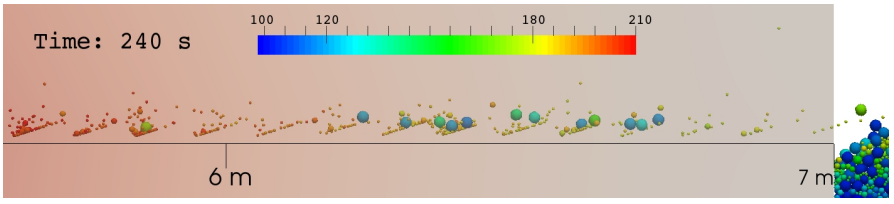

(d)

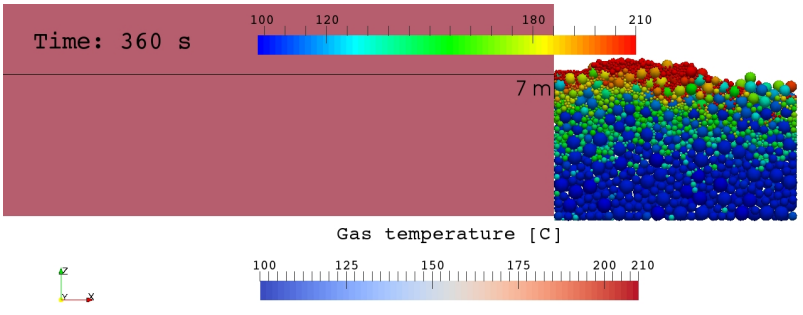

(e)

FIGURE 4.15: Temperature distribution of particles at different instances in zoomed view

4.6 Conclusion

In this chapter, the described DEM-CFD approach (Chapter.2) is applied to evaluate drying of beechwood materials in a vibrating fluidized bed dryer. Where the solid particles are modeled based on discrete element method coupled to the continuous gas phase via heat, mass and momentum transfer using OpenFOAM as a computational fluid dynamics tool. The experimental work is done through collaborating with Soil-Concept company located in Diekirch, Luxembourg. The aim of experimental tests in the industrial scale vibrating dryer is to find out the initial and final moisture contents, density and size distribution of the materials. And thereby the input parameters of the experiment are used in the simulations. The comparison of the final moisture content and residence time between experiment and simulation show good agreement conducting for further investigations. Therefore, to optimize the operation and efficiency of industrial vibrating dryer, the influence of effective parameters on drying process are investigated with defining multiple simulation cases. The predictions demonstrate that the inlet gas temperature/velocity and initial dryer temperature increase the drying rate and decrease the final moisture content of the materials. In addition, higher initial moisture content of the biomass requires more residence time to dry properly. Also the vibrating grate intensity has a major influence on the residence time so that higher intensities leads to accelerating the forward motion of the particles and reducing the terminal temperature of the materials. At the end the instantaneous temperature distribution of the particles and gas phase are visually presented to examine the effect of size distribution on drying process. It is shown that the small particles are dried faster than large particles since heat is transferred from the surface to core of particle faster.

Chapter 5

Fluidized bed hydrodynamics

5.1 Introduction

Fluidized beds are widely used in many industrial applications such as the gasification of biomass to generate biofuel. Generally, the gas-solid two-phase systems can be classified to several kinds of flow regimes such as fixed bed, bubbling fluidization, slugging fluidization, fast fluidization and turbulent fluidization, each of which the regimes occurs over a definite range of gas velocities as well as gas and solid properties. [38]

In fluid systems including moving beds in addition to the collision force which causes particles motion, the drag force is another accelerating force acting on particles so that the selection of drag models make difference in the CFD simulation of fluidized beds. Wei Du et al. in [38] has worked on the use of different drag models in the CFD modeling of a spouted bed that implies significance of different drag force acting on particles. By incorporating several widely used drag models, including Gidaspow model [39], Syamlal and O'Brien model [64], Richardson and Zaki model [65], Di Felice model [66] and Arastoopour model [67], into the two-fluid model, their influences on the CFD simulation of spouted beds are assessed. The simulation results of different drag models show that the Gidaspow model gives the best fits to the experimental data so that this model is used in this work to calculate the correlation coefficient of B_i which is discussed in section 2.4.2.1 thoroughly.

Therefore, the objective of this chapter is to investigate the flow regimes and the dynamics behavior of plastic particles in a cold flow fluidized bed by employing the described four-way Lagrangian-Eulerian coupling model (Chapter.2) whereby the pressure drop through the bed and the minimum fluidization velocity are verified by simulation and experiment.

5.2 Case definition

In order to validate the model, experimental investigations are performed with the setup shown in fig.5.1. The main part of the test rig consists of a transparent cylinder ($h = 190\ mm,\ d = 150\ mm$) with a perforated plate located at the bottom. The cylinder is filled with a packed bed with the height around 50 mm. A compressor generates a gas flow of ambient air which is introduced below the perforated plate. The axial pressure drop across the bed is measured by a differential pressure sensor and all sensor signals are recorded by a data logger which is connected to a computer. At the beginning of the experiments a monodispersed random packed bed of plastic spheres is created in the cylinder. The particle and bed properties are summarized in tab.5.1. During the experiments the air volume flow is stepwise increased until the maximum compressor power is reached. Each volume flow has been held constant for 5 min. The differential pressure across the bed is recorded with a sample time of $t_{sample} = 0.5\ s$. After reaching the maximum volume flow, the same procedure is done with decreasing volume flow. For reasons of reproducibility the measurements are repeated 3 times and the average values are used for comparison with simulation results.

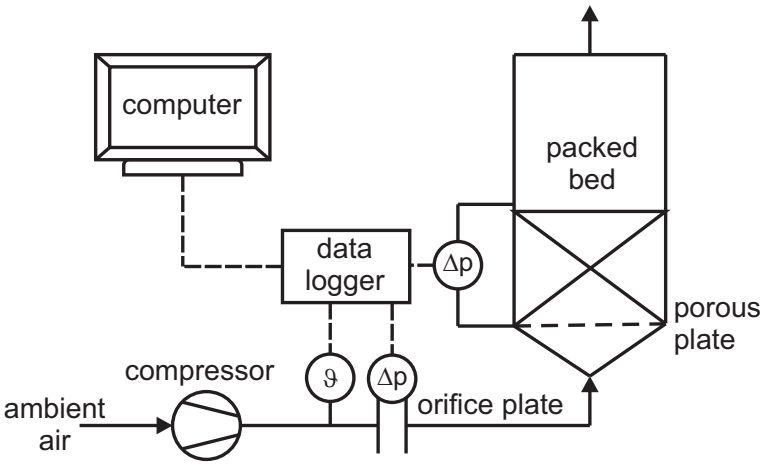

FIGURE 5.1: Schematic of the cold flow test rig

5.3 Validation

The aim is increasing superficial gas velocity to reach the moment that particles are fluidized while the bed pressure drop is recorded to compare with simulation results. In the experimental test with increasing the superficial gas velocity, the pressure drop keeps increasing until the particles start to fluidize and then the increment stops (see fig.5.2). This moment is the beginning of fluidization and the superficial gas velocity is

the minimum fluidization velocity (U_{mf}). In fact, the pressure drop balances the gravity of the bed of particles. Fig.5.2 illustrates the variation of bed pressure drop according to the various superficial gas velocities. The non-linearity of the prediction is due to the wall effect in the small scale fluidized bed used in this work. The error bars show the standard deviation (STD) value so that with increasing the flow rate, the STD value increases as expected. The pressure drop through a packed bed can also be theoretically estimated according to the Ergun equation (Eq.5.1) which is valid only for fixed beds rather than fluidized beds. It is also compared to experiment and simulation. As can be seen in fig.5.2, the prediction by DEM-CFD model is in good agreement with experiment as well as with Ergun equation at the fixed bed period.

TABLE 5.1: Properties of the plastic particles and the packed bed

Particle diameter	$d_{p,sphere}$	6 mm
Particle density	$\rho_{p,sphere}$	972.49 kg/m^3
Bed total mass	m_{bed}	500 g
Bed height	h_{bed}	$\sim$ 50 mm
Bed voidage	ε	0.4
Particles No. (app)	–	2400
Young's modulus	Y	0.1 GPa
Poisson's ratio	ν	0.29
Restitution coefficient	e	0.98
Friction coefficient	μ_f	0.3
DEM timestep	Δt_{solid}	10^{-5}
CFD timestep	Δt_{fluid}	10^{-5}

$$\frac{\Delta P}{H_{bed}} = 150\frac{\mu(1-\varepsilon)^2}{d_p^2\varepsilon^3}u_s + 1.75\frac{\rho_f(1-\varepsilon)}{d_p\varepsilon^3}u_s^2 \tag{5.1}$$

5.4 Result and discussion

In this section, the simulation results by DEM-CFD approach are presented. The simulation setup is considered as 3D configuration the same as the experimental test. Where the spherical plastic particles with diameter of $6mm$ and the bed hight of $50mm$ is employed (see tab.5.1). For optimizing the running time, a half cylinder is applied with defining a symmetry plane which is depicted the CFD domain and solid particles separately in fig.5.3. In order to consider the behavior of solid-gas simultaneously, in fig.5.6–5.20 the particles dynamics are shown in the left side while the gas flow performance in the right side. Also the white bar in the middle down indicates the included shaft in the experiment test rig and the vertical black line in the middle is the symmetry

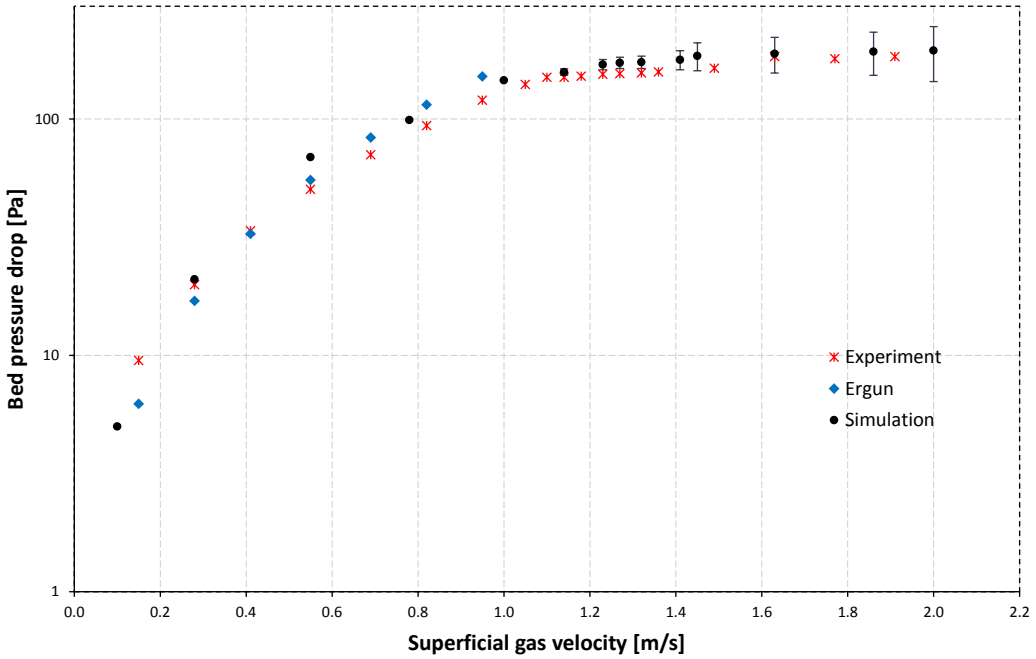

FIGURE 5.2: Bed pressure drop vs. superficial gas velocity comparing experiment, simulation and Ergun equation predictions including error bars showing standard deviation (values listed in fig.5.5)

plane. It should be noted that the O-grid technique is employed to generate mesh cells in CFD domain for capturing better results specially near the wall. In addition, the size of the CFD cells (shown in fig.5.3) are considered with regards to the initial solid volume fraction of the bed as 0.6 which is based on the experimental setup with the bed voidage 0.4 (tab.5.1).

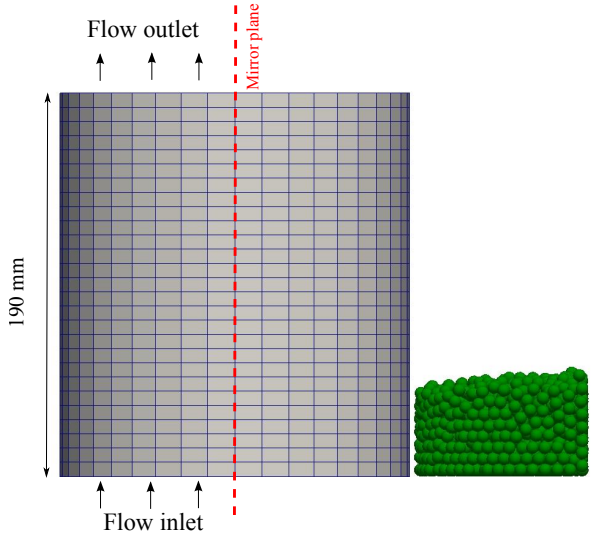

FIGURE 5.3: Simulation domain (left); packed bed of spherical plastic particles (right)

5.4.1 Pressure drop fluctuations across the bed

Fig.5.4 presents the pressure drop across the bed for different superficial gas velocities (1.0, 1.27, 1.45, 1.63, 2.0 m/s). The particle size is considered $d_p = 6\ mm$ which is the same as experiment setup. When the bed starts to fluidize, the pressure drop fluctuates around a mean pressure with chaotic behavior. It could be seen from the figure that at the superficial gas velocity of $U_g = 1.0\ m/s$, there is no pressure fluctuation meaning the bed is still fixed. With increasing air flow rate to $U_g = 1.27\ m/s$, the bed pressure fluctuates as a result of particles fluidization. This is explained as the drag force (acting on particles by gas phase) is high enough to balance the weight of particles where in this moment the particulates commence to suspend in the system. In other words, the fluctuation indicates that particles bounce because of generated bubbles inside the bed. These bubbles are due to gas motion from bottom to top of the bed. Higher air flow rate leads to higher pressure fluctuations. This could be seen in fig.5.4 that with increasing superficial gas velocity from $U_g = 1.27 - 2.0 m/s$, the absolute of fluctuation amplitudes raise to higher values according to diverse colors. This is also demonstrated as increment in sample standard deviation (STD) value so that the expansion trend is shown in fig.5.5.

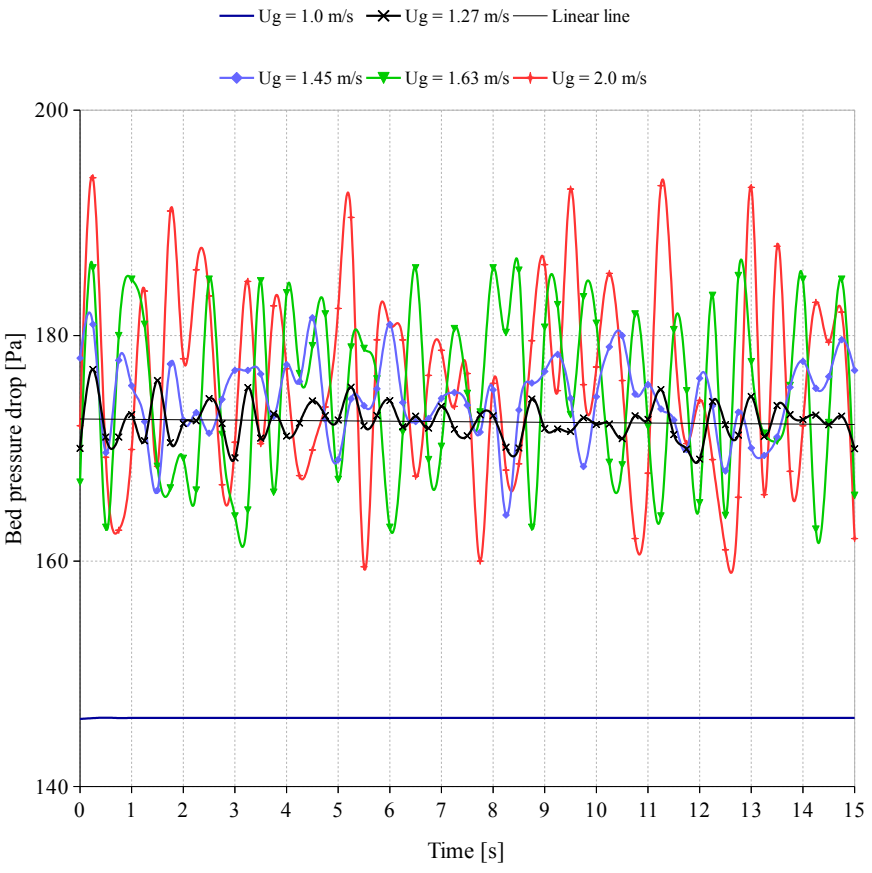

FIGURE 5.4: Pressure drop across the bed for various gas velocities

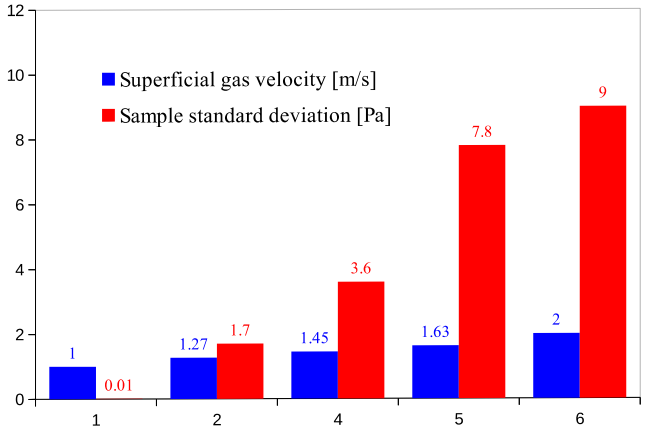

FIGURE 5.5: Sample standard deviation for different gas velocities

5.4.2 Bed pressure distribution

The scope of fig.5.6 is to illustrate pressure distribution across the bed in accordance with the air flow rate at $t = 0.25s$. The behavior is similar when time carries on, then the beginning of the simulations are only shown. This section confirms the previous part to represent the pressure gradient through the bed which is shown visually as colorful contours. It could be seen in fig.5.6(a) that with superficial gas velocity $U_g = 0.55m/s$, the bed is fixed meaning the gas velocity is lower than minimum fluidization velocity. With increasing the superficial gas velocity to $U_g = 1.27m/s$ shown in fig.5.6(b), it is visible that the particles start to fluidize a bit and the pressure drop increases. Higher values of superficial gas velocity ($U_g = 1.45, 1.63\ m/s$) leads to further motion of particles based on higher pressure drop among the bed that are shown in fig.5.6(c) and fig.5.6(d), respectively.

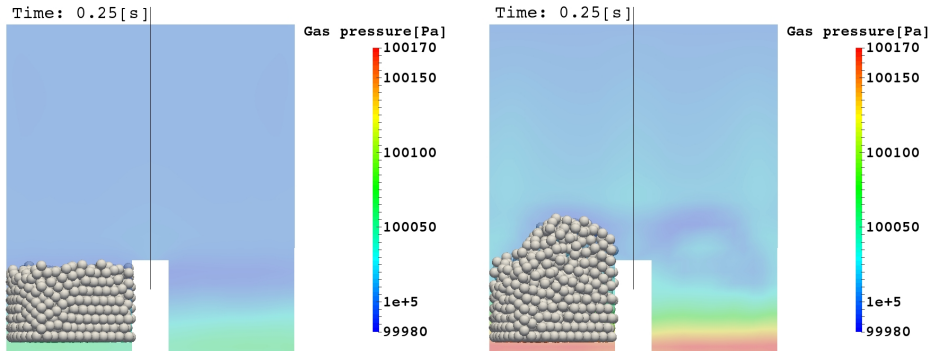

(a) $U_g = 0.55\ m/s$ (b) $U_g = 1.45\ m/s$

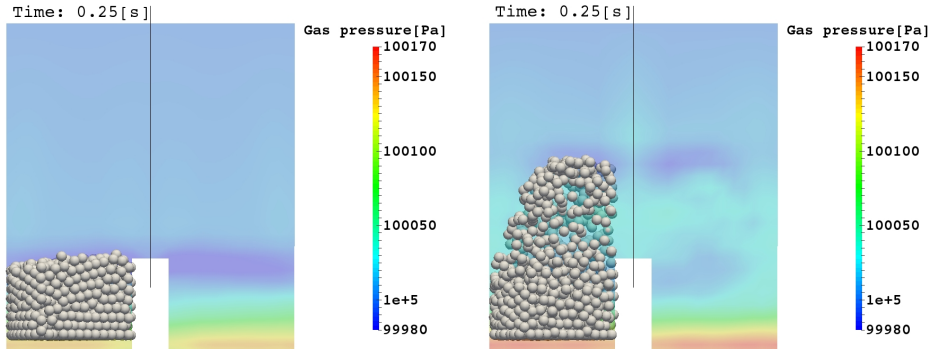

(c) $U_g = 1.27\ m/s$ (d) $U_g = 1.63\ m/s$

FIGURE 5.6: Gas pressure distribution at $t = 0.25s$ with $d_p = 6mm$ for different superficial gas velocities

5.4.3 Solid volume fraction profiles

Fig.5.7 represents time averaged solid volume fraction contour plots with particle size $d_p = 6\ mm$ for different superficial gas velocities U_g =0.55, 1.0, 1.27, 1.45, 1.63, 2.0 m/s at $t = 0.25s$. This illustrates the variation of solid volume fraction according to the change of gas flow rate. It could be seen that for low superficial gas velocities (0.55, 1.0 m/s), the particles stay fixed as a packed bed. In this case, the solid volume fraction remains constant as $\varepsilon_s = 0.6$ at highest feasible value according to the experimental setup (see tab.5.1). When the superficial gas velocity reaches $1.27m/s$, due to upward motion of particles, the compression of solid volume fraction reduces. This downward trend continues with increasing superficial gas velocity to 1.45, 1.63, $2.0m/s$ which leads to lower values at dense parts. This reduction in solid volume fraction or increment in bed voidage is considered as generated bubbles by gas flow that causes the particles to move upward. It could be mentioned that this void space is sparse remarkably at the bed top so that larger bed expansion leads to more sparseness at the upper

layers as expected. Thus, higher flow rate leads to reduce the solid volume fraction in the bed. Also the positions and normalized velocities (as color bar besides) of particles are shown in fig.5.7 for different superficial gas velocities. The initial response of the bed to fluidization takes place at $U_g = 1.27m/s$ in which some particles start to jump slightly. Consequently, with increasing the superficial gas velocity, the particles on the top layers move upward to higher height and back to the bed (due to gravity) so that they keep bouncing during air feeding.

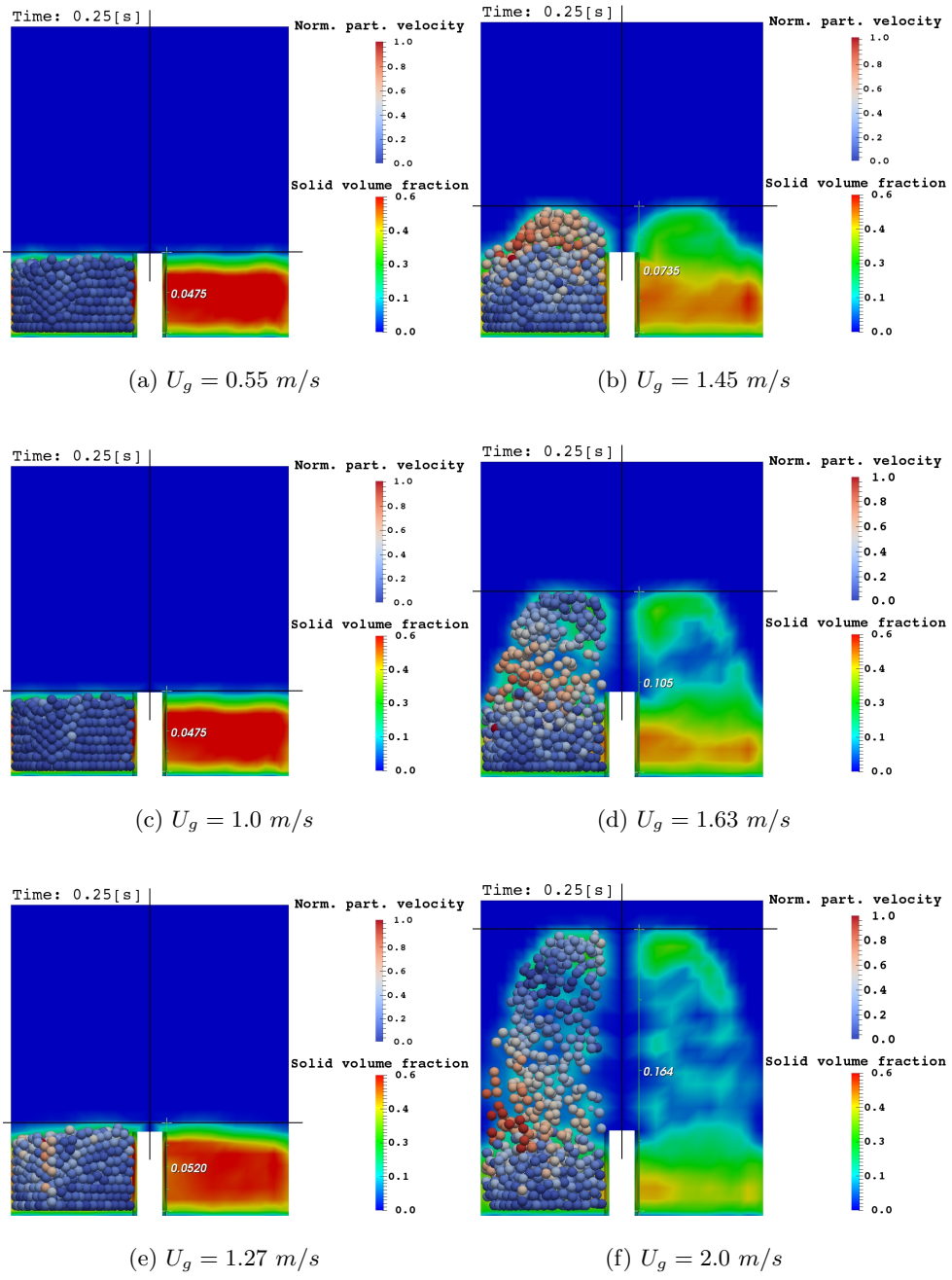

(a) $U_g = 0.55\ m/s$ (b) $U_g = 1.45\ m/s$

(c) $U_g = 1.0\ m/s$ (d) $U_g = 1.63\ m/s$

(e) $U_g = 1.27\ m/s$ (f) $U_g = 2.0\ m/s$

FIGURE 5.7: Solid volume fraction at $t = 0.25s$ with $d_p = 6mm$ for different superficial gas velocities

5.4.4 Bed expansion analysis

It could also be seen in fig.5.7 that when the gas velocity is under minimum fluidization velocity ($U_g = 0.55,\ 1.0m/s$), the particles experience no motion with the fixed bed height $H_b = 47.5\ mm$. Once the superficial gas velocity passes the minimum fluidization velocity at $1.27m/s$, the drag force reaches the particles weight. In this moment, the bed porosity increases and the particles commence to fluidize where the bed height increases to $52mm$ at $t = 0.25s$. The growth is around 4.5 mm (10%). Similarly, with enhancing the superficial gas velocity to 1.45, 1.63, $2.0m/s$, the top layer of the bed is expanded further to 73.5, 105, $164mm$ leading to 26 (55%), 57.5 (121%), 116.5 mm (245%) growth, respectively. This indicates the significant dependency of bed expansion to superficial gas velocity. The whole analysis of bed expansion including growth statistics is presented in fig.5.8. It is worth to mention that to compare the bed expansion between experiment and simulation in different flow rates, it is hard to measure a reliable bed height in experiment due to nonuniform radial distribution of particles in the bed, but remarkably similar behavior was observed in the experiments.

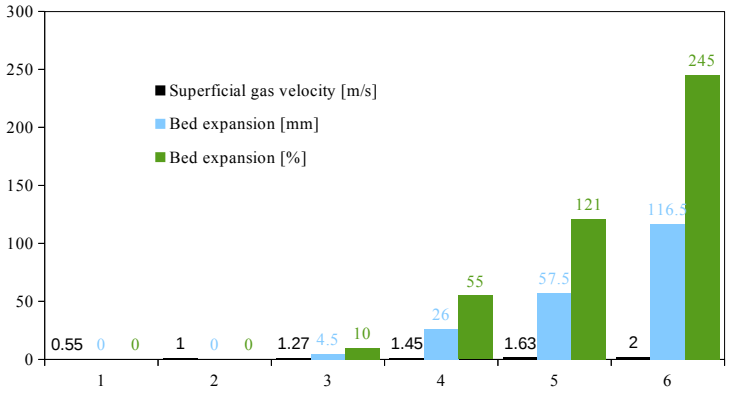

FIGURE 5.8: Bed expansion analysis for different superficial gas velocities at $t = 0.25s$

5.4.5 Effect of bed height

It is experimentally shown in Rao et al. [68] that the minimum fluidization velocity of particles increases when the bed height is increased. This is due to the wall effect and higher weight of the bed. In fact, the wall friction resists the drag force acting on the particles in addition to the bed weight during fluidization so that the higher wall friction leads to increase the minimum fluidization velocity. In this work the DEM-CFD coupling model is employed to validate with experiment considering the bed height $H_b = 47.5mm$. In order to investigate the influence of bed height on minimum fluidization velocity, two other bed heights are applied as $27.5mm$ and $66.3mm$ that are half lower and

half larger than experiment. Since at the bed height 47.5mm, the particles start to fluidize in $U_g = 1.27\ m/s$, firstly two specified heights are examined in this flow rate shown in fig.5.9-5.10. For half lower bed height (27.5mm), after 0.25s due to the less weight compared to 47.5mm, the particulates are fluidized remarkably and the bed is expanded to 74.4mm which shows 46.9mm growth (171%). To evaluate when the particles begin to fluidize in this case, the superficial gas velocity is diminished so that the first response to fluidization occurs at 1.0m/s shown in fig.5.11. In contrast, increasing the bed height to half higher than experiment (66.3mm), the bed has no significant movement at $U_g = 1.27m/s$. This is due to the weight gain and higher wall friction that is shown in fig.5.10. That is the particles require higher flow rate to fluidize. The evaluation is done with raising U_g so that at 1.63m/s the bed motion is shown in fig.5.12. It could be seen that the bed is expanded to 119mm showing 53mm growth (80%). As a result, the minimum fluidization velocity of particles increases when the primary bed height is grown.

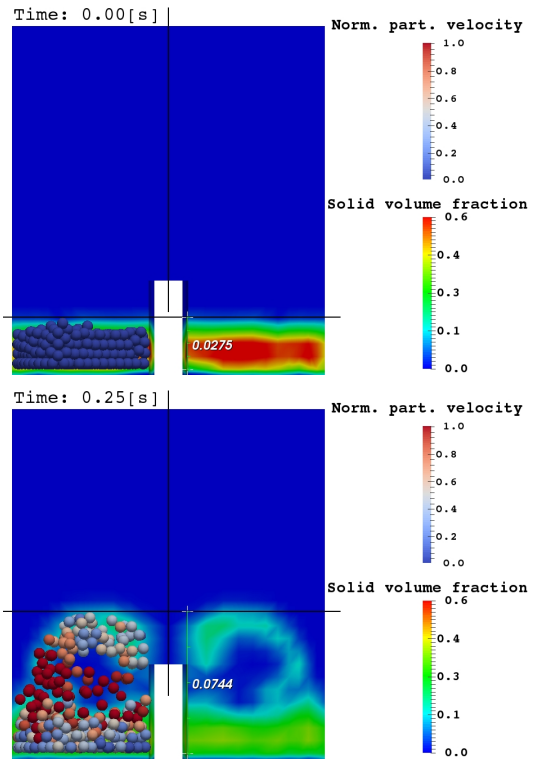

FIGURE 5.9: Solid volume fraction with $d_p = 6mm$, $U_g = 1.27m/s$ and $H_b = 27.5mm$ at 0, 0.25s

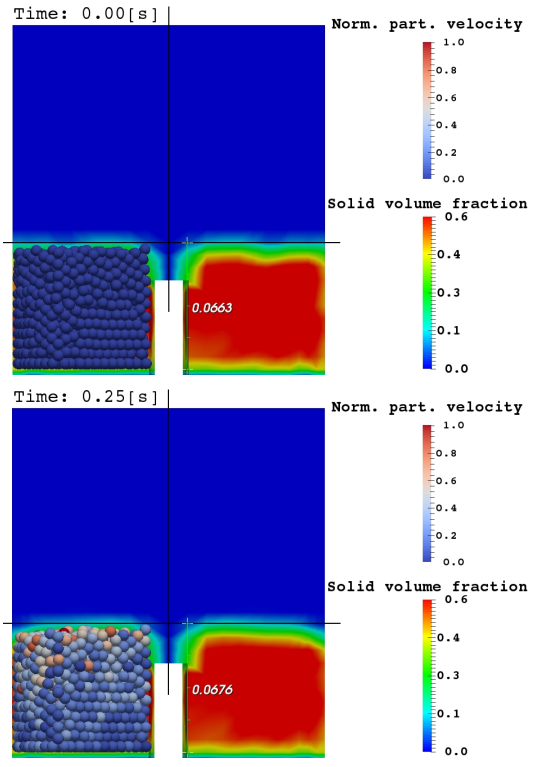

FIGURE 5.10: Solid volume fraction with $d_p = 6mm$, $U_g = 1.27\ m/s$ and $H_b = 66.3\ mm$ at 0, 0.25s

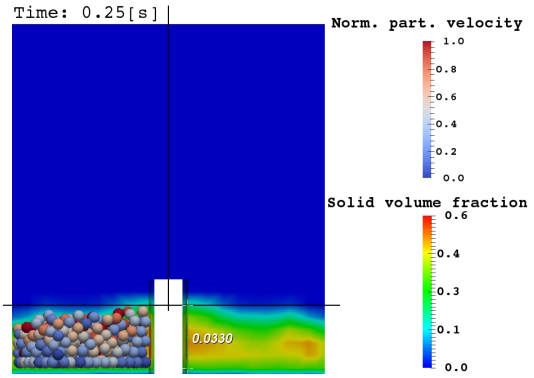

FIGURE 5.11: Solid volume fraction with $d_p = 6mm$, $U_g = 1.0m/s$ and $H_b = 27.5mm$ at $0.25s$

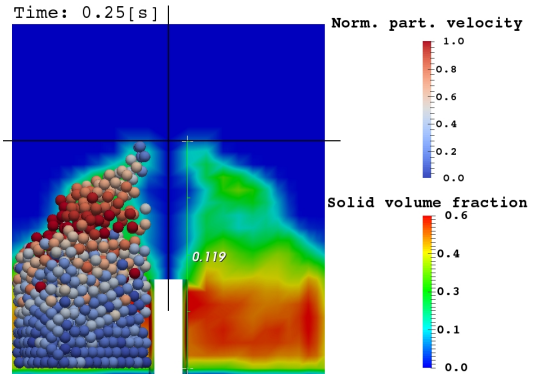

FIGURE 5.12: Solid volume fraction with $d_p = 6mm$, $U_g = 1.63m/s$ and $H_b = 66.3mm$ at $0.25s$

5.4.6 Effect of particle size

The purpose of this section is to assess the influence of particle size on minimum fluidization velocity and bed expansion. The base particle size according to experiment is $6mm$. And two other sizes as half smaller and half larger (3, $9mm$) are applied where the bed height for all cases is held almost the same. The intention is to keep the bed bulk volume as equivalent as possible. That is for $d_p = 3,\ 6,\ 9mm$, the bed height considered in the simulation is 45.3, 47.5, 47 mm, respectively. The small difference is due to particle diameter so that adding one layer makes the bed height less appropriate. Then two mentioned sizes are simulated at $U_g = 1.27\ m/s$ to compare with particle size $d_p = 6mm$. It could be seen from fig.5.13 that the size $d_p = 3mm$ experiences high bed expansion at $t = 0.25s$ showing $122mm$ growth (269%). In contrast, the particle size $d_p = 9mm$ responds no motion at $U_g = 1.27\ m/s$ which is shown in fig.5.14. In fact, when the particle size increases, the solid surface area which encounters to the gas flow is also increased. This leads to higher resistance between solid-gas phase. In order to find the minimum fluidization velocity in each case, the flow rate changes correspondingly. That is the superficial gas velocity for smaller size ($3mm$) is decreased so that at 0.87 m/s the particles start to fluidize as shown in fig.5.15. Contrary to the smaller size, the superficial gas velocity needs to grow for fluidization of larger particles ($d_p = 9mm$). In this case, it is increased to higher values so that at 1.67 m/s the particles commence to move as shown in fig.5.16 at $0.25s$ and it carries on afterwards.

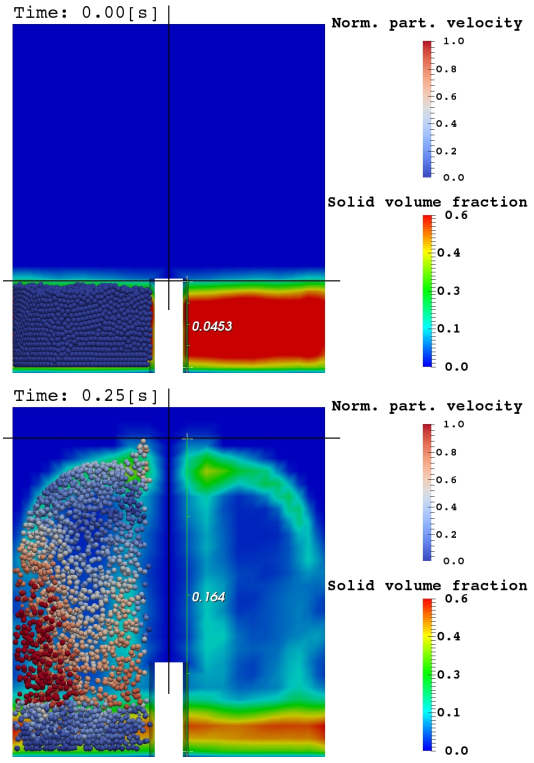

FIGURE 5.13: Solid volume fraction with $d_p = 3mm$, $U_g = 1.27m/s$ and $H_b = 45.3mm$ at 0, $0.25s$

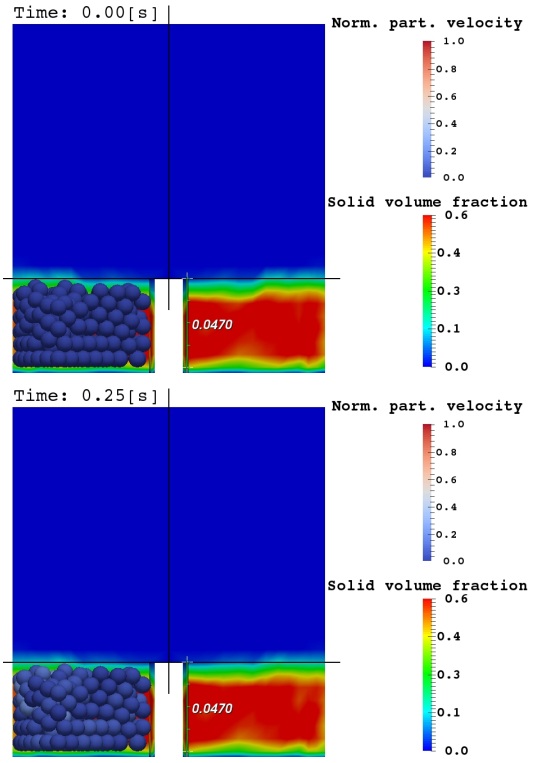

FIGURE 5.14: Solid volume fraction with $d_p = 9mm$, $U_g = 1.27\ m/s$ and $H_b = 47mm$ at 0, $0.25s$

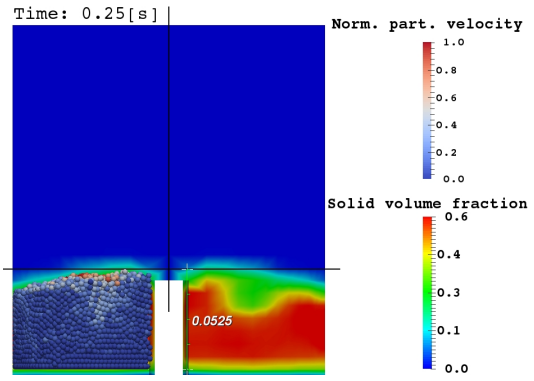

FIGURE 5.15: Solid volume fraction with $d_p = 3mm$, $U_g = 0.78m/s$ and $H_b = 45.3mm$ at $0.25s$

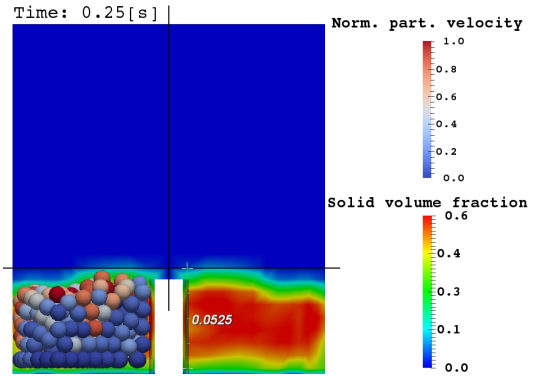

FIGURE 5.16: Solid volume fraction with $d_p = 9mm$, $U_g = 1.67m/s$ and $H_b = 47mm$ at $0.25s$

5.4.7 Effect of air density with temperature variation

The air properties for various temperature are shown in tab.5.2 and fig.5.17 graphically according to Incropera [69]. When air temperature increases, the density decreases

while the viscosity increases. In this section the influence of air temperature on bed motion is investigated with respect to excluding any conversion process. Since the base temperature is the ambient temperature ($25°C$), the related data is interpolated in tab.5.2 shown as red values . Then the prediction of bed motion in three different temperature $T_g = 25$, 60, $95°C$ at $U_g = 1.51\ m/s$ is illustrated in fig.5.18. With raising air temperature and accordingly reducing air density as well as increasing air viscosity, the bed height diminishes from 0.0794 to 0.065 and 0.0607 m, respectively. In another words, the volume of generated bubble through the bed lessens with respect to the increase in solid volume fraction inside the bed. The latter is distinguished according to the color bar alongside. This states that lowering air density due to air temperature increment leads to increase the minimum fluidization velocity. This tendency is shown in fig.5.21 quantitatively.

TABLE 5.2: Thermophysical properties of air at atmospheric pressure from Incropera

$T\ [K]$	$\rho\ [kg/m^3]$	$c_p\ [kJ/kg.K]$	$\mu \times 10^7\ [Ns/m^2]$	$\alpha \times 10^6\ [m^2/s]$	Pr	$Ref.$
250	1.3947	1.006	159.6	15.9	0.720	[69]
298	1.1707	1.007	183.6	22.2	0.707	
300	1.1614	1.007	184.6	22.5	0.707	
350	0.9950	1.009	208.2	29.9	0.700	
400	0.8711	1.014	230.1	38.3	0.690	
450	0.7740	1.021	250.7	47.2	0.686	
500	0.6964	1.030	270.1	56.7	0.684	
550	0.6329	1.040	288.4	66.7	0.683	
600	0.5804	1.051	305.8	76.9	0.685	
650	0.5356	1.063	322.5	87.3	0.690	
700	0.4975	1.075	338.8	98.0	0.695	
750	0.4643	1.087	354.6	109	0.702	
800	0.4354	1.099	369.8	120	0.709	

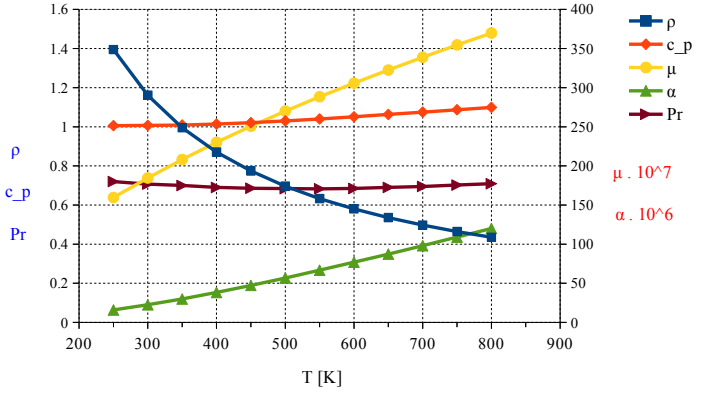

FIGURE 5.17: Variation of air properties vs. air temperature

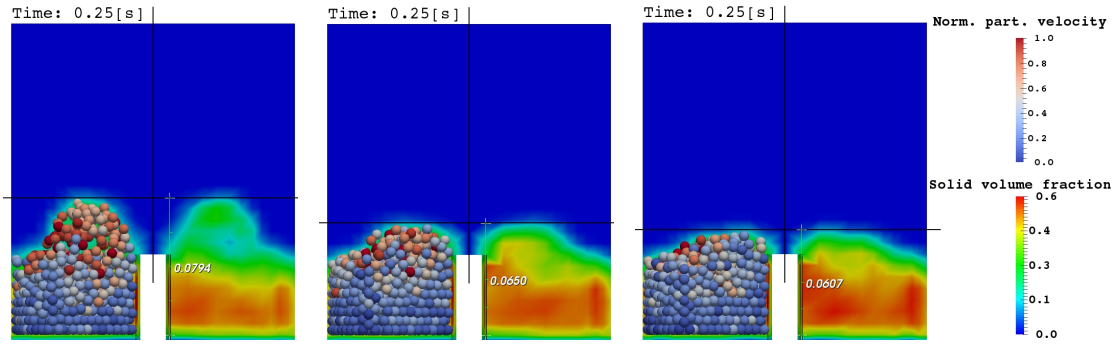

FIGURE 5.18: Solid volume fraction and bed expansion with $d_p = 6mm$ and $U_g = 1.51m/s$, for various dry air temperature $T_g = 25°C$ (left); $60°C$ (middle); $95°C$ (right)

5.4.8 Effect of air density with water vapor variation

So far dry air is used as gas medium to fluidize particles in the system. In this section the influence of water vapor on minimum fluidization velocity is investigated. Generally at the same temperature and pressure, the number of molecules for the same volume of gas are equal. In addition, the weight of water vapor molecules (H_2O) is less than dry air molecules ($O_2 + N_2$). In another words, the same volume of vapor-air mixture has less weight than the same volume of dry air. This means the vapor-air mixture has less density than dry air and it is expected to increase the minimum fluidization velocity. According to the ideal gas law, the relationship between density, pressure and temperature for dry air is defined as $p = \rho RT$ where $R = 286.9\ [J/kgK]$ is gas constant for dry air. On the other hand, the ideal gas law for vapor-air mixture is described in Eq.5.2 which is based on Stull [70]. Where T_v is called *virtual temperature* and defined for temperature under saturation with r as vapor-air mixing ratio.

$$p = \rho R T_v \tag{5.2}$$

$$T_v = T\ (1 + 0.61\ r) \tag{5.3}$$

That is the vapor-air mixture with temperature of T behaves like dry air with temperature of T_v. So assuming the same temperature and pressure, with increasing water vapor content of the gas flow, the vapor-air mixture density decreases while the viscosity increases. Fig.5.19 demonstrates the variation of air density, viscosity and virtual temperature versus vapor-air mixing ratio. Therefore, three different vapor-air mixing ratios ($r = 0.2, 0.4, 0.6$) are considered and simulated to find out the influence of density change on minimum fluidization velocity. It could be seen from fig.5.20 that at the

same superficial gas velocity ($U_g = 1.4\ m/s$), the bed motion is reduced with respect to decrease in bed height to 0.0639, 0.06, $0.055m$ respectively. Furthermore, the bubble inside the bed is diminished and solid volume fraction through the bed is grown. This is due to the fact that lower air density requires higher minimum fluidization velocity to move the bed. At the end, fig.5.21 predicts the variation of minimum fluidization velocity according to density change due to air temperature and vapor-air mixture ratio variation quantitatively. It clarifies that air density reduction leads to raise the minimum fluidization velocity.

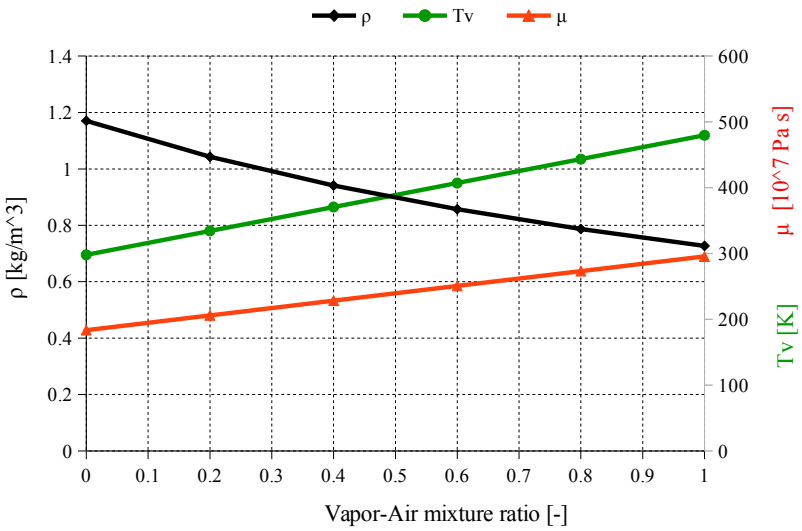

FIGURE 5.19: Variation of air density, viscosity and virtual temperature vs. vapor-air mixture ratio

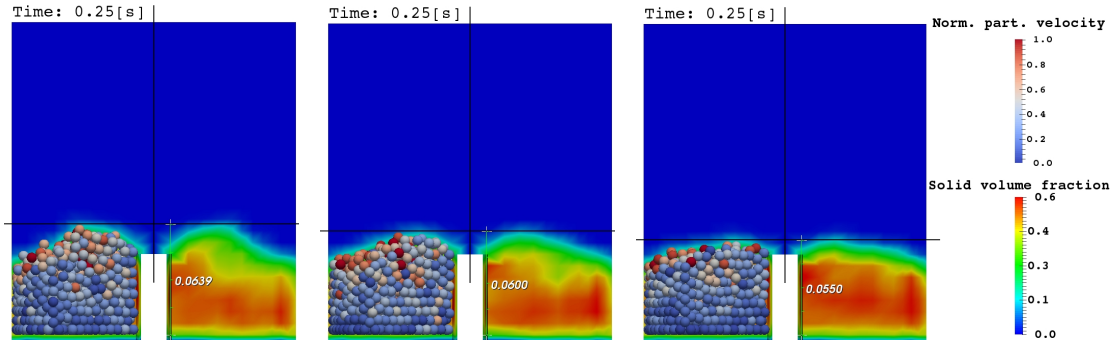

FIGURE 5.20: Solid volume fraction and bed expansion with $d_p = 6\ mm$ and $U_g = 1.4\ m/s$, for various vapor-air mixing ratio $r = 0.2$ (left); 0.4 (middle); 0.6 (right)

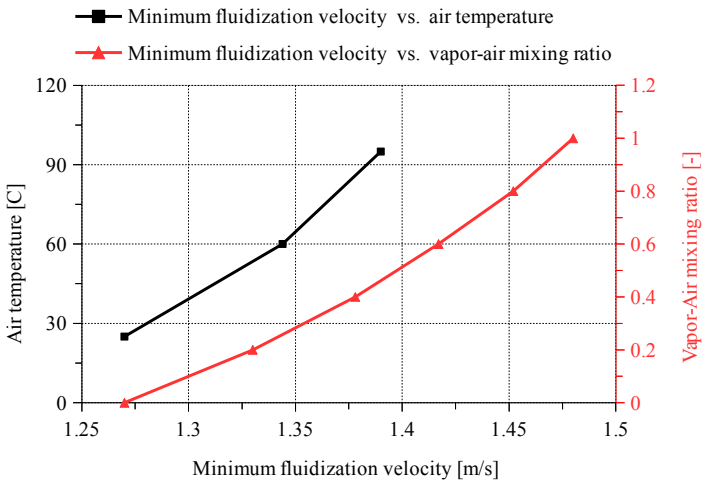

FIGURE 5.21: Variation of minimum fluidization velocity vs. air temperature and vapor-air mixing ratio

5.5 Conclusion

In this chapter, the interaction between the air flow and a packed bed of plastic spheres is investigated experimentally and numerically using the described four-way DEM-CFD coupling model. The four-way coupling stands for considering both particle-particle collisions and fluid-particle interactions with influence of the drag force on particles. The latter is modeled using Gidaspow approach. In order to validate the model, the experimental work is performed in Technische Universität Dresden laboratory, Germany. And the pressure drop across the bed is compared between experiment, simulation and theoretical calculation by Ergun equation and the result shows an adequate agreement. Furthermore, presenting pressure drop fluctuation through the bed indicates that after reaching the superficial gas velocity to minimum fluidization velocity, the particles start to fluidize and pressure fluctuates around a mean pressure so that increasing the superficial gas velocity leads to higher fluctuation indeed. It is also shown the influence of superficial gas velocity on instantaneous particle position and velocity as well as bed expansion. It is stated that higher flow rate leads to faster motion of particles and larger bed expansion. The effect of bed height and particle size on minimum fluidization velocity is also denoted. In fact, the superficial gas velocity should increase to fluidize higher bed height and larger particles due to wall effect, higher bed weight and bigger surface area facing with the gas phase. At last, it is shown that reducing air density because of higher air temperature and higher vapor-air mixing ratio leads to increase the minimum fluidization velocity.

Chapter 6

Fluidized bed conversion

6.1 Introduction

Fluidized beds are widely used in chemical applications in industry like biomass conversion to generate biofuel. The ability of fluidized beds are suspending the solid materials inside the reactor so that they can be mixed in a better way with the gas flow leading to uniform heat transfer. This is due to the fact that heat transfer by gas phase to the solid fuel is very important in conversion process. Generally, biomass conversion inside the fluidized beds are complex due to simultaneous heat, mass and momentum transfer between solid-gas phase. In order to get better prediction close to experiment, the solid-gas interactions through conversion and dynamics need to be considered properly according to the relevant governing equations.

At sufficiently high fluid velocities inside the fluidized beds, the frictional force between solid-gas phase balances the particles weight. In this state, the solid particles and related gas velocity are referred to fluidized particles (because of fluid-like behavior) and the minimum fluidization velocity, respectively. With increasing the gas flow rate beyond the minimum fluidization velocity, the fluidized bed reactors can be operated in various fluidization regimes. Concerning chemical reactions, the fluidized bed reactors are particularly suitable for highly exothermic and temperature-sensitive reactions since the solid particle motion gives them a unique ability to rapidly transport heat and maintain a uniform temperature [71].

During conversion of biomass into gaseous fuel in a fluidized bed, the physical and chemical processes as heat-up, drying, pyrolysis, combustion and gasification of char take place. The heat-up is identified as providing heat to the system to increase the temperature of solid particles above the ambient temperature. When the surface temperature

of particle achieves the saturation status (around $100°C$ in $1bar$), the water contents of particles start to vaporize whereby the drying process begins. After removing the water content and with increasing heat, the biomass fuel starts to decompose thermally to char, tar and volatiles ($CH_4, CO, CO_2, H_2, H_2O$). This stage is recognized as pyrolysis or devolatilization process. The released heat from reactions between volatile gases and oxygen is used for drying and pyrolysis of new feeding biomass fuel to the reactor and producing further volatiles so that this cycle continues as far as the oxygen is provided to the system. The remaining char from thermal decomposition is gasified via reacting with CO_2 and H_2O to generate useful gases CO, H_2 which are highly combustible. Also char is oxidized at high temperature above $700°C$ denoting the combustion process when the solid char reacts with oxygen for releasing heat.

All mentioned processes that take place through homogeneous (with volatiles) and heterogeneous (with char) reactions are discussed in Chapter 2. It is worth to note that thermal energy required for endothermic drying, pyrolysis and gasification reactions is supplied from exothermic combustion of volatiles. The described physical and chemical processes are shown in fig.7.1. In general, the materials including hydrogen and carbon such as biomass, natural gas and agricultural residues are suitable for combustion. A certain quantity of fuel and air leads to complete combustion which is 21% of O_2 and 79% of N_2 in a stoichiometric combustion reaction shown in Eq.6.1.

$$Biomass + (0.21O_2 + 0.79N_2) \rightarrow CO_2 + H_2O + (0.79N_2) + Heat \tag{6.1}$$

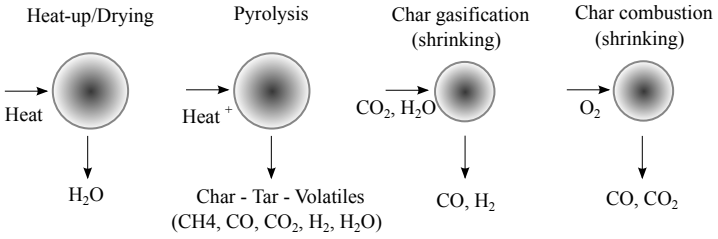

FIGURE 6.1: Main steps of conversion process

Although, the complete combustion is only theoretically possible due to heat loss. Therefore, for complete combustion it is required some extra air feeding to the combustion chamber referred to excess air quantity. Also analysis of flue gas emissions is required to improve combustion efficiency. One great environmental concern which is desirable refers to produce less amount of CO. It could be improved with adding a secondary

inlet above the bed that converts toxic and harmful CO to CO_2 which is released to the atmosphere and it is considered in the case study in this chapter.

Basically, biomass conversion depends on different parameters such as amount of produced volatile matter, yielded char, particle size, reactants partial pressure, reactor temperature and residence time. Many works are done concerning biomass conversion in various types of fluidized beds experimentally and numerically. Tremel and Spliethoff [72] have studied volatile yield, char specific surface area, and char reactivity after pyrolysis experiments in a pressurized entrained flow fluidized bed. It is concluded that the devolatilization behavior of the solid fuels and the reactivity of the resulting char are important design parameters for entrained flow gasifiers. The experimental data indicate that the devolatilization rate is significantly faster than the char deactivation rate. In addition, Baruah [73] categorizes the recent modeling works based on certain specific criteria such as type of gasifier, feedstock, modeling considerations and evaluated parameters. Apparently, feed stock flow rate, gasifying agent flow rate, equivalence ratio, reactor pressure and temperature are some of the important operating parameters which influence the gasification process. Change in a parameter has considerable effect on the flue-gas composition and hence on the performance of the gasifier.

Furthermore, Babu in [74] predicts the composition and temperature profiles across the length of the reduction zone using a steady state equilibrium model. It is shown that the char reactivity factor is the key parameter in modeling the downdraft gasifier, and it directly represents the reactivity of the char in the reduction zone. Melgar et al. [75] has proposed a thermochemical equilibrium model for downdraft gasifiers to predict the final produced gas composition and its main characteristics such as heating value and engine fuel quality for a biomass with a defined ultimate composition and moisture content. The reaction temperature is considered to be the driving parameter of the whole gasification process and calculated considering thermal equilibrium. Through the energy equation, the reaction temperature corresponding to a certain fuel/air ratio and moisture content is obtained, thereby the reaction temperature is estimated.

Besides, Gao and Li [76] simulated the behavior of a fixed bed biomass gasification reactor to study the effect of a continuously increasing heating rate and fixed temperature of the pyrolysis zone on the flue-gas composition in the reduction zone. It was observed that for a continuous heating rate of the pyrolysis zone, the concentrations of H_2 and CO increased while those of N_2 and CO_2 decreased with increasing reaction temperature. The CH_4 content increased during the reaction time and at the end of the reaction the concentration decreased. Similar observations were made for H_2O fraction. For a constant pyrolysis temperature, CO_2 decreased and CH_4, H_2, CO and H_2O increased

with reaction time. In both modes, the trends of temperature profile and species concentrations were found to be very different. Thus, it is observed that while modeling the pyrolysis and reduction zones together, the temperature profile of the pyrolysis zone has significant effect on the gas composition in the reduction zone. [73]

Also Azzone et al. [77] developed an equilibrium model for the simulation of thermochemical gasification and application to agricultural residues. The model behavior was analyzed by varying process parameters (pressure, temperature), biomass humidity and oxidant agent composition. It is proved that by increasing the pressure in the gasifier, the methane fraction increased. This was due to the fact that the equilibrium constant is inversely proportional to the process pressure. [73]

Since the biomass materials have layered behavior similar to an insulator, the suitable model for biomass is either slab or cylinder where the latter is applied in this study. Recently, the studies in terms of modeling non-spherical particles have been increased significantly. For instance, in Lu et al. [78] the DEM modeling for non-spherical particle systems is reviewed remarking the advances in shape representation algorithms and efficient detection of contacts. Furthermore, Zhong et al. [79] reviews extensively the theoretical developments and applications of DEM modeling in non-spherical particle systems. Also Dziugys and Peters in [80] introduce a new algorithm to calculate analytically the overlap of two-dimensional ellipses based on the general equation of superquadratics.

In this work, the cylindrical particle with non-spherical shape is replaced by a sub-spherical configuration. Where fig.6.2 shows a cylindrical particle represented by sub-spheres which approximately fills the original particle shape. This method is originally proposed by Nolan et al. [81]. In this approach, it is assumed that the sub-spheres could have different sizes and initial overlap in between, but the whole shape remains a rigid body with constant distance between sub-spheres. That is, the contact between original shapes is considered as contacts between their sub-shapes which means the contact detection remains the same as spherical contacts for simplicity. It should be noted that the total force and torque acting on a non-spherical particle is calculated based on total forces and torques of the sub-shapes, but at the center of gravity of the original shape. It could be also feasible to improve the approximation by increasing the number of sub-spheres. Although, this method specifies the original shape with no absolute precision, but with an acceptable approximation for applications. [28]

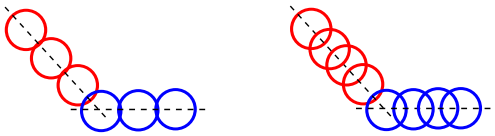

FIGURE 6.2: Sub-spherical particles representing cylindrical shape; left: simple, right: packed

Moreover, in particle scale modeling it is assumed that particles are isotropic and properties change along the radius. The distribution of temperature and species within the particles are accounted for by a system of one-dimensional and transient conservation equations. By the fact that solid particles lose their mass through drying, pyrolysis, combustion and gasification; but solid fuel shrinkage is considered exclusively during wood and char consumption due to negligible volume change during drying. [16]

Basically, shrinkage improves heat and mass transfer due to surface reduction. The latter accelerates the heat and mass to reach the particle center faster because of smaller dimensions [82]. In the shrinking model in this work, it is assumed that the char formation during pyrolysis and consumption by gasification and combustion is in the outermost cell (V_{cell}) of the particle. That is evaluated as a shrinking volume (V_{shrunk}). While the particle shrinks uniformly in radial direction, the original shape of the particle remains unchanged. Where the porosity and size of the particle vary in such a way that char reaction rate ($\dot{w}_{char}$) in the boundary cell of the particle influences the shrinking volume thereby the reduced size of particle (r_{new}) is defined as:

$$V_{shrunk} = \frac{\dot{w}_{char} * V_{cell}}{\rho_p} \tag{6.2}$$

$$r_{new} = \sqrt{\frac{V_p - V_{shrunk}}{\pi \; l}} \tag{6.3}$$

And it is assumed that the reactions taking place inside particle increase the porosity of particle instead. The particle size reduction due to shrinking is shown in fig.6.3 where the circles inside the particle show the number of arbitrary cells that are defined in the particle modeling. After reduction the particle with new size is generated with the same number of cells for numerical stability. The shrinking model is applicable for different shapes such as slab, sphere and cylinder where the latter is considered in this work.

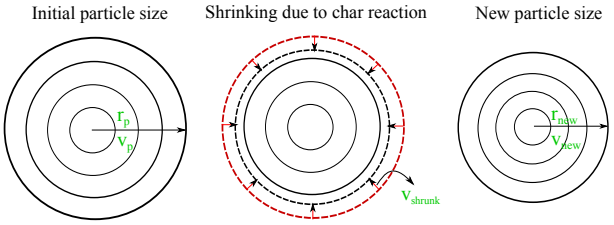

FIGURE 6.3: Shrinking procedure during char conversion

The main operating parameters that affect the fluidized bed behavior are the reactor temperature, equivalence ratio, fuel particle size and bed motion. The aim of this section is applying the described Lagrangian-Eulerian coupling module (in Chapter 2) to predict biomass conversion in a bubbling fluidized bed reactor with considering the dynamics behavior of granular flow mixing as well as physical and chemical processes simultaneously. At first, the conversion behavior of a single pellet particle is evaluated with experimental data from literature and then a moving bed of particles inside the fluidized bed is considered.

6.2 Case definition

The simulation case employed in this study is a cylindrical fluidized bed reactor based on the work by Wiese et al. [41] as shown in fig.6.4. In order to evaluate the conversion of biomass fuel, a single cylindrical beechwood particle is simulated at two different wall reactor temperature (700, $800°C$) where tab.6.1 presents the proximate and ultimate analysis of biomass fuel. In addition, the particle and gas properties are listed in tab.6.2 and 6.3. There exist two inlets and one outlet at top right of the reactor. The primary inlet is injecting from the bottom and passes the underneath grate and the bed of particles. It is noted that in the simulation case, there is a gap ($20mm$) between the primary inlet and the particles grate to consider the developed flow reaching the particles. While the secondary inlet is located at $88mm$ above the grate that flows through a distribution chamber surrounding the reactor and enters via circular air inlet. The position of the secondary inlet is considered so that the bed height during full load operation is underneath.

In this case study, the main heat is significantly provided by the hot wall with $700-800°C$ based on the radiation from the combustion chamber to the particle surface. Between the particles, both radiative and conductive heat transfer is evaluated in addition to considering the radiation between particle-gas phase. Generally in fixed beds, the radiative heat transfer is considered only between the gas and particles on the bed surface

according to the visibility between solid-gas. This means the particles inside the bed achieve less energy. While in fluidized beds due to instantaneous motion of particles and updating the surface visibility among the particles and gas phase, the radiative heat transfer is considered for all particles. As stated, to describe the heat and mass transfer within the particle, each element is spatially divided into multiple radial cells where the resolution of the particle discretization is determined by the number of cells. In this work since the radius of cylindrical particles is $6mm$, the number of cells in radius direction is 6 for each particle. Besides, the convective heat transfer between the solid and gas phase is calculated by Nusselt correlation of Wakao [83] and the relative convective mass transfer is analogical to the convective heat transfer with Sherwood number instead. The reaction modeling is based on Partially Stirred Reactor (App.A) in combination with $k - \epsilon$ turbulence model.

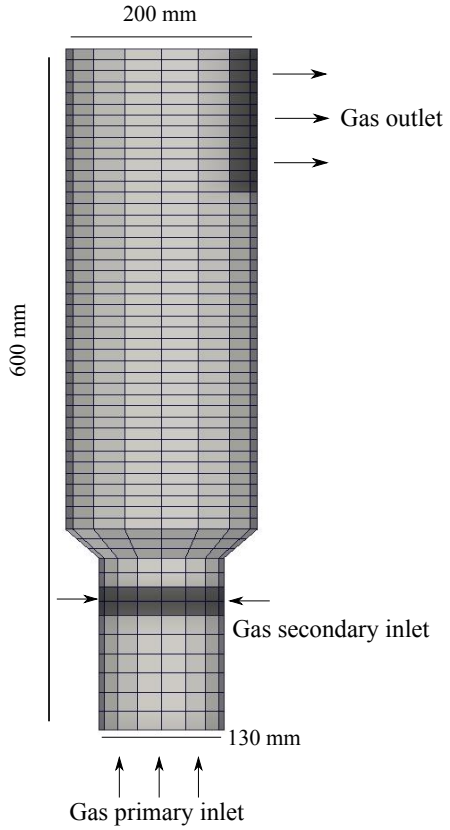

FIGURE 6.4: Gas CFD domain with primary and secondary inlets and upper outlet

TABLE 6.1: Initial and final fuel composition

Proximate Analysis - As-Received basis [41]	
$Moisture\ (wt.\%)$	6.82
$Fixed\ carbon\ (wt.\%)$	14.39
$Ash\ (wt.\%)$	0.19
$Volatiles\ (wt.\%)$	78.6
$HHV\ (MJ/kg)$	17.38
Ultimate Analysis - dry and ash free(daf) basis [41]	
$C\ (wt.\%)$	51.7
$H\ (wt.\%)$	6.13
$N\ (wt.\%)$	0.23
$O\ (wt.\%)$	41.9
$S\ (wt.\%)$	0.04

TABLE 6.2: Properties of the beechwood cylindrical particle

diameter	d_p	6 $[mm]$
length	l_p	16.5 $[mm]$
density	ρ_p	1220 $[kg/m^3]$
initial temperature	T_0	25 $^\circ[C]$
initial water content	X_0	1.1 $[g\ water/g\ dry\ solid]$
$Young's\ modulus$	Y	0.1 $[GPa]$
$Poisson's\ ratio$	ν	0.29
restitution coefficient	e	0.98
friction coefficient	μ_f	0.3
specific heat	c_p	$1.5 + 0.001\ T$ $[kJ/kg]$
conductivity	λ	0.47 $[W/mK]$
permeability	K	0.02
pore diameter	$-$	50 $[\mu m]$
particle porosity	ε_p	0.64
particles No. (app)	$-$	1000
DEM timestep	Δt_{solid}	10^{-5} $[s]$
CFD timestep	Δt_{fluid}	10^{-5} $[s]$

TABLE 6.3: Properties of the inlet air flow

pressure	P	1 $[bar]$
temperature	T_g	25 $[^\circ C]$
density	ρ_g (25 $^\circ C$)	1.1707 $[kg/m^3]$
primary-air volume flow rate	$\dot{v}_{g,1}$	0.0023 $[m^3/s]$
secondary-air volume flow rate	$\dot{v}_{g,2}$	0.0046 $[m^3/s]$

6.3 Validation

In order to evaluate the biomass conversion with shrinkage, a single pellet particle is investigated based on [41]. Two conditions are performed for each wall temperature (700, 800°C) considering with and without the shrinking model. The prediction of mass loss tendency for the cylindrical particle is compared with experiment and shown in fig.6.5 where the mass loss could be divided to four steps. In case of wall temperature 700°C, since the particle is initiated in 25°C, the first step is heat-up which is very fast due to high radiative heat transfer by wall. Then drying starts after reaching the particle temperature to saturation status. In this period which lasts 35s, the temperature of particle remains constant and there is an equilibrium between water liquid and vapor inside the particle. Subsequently, the devolatilisation commences with converting beechwood to char, tar and volatile matters where the particle starts getting shrunk and more porous. Afterwards, with leaving the volatiles from the particle, the oxygen can enter the pore space of the particle where the combustion of char starts. In addition, char gasification is done due to reaction with steam and carbon dioxide released by volatiles combustion with the surrounding gas phase. It is clear that all processes take place in a faster rate for the wall temperature 800°C rather than 700°C. This means the conversion ends up faster due to higher heat transfer rate. As expected, the predictions of conversion including the shrinking model give improved agreement with experiments for both wall temperature.

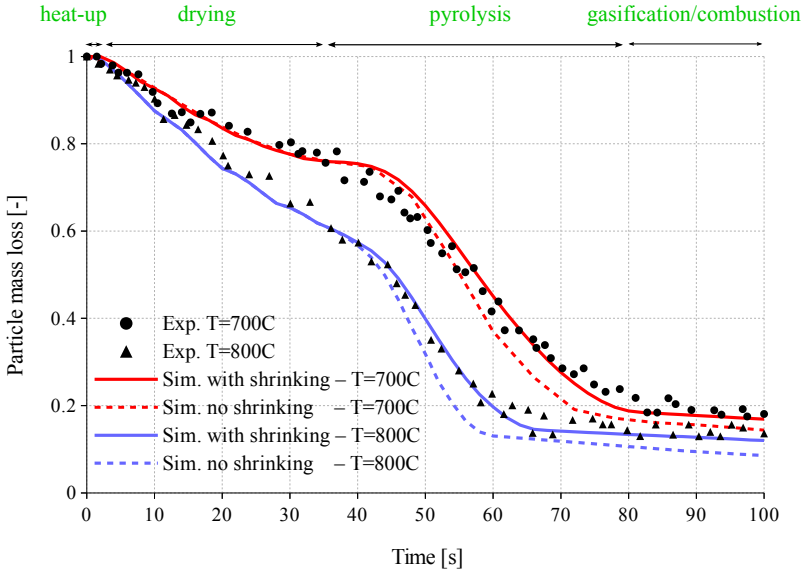

FIGURE 6.5: Validation of cylindrical particle mass loss with experiment for two wall temperature 700, 800°C

In addition, fig.6.6 complements the effect of shrinking model based on the particle porosity and radius change for wall temperature 700°C. When the pyrolysis commences after 35s, while the particle radius remains unchanged for the model without shrinking, the particle porosity still tends to increase because of continuous mass loss. In contrast, the prediction including the shrinking model leads to radius reduction due to shrinkage; while the particle porosity keeps reducing as expected. In the model including the shrinkage, there exist two different rates starting from 40s and 80s which denote the onset of pyrolysis and combustion periods respectively. The hill at 80s, showing an increment in porosity, is explained as the beginning of particle combustion where the volatiles from pyrolysis are exited and oxygen can go through the pore space of particle.

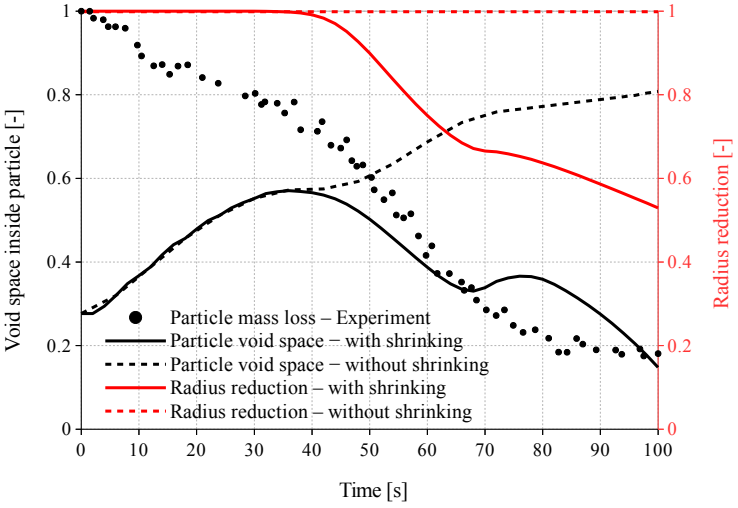

FIGURE 6.6: Particle porosity and radius reduction with and without shrinking model for $T_{wall} = 700\ °C$

Besides, fig.6.7 represents the behavior of particle core temperature and it's rate during conversion of the cylindrical beechwood particle for $T_{wall} = 700°C$. At the beginning of simulation, since the particle is initiated at ambient temperature (25 $°C$) and because of high wall temperature (700 $°C$) leading to high radiation heat transfer, the heating rate is intense. This leads to increase the particle temperature rapidly to reach the saturation status (heat-up process). In this moment, drying starts and the particle temperature remains constant at 100 $°C$. This is shown as steady rate of temperature change with zero value between $10 - 35s$. At the end of drying, the particle temperature rises promptly due to high wall temperature and high heating rate where the pyrolysis starts. During devolatilization the heating rate decreases and it remains almost constant specially between $(60 - 70s)$. In this moment, since the pyrolysis finishes and consequently the oxygen can enter the particle, the temperature of particle rises again and accordingly the heating rate has another jump. The latter is due to the onset of char combustion explained in fig.6.9 as well.

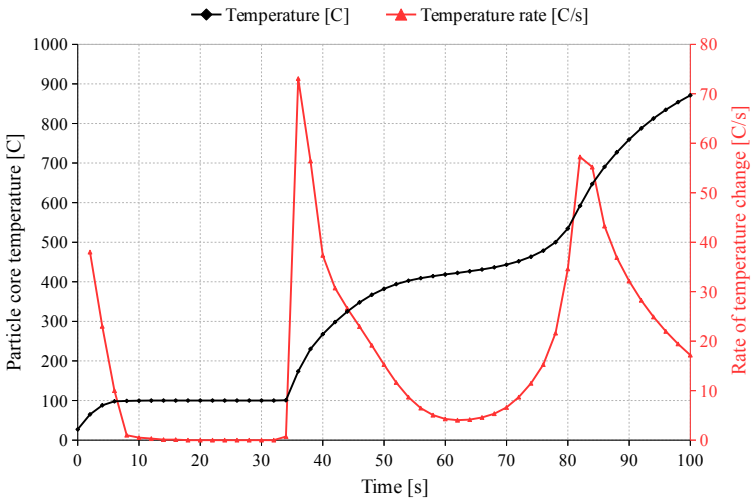

FIGURE 6.7: Particle core temperature and rate of temperature change during conversion with shrinking model for $T_{wall} = 700\ ^{\circ}C$

Moreover, fig.6.8 illustrates the mass fraction of volatile yields during conversion of the cylindrical beechwood particle for $T_{wall} = 700^{\circ}C$. As stated, due to high heating rate at the beginning of simulation, the particle temperature reaches the saturation status rapidly so that drying starts at $t = 6s$. During drying process until around $35s$, the only produced gas is water vapor which comes from the evaporation of water liquid inside the particle due to equilibrium between water vapor and liquid. After drying and then increasing the particle temperature, the pyrolysis begins with delivering the volatiles $CO_2, CO, CH_4, H_2, H_2O$. This stage carries on until end of devolatilization process. Actually, the gas compositions released by the solid fuel are mixed with oxygen and combusted above the particle in the reactor. In addition, the oxygen can go through the particle in this moment. Consequently, these exothermic reactions generate required energy at the end of pyrolysis which leads to minor gasification and combustion of the produced char. However, due to mass transfer of the volatiles and lack of CO_2 and H_2O at the end of pyrolysis, the gasification occur due to reaction with released CO_2 by char combustion. As remarked, since during pyrolysis the produced volatile matters prevent the oxygen to enter the particle, the char combustion takes place slightly after pyrolysis.

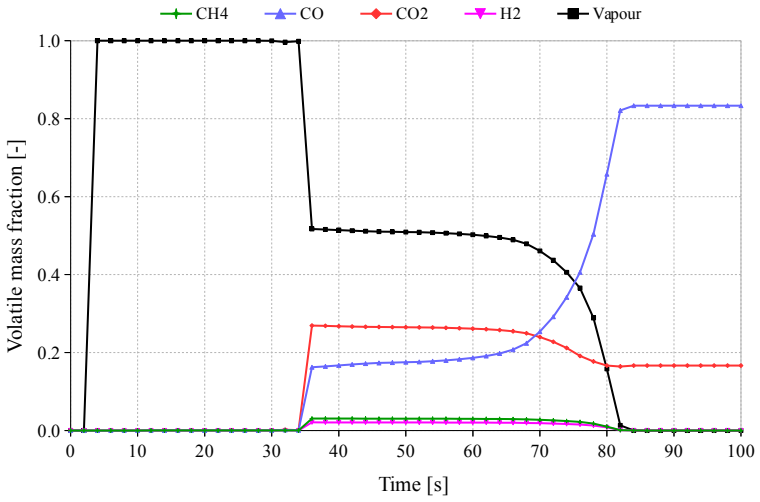

FIGURE 6.8: Mass fraction of volatile yields during conversion with shrinking model for $T_{wall} = 700\ ^{\circ}C$

Furthermore, fig.6.9 demonstrates the performance of solid materials during conversion of the cylindrical beechwood particle for wall temperature $700^{\circ}C$. At the beginning, the solid material is purely beechwood meaning only drying is taking place. When drying finishes, the particle temperature increases and then the beechwood starts to decompose. Since the wood is decomposed to volatiles faster than to char, firstly the gas compositions are generated after $35s$ and then char is formed after $t = 40s$. While the beechwood is consuming, the char is forming until $80s$ and then it is started to convert partially through char combustion with oxygen and char gasification with carbon dioxide.

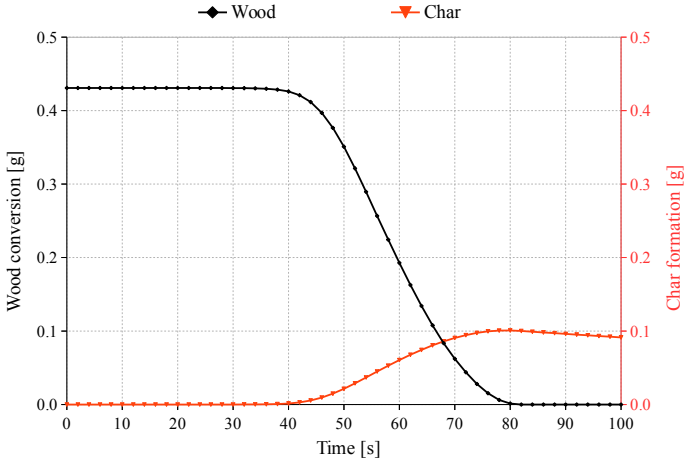

FIGURE 6.9: Wood conversion and char formation during conversion with shrinking for $T_{wall} = 700\ ^{\circ}C$

In addition, fig.6.10 shows the performance of liquid materials during conversion of the cylindrical beechwood particle for wall temperature $700°C$. After heating-up and when drying starts, the water content is reducing due to evaporation until $35s$ where all water liquid is vaporized. Then the pyrolysis commences thereby the tar liquid is formed and due to the mass transfer, it leaves the particle until $80s$. Whereas the whole tar yield is transferred to the reactor and combusted with oxygen above the particle, more carbon monoxide and hydrogen are released in the reactor.

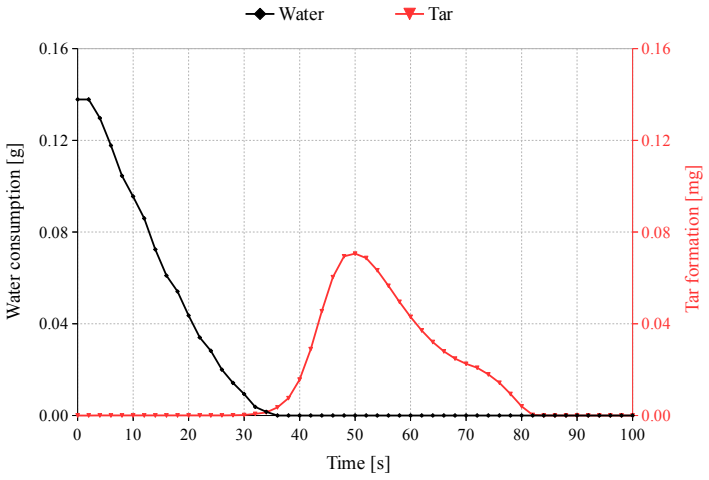

FIGURE 6.10: Water consumption and tar formation during conversion with shrinking for $T_{wall} = 700\ °C$

6.4 Result and discussion

In the reactor studied in this chapter, the aim of fluidization is improving the view factor between the particles and wall so that the particles achieve uniform view factor and uniform radiation heat transfer emitted from the wall. In a fixed bed, interior particles attain lower view factor since they are surrounded by neighbor particles. While in a bubbling fluidized bed, due to continuous motion of particles and position alteration, the particles achieve uniform heat transfer from the wall. However, a bubbling fluidized bed cannot achieve complete char conversion due to the back-mixing of particles. The high degree of solid mixing helps a bubbling fluidized bed gasifier achieve temperature uniformity, but because of intimate mixing of fully and partially gasified particles, any solids leaving the bed contain some partially gasified char. Char particles entrained from a bubbling fluidized bed can also contribute to the loss in a gasifier [1]. So the scope of this part is evaluating the effect of fluidization in a bubbling fluidized bed during conversion of cylindrical beechwood particles. In the defined reactor, the pellets are

transported through a pipe system by gravity and fed with the rate of 1 g/s below the secondary air for 5 s.

In order to compare a fixed bed with a fluidized bed, the idea is giving the same amount of energy from the gas phase ($\dot{Q}_g$) to the particles in both cases according to Eq.6.4. Where the gas flow rate ($\dot{v}_g$) and temperature (T_g) play the main role to estimate the amount of energy given to the particles. It should be mentioned that the variation of gas density (ρ_g), viscosity (μ_g) and specific heat capacity (c_p) according to the temperature change is also considered. For the fixed bed, the volumetric flow rate of primary inlet is kept similar to the single particle case (0.0023 m^3/s), while the gas temperature is increased to $573K$. In order to consider the same heat flow rate while acting the bed to fluidize, the volumetric flow rate of primary inlet is required to be doubled and according to energy estimation by Eq.6.4, the gas temperature is calculated as $400K$. It should be noted that the reason to raise the gas temperature for the fixed bed is if keeping it as ambient temperature, then in the fluidized bed case to provide the same heat flow rate, the gas temperature needed to go below zero value which makes no sense. Tab.6.4 shows the estimated properties of the gas flow for both fixed and fluidized beds.

$$\dot{Q}_g = \rho_g \; c_p \; (\dot{v}_g \; . \; T_g) \tag{6.4}$$

TABLE 6.4: Fixed vs. fluidized bed flow properties

	$\dot{v}_{g,1}(m^3/s)$	$T_g(K)$
Fixed bed	0.0023	573
Fluidized bed	0.0046	400

In order to estimate the behavior of gas phase inside the reactor, a vertical plane is considered. The conversion of pellet particles in the fixed and fluidized bed structure is compared in fig.6.11. The temperature distribution of pellets through the fixed bed in fig.6.11(a) shows that the gradient of temperature is high from the bottom to top of bed ($\Delta T \simeq 330\ ^\circ C$). This is due to the fact that the particles at the lower layers of bed face with the hotter gas leading to more heat transfer rate between solid-gas phases compared to the particles at the top layers. In contrast, because of continuous motion of pellets as a result of drag force by gas flow, the temperature gradient of particles in the fluidized bed configuration shown in fig.6.11(b) is small leading to uniform thermal conversion of materials. This is mentioned as the capability of fluidized beds due to uniform heat transfer rate between the particles and gas phase.

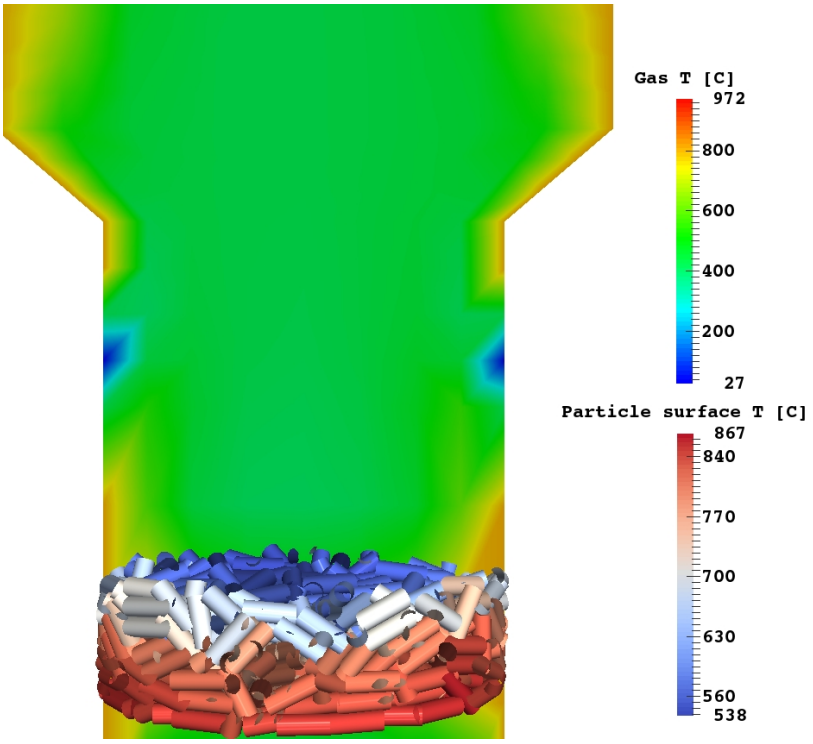

(a) *Conversion of pellets in fixed bed*

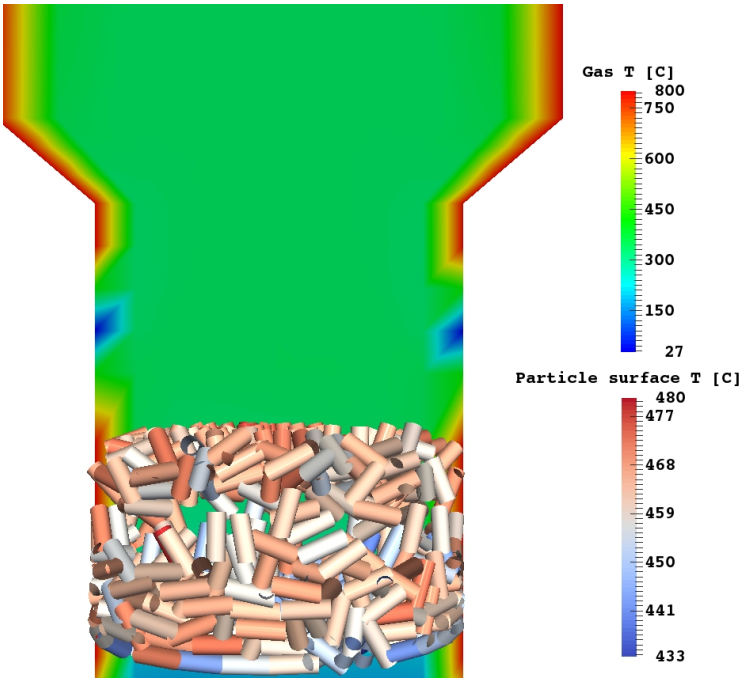

(b) *Conversion of pellets in fluidized bed*

FIGURE 6.11: Temperature distribution of particles and gas flow at $t = 85s$

Additionally in fig.6.12, it can be seen from the temperature distribution in the reactor after 120 s that the combustion zone in gas phase is located above the bed. Where the displacement of flame is essentially affected by the secondary air distribution around the circumference of the reactor. Thus, the secondary air conducts the gaseous flame to the middle of freeboard.

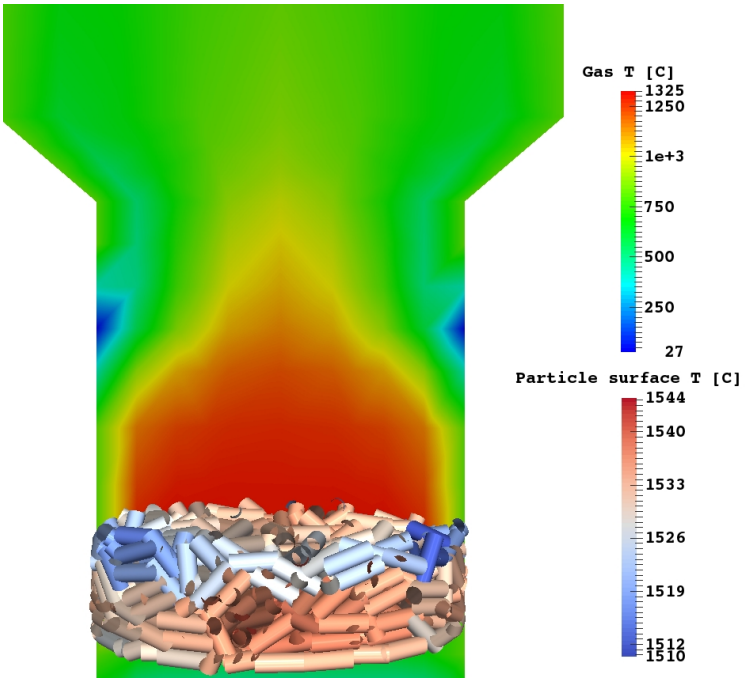

FIGURE 6.12: Ignition in the fixed bed at $t = 120s$

6.5 Conclusion

The aim of this chapter is estimating the conversion behavior of biomass in a bubbling fluidized bed reactor. Where the conversion process is investigated by employing the proposed DEM-CFD approach, and validated via comparison with experimental data for a single particle from literature. Since the wood particles have layered behavior like an insulator, the suitable models are either slab or cylinder where the latter is considered for the studied particles. In addition, a shrinking model is applied to evaluate the effect of shrinkage during conversion. The model is based on the rate of wood and char consumption and the results show an improvement in the predictions. It is illustrated that the conversion process is referred to four stages which take place sequentially. In the first stage, the particle is heated up until reaching the saturation status. Then drying starts where the particle temperature remains constant. After finishing the moisture content inside the particle, while the temperature rises, the particle is decomposed thermally to solid char, liquid tar and volatile matters. According to mass transfer between solid-gas phases, tar and volatiles are exited from the particle and combusted with oxygen in the gas phase above the particle. At the end of pyrolysis, the gasification and combustion commence where the released carbon dioxide from combusted volatiles as well as oxygen react with the remaining char. Then the successful approach is applied to compare the behavior of biomass conversion in a fixed and a fluidize bed. The intention is giving the same heat flow rate to both cases. While in the fixed bed, the inlet gas has high temperature with low volumetric flow rate; in the fluidized bed the volumetric flow rate is relatively higher to fluidize the bed with respect to rather low temperature than the fixed bed. Hence, in both fixed and fluidized beds, the achieved heat flow rate by particles are equivalent. The comparative predictions between the fixed and fluidized bed configurations show that temperature gradient of pellets in fixed bed is much higher than fluidized bed formation as expected. This is due to the fact that motion of particles in the system leads to uniform heat transfer rate to the pellets which results the uniform temperature between particles through the bed. At the end, the ignition owing to combustion of conversion yields is shown graphically where the gaseous flame is directed to the middle of system due to influence of the secondary air distribution around the circumference of reactor.

Chapter 7

Conclusions

Since experimental work is highly expensive and time-consuming, the numerical modeling would be a powerful tool to find out the complex phenomena inside the reactors used in industry. In this doctoral thesis, a four-way DEM-CFD coupling approach called eXtended Discrete Element Method is developed and applied to simulate the drying and conversion of biomass materials. The proposed model, that includes three different modules, is originally based on the classical Discrete Particle Method (DPM) which deals with the motion of particles specified as the dynamics module. In addition, the conversion module considers the thermodynamic state inside the particle and evaluates the temperature and species distributions within the particle. The surrounding gas phase is estimated as a continuous phase with employing OpenFOAM source code as the CFD module which is coupled via heat, mass and momentum transfer to the particles. In XDEM, the solid phase is considered as discrete, while the gas flow is treated as continuum phase in the void space of the particles. Therefore, this approach is termed as Combined Continuum and Discrete Model (CCDM). In order to describe the processes within a particle, a set of differential conservation equations are applied to mass, momentum, energy and species transfer to both solid-gas phase within a particle. That is, the conservation equations for mass, momentum, energy and species are resolved to determine radial distributions of gaseous and solid species concentration and temperature, as well as gas pressure and velocity versus time. The gas phase is assumed as an ideal gas inside the pore volume of solid phase which is transported via convection and diffusion and it can exchange mass and heat with the solid phase. Thermal equilibrium between solid-gaseous phase is assumed within the pore space of the solid and for energy conservation a homogeneous model is applied. Whereby, the implementation of the heat, mass, momentum and species transfer is verified by conducting experimental tests and subsequent comparison between the numerical and experimental results that reveals an appropriate agreement. Therefore, XDEM is termed as a powerful numerical tool to

deal with the multiphase systems including dynamics and conversion of particles within a surrounding gas phase, thereby it is applied in various types of applications including heat-up, drying, pyrolysis, combustion and gasification in this work.

In Chapter.1, it is remarked the importance of biomass solid fuels as an economical and ecological source of renewable energy; and an affordable alternative to fossil fuels. In Chapter.2, the proposed DEM-CFD coupling is described through conservation equations of mass, energy, momentum and species transfer in both solid-gas phase including the interfaces in between. The latter is mentioned as heat, mass and momentum transfer between the particles and surrounding gas. Afterwards, with employing the proposed model, four different applications are considered in the next four chapters. Where in Chapter.3, the drying process including the influence of particle size distribution is investigated in a rotary drum. Also in Chapter.4, the drying process of wood materials in a vibrating fluidized bed dryer is investigated in industrial scale where the experimental work is performed through a collaboration with Soil-Concept company located in Diekirch, Luxembourg. The subject of Chapter.5 is evaluating the hydrodynamic behavior of a packed bed of particles within the gaseous phase inside a bubbling fluidized bed. In this case, the experimental data is achieved via cooperation with a laboratory of Dresden University, Germany. The last studied case is defined in Chapter.6 that investigates the conversion of woody biomass inside a fluidized bed. The conversion is denoted as accomplishing the heat-up, drying, pyrolysis, gasification and combustion processes sequentially where the essential homogeneous and heterogeneous reactions between the particles and gas phase are taken into account.

Thermal treatment of biomass refers to the conversion of biomass when the essential heat is available in the system. In this case, some physical and chemical processes shown in Figure 7.1 as heat-up, drying, pyrolysis, combustion and gasification take place. Heat-up is warming biomass to increase the temperature above the ambient temperature. When the surface temperature of biomass reaches the saturation status (around $100°C$ in $1bar$), the water contents of biomass start to vaporize whereby the drying process begins. After removing the water content and with increasing heat, the biomass starts to decompose thermally to solid char, liquid tar and volatile gases ($CH_4, CO, CO_2, H_2, H_2O$). This stage is pyrolysis or devolatilization process. The released heat from reactions between the volatile gases and oxygen is used for drying and pyrolysis of new feeding biomass fuel to the reactor and producing further volatiles so that this cycle continues as far as the oxygen is provided to the system. The remaining char from thermal decomposition is gasified via reacting with CO_2 and H_2O to generate useful gases of CO and H_2 which are highly combustible. Also char is oxidized at high temperature above $700°C$ denoting the combustion process when the solid char reacts with oxygen. [1]

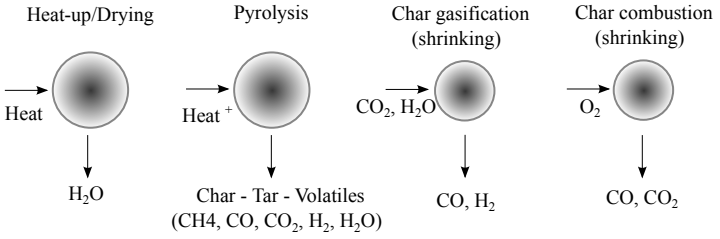

FIGURE 7.1: Main steps of conversion process

Here the XDEM model is applied to validate the drying of a single particle with the experiment carried out by Looi et al. [2]. The particle is considered as a spherical wet particle including 60 % of moisture content and diameters $10, 12\ mm$ defined as cases **A** and **B**. The experiments are performed at the pressure of 2.4 bar, and the superheated steam temperature at $170°C$, as well as the steam velocity at 2.7 m/s. The prediction of particle core temperature by XDEM model compared to experiment is shown in Figure 7.2. In case **A**, the temperature rises from saturation after 20 s while in case **B** it rises after 27 s which states that the small particle is dried faster. The reason is in the small particle, heat transfer from the surface to core of particle is faster. However, the temperature of particles in both cases reaches the gas temperature ($170°C$) at the end of drying. In addition, Figure 7.3 shows the behavior of drying rate based on the moisture content for case **B**. The AB part on the curve represents a warming-up period of the particle. The BC part is the constant-rate period where the particle temperature is constant during this period since heat transfer into the surface

is constant and the heat is consumed just for water evaporation. When the free water is finished, the temperature starts to rise. This point is shown as point C, where the constant-rate ends and the drying rate begins falling that is termed the critical-moisture content. The curved portion CD is termed the falling-rate period and is typified by a continuously changing rate throughout the remainder of the drying cycle. It is also shown the prediction of moisture content of the particle compared to the experiment. In total, the prediction by XDEM simulation is in good agreement with the experiment. [3]

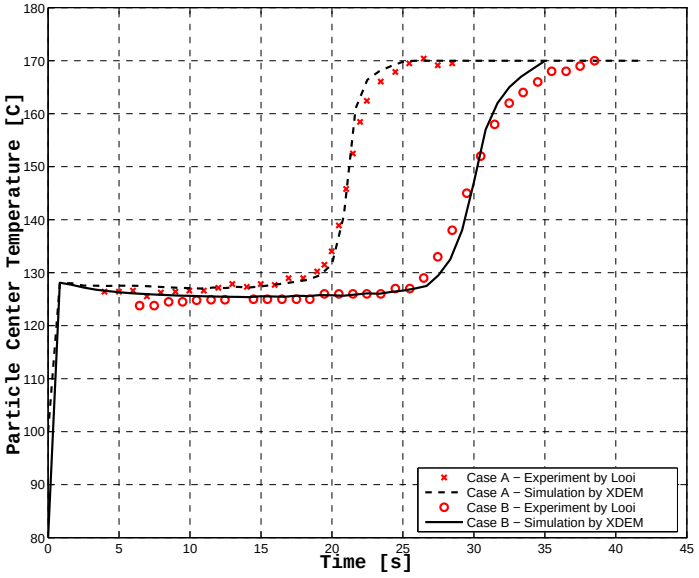

FIGURE 7.2: Particle size effect on drying of a coal particle— Case A: $d_p = 10mm$, $P = 2.4bar$, $T_a = 170°C$, $v_g = 2.7m/s$; Case B: $d_p = 12mm$, $P = 2.4bar$, $T_a = 170°C$, $v_a = 2.7m/s$

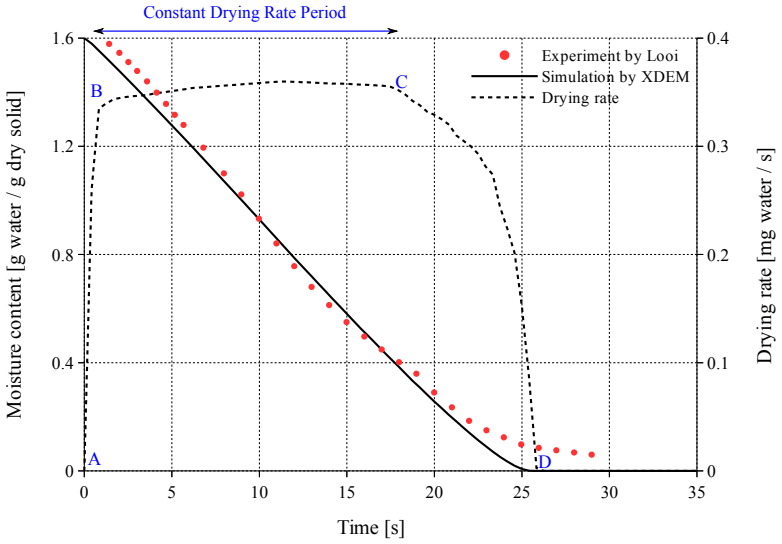

FIGURE 7.3: Drying rate and moisture content vs. time— case **B**: $d_p = 12mm$, $P = 2.4bar$, $T_a = 170°C$, $v_g = 2.7m/s$

Bibliography

[1] Mohammad Mohseni. *Drying and Conversion Analysis of Biomass by a DEM-CFD Coupling Approach.* PhD thesis, University of Luxembourg, Luxembourg, 2017.

[2] A.Y. Looi, K. Golonka, and M. Rhodes. Drying kinetics of single porous particles in superheated steam under pressure. *Chemical Engineering Journal*, 87:329–338, 2002.

[3] Mohammad Mohseni and Bernhard Peters. Effects of particle size distribution on drying characteristics in a drum by xdem: A case study. *Chemical Engineering Science*, 152:689–689, 2016.

Appendix A

Appendices

A.1 PaSR combustion model

In this work to describe the turbulence/chemistry interaction, the Partially Stirred Reactor concept (PaSR) is used. In PaSR model, it is assumed that the flames are much thinner than any computational cell meaning any cell could be considered as a perfect reactor. Thus, every computational cell is separated into two different zones where in one zone all reactions occur, while in the other one no reaction takes place. So in the reacting zone the mass exchange causes the composition change. It should be noted that Perfectly Stirred Reactor (PSR) is considered in the reacting zone where the composition is homogeneous. Generally, PaSR states that the concentration of specie i at the reactor output could be written as:

$$c_1^i = k^* c^i \ + \ (1 - k^*) c_0^i \tag{A.1}$$

where c_1^i is a linear interpolation between c^i and c_0^i; k^* is the mass fraction of the reacting mixture. In PaSR three molar concentrations are distinguished as could be seen in Fig.A.1.

- c_0^i : initial averaged concentration of specie i entering to the cell
- c^i : unknown concentration of specie i in the reacting zone at any time
- c_1^i : output averaged concentration of specie i exiting from the cell

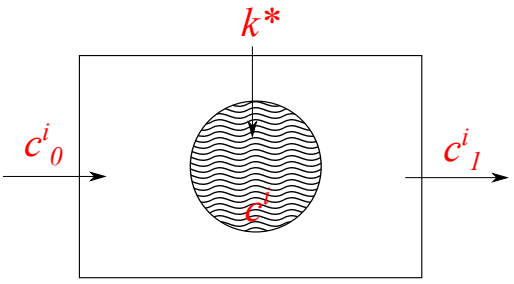

FIGURE A.1: Conceptual view of Partially Stirred Reactor

The chemical combustion process using PaSR is modeled with splitting into sub-steps which take place simultaneously as:

(i) The initial concentration c_0^i changes to c^i in the reacting zone

(ii) The reactive concentration c^i is mixed via turbulence with c_0^i leading to the averaged concentration c_1^i

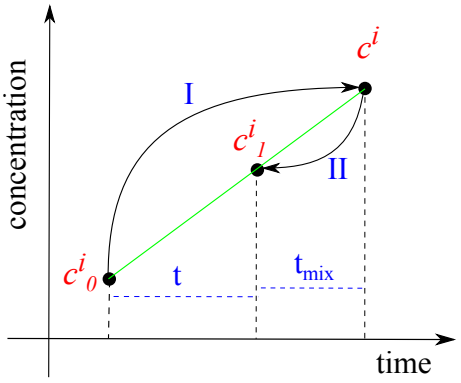

FIGURE A.2: Reaction-Mixing stages

Where t is the integration step time between c_0^i and c_1^i and t_{mix} is the turbulence characteristic time which is the time to mix c^i with c_0^i. In the reaction-mixing stages shown in Fig.A.2, it is assumed that the slope of the curve (the green line) expresses the reaction rate in the reacting zone, then we can write the reaction rate of specie i in numerical time step of t as $f(c^i)$:

$$f(c^i) = \frac{c_1^i - c_0^i}{t} = \frac{c^i - c_1^i}{t_{mix}}; \quad k^* = \frac{t}{t + t_{mix}} \tag{A.2}$$

This is so important to mention that the reaction rate term appears in the species transport equation added to the chemical source term. With performing the Taylor expansion on the reaction rate of $f(c^i)$:

$$f(c^i) = f(c_1^i) + \frac{\delta f}{\delta c}\Big|_{c=c_1^i}(c^i - c_1^i) \tag{A.3}$$

and $\frac{\delta f}{\delta c}$ is reciprocal of the chemical time scale (t_c) and could be written as:

$$\frac{\delta f}{\delta c}|_{c=c_1^i} = \frac{\dot{w}(c_1^i) - \dot{w}(c_0^i)}{c_1^i - c_0^i} = -\frac{1}{t_c} \tag{A.4}$$

where $\dot{w}(c_0^i)$ and $\dot{w}(c_1^i)$ are the reaction rate of specie i at the beginning and at the end of the time step. Then we can write Eq.A.3 as:

$$f(c^i) = f(c_1^i) - \frac{c^i - c_1^i}{\tau_c} \tag{A.5}$$

with using the chemical time scale (t_c) in Eq.A.2, we can write the reaction rate and rate coefficient as:

$$\frac{c_1^i - c_0^i}{t} = \frac{t_c}{t_c + \tau_{mix}} f_m(c_1^i) \; ; \quad k_i = \frac{t_c}{t_c + t_{mix}} \tag{A.6}$$

so that the turbulent mixing time t_{mix} could be written as:

$$t_{mix} = C_{mix}\sqrt{\frac{\mu_{eff}}{\rho\varepsilon}} \tag{A.7}$$

where C_{mix} is the mixing coefficient and could be defined based on turbulence scales as:

$$t_{mix} = \sqrt{\frac{k}{\varepsilon}(\frac{\nu}{\varepsilon})^{1/2}} \tag{A.8}$$

and with equalizing Eq.A.7 and Eq.A.8, the mixing coefficient is written as:

$$C_{mix} = \sqrt{\frac{1}{1 + C_\mu Re_t}} \tag{A.9}$$

where

$$\frac{\mu_t}{\rho} = C_\mu \frac{k}{\varepsilon};\ Sc_t = 1;\ Re_t = \frac{k^2}{\varepsilon\nu} \tag{A.10}$$

Therefore, according to the turbulent Reynolds number, the mixing coefficient could be estimated as follows.

- Laminar flow $Re_t = 0 \Rightarrow C_{mix} = 1$
- Typical turbulent flow $Re_t \simeq 1000 \Rightarrow C_{mix} \simeq 0.1$
- Extremely turbulent flow $Re_t \simeq \infty \Rightarrow C_{mix} \simeq 0$

Bibliography

[1] Prabir Basu. *Biomass Gasification and Pyrolysis*. Academic Press Elsevier, 2010.

[2] International Energy Outlook 2016. https://www.eia.gov/outlooks/ieo/. Report Number: DOE/EIA-0484(2016).

[3] A. E. Ghaly and K. N. MacDonald. mixing pattrens and residence time determination in a bubbling fluidized bed system. *American Journal of Engineering and Applied Sciences*, 5 (2):170–183, 2012.

[4] A. Faghri and Y. Zhang. *Transport Phenomena in Multiphase Systems*. Elsevier Academic Press, 2010.

[5] J. Sun, F. Battaglia, and S. Subramaniam. Hybrid two-fluid dem simulation of gas-solid fluidized beds. *Fluids Engineering*, 129:1394–1403, 2007.

[6] B. G. M. van Wachem, J. C. Schouten, and C. M. van den Bleek. Cfd modeling of gas-fluidized beds with a bimodal particle mixture. *AIChE Journal*, 47:1292–1302, 2001.

[7] Madhava Syamlal and William Rogers Thomas J. O'Brien. Mfix documentation: Theory guide. Technical report, U.S. Department of Energy, 1993.

[8] S. Deb and D. K. Tafti. Two and three dimensional modeling of fluidized bed with multiplejets in a dem–cfd framework. *Particuology*, 16:19–28, 2014.

[9] M. Weng and J. Plackmeyer. Comparison between measurements and numerical simulation of particle flow and combustion at the duisburg cfbc plant. In *10th International Conference on Circulating Fluidized Beds and Fluidization Technology - CFB-10*, 2011.

[10] Heng Xiao and Jin Sun. Algorithms in a robust hybrid cfd-dem solver for particle-laden flows. *Communications in Computational Physics*, 9:297–323, 2011.

[11] P. A. Cundall and O. D. L. Strack. A discrete numerical model for granular assemblies. *Geotecgnique*, 29:47–65, 1979.

[12] Y. H. Man and R. C. Byeong. A numerical study on the combustion of a single carbon particle entrained in a steady flow. *Combustion and Flame Journal*, 97: 1–16, 1994.

[13] A. H. Mahmoudi, F. Hoffmann, and B. Peters. Application of xdem as a novel approach to predict drying of a packed bed. *International Journal of Thermal Sciences*, 75:65–75, 2014.

[14] Donald A. Nield and Adrian Bejan. *Convection in Porous Media*. Springer, 2006.

[15] K. D. Kafui, C. Thornton, and M. J. Adams. Discrete particle-continuum fuid modelling of gas–solid fuidised beds. *Chemical Engineering Science*, 57:2395–2410, 2002.

[16] A. Mahmoudi, M. Markovic, B. Peters, and G. Brem. An experimental and numerical study of wood combustion in a fixed bed using euler–lagrange approach (xdem). *Fuel*, 150:573–582, 2015.

[17] M. Sakai, H. Takahashi, C. Pain, J. Latham, and J. Xiang. Study on a large-scale discrete element model for fine particles in a fluidized bed. *Advanced Powder Technology*, 23:673–681, 2012.

[18] Mikio Sakai, M. Abe, Y. Shigeto, S. Mizutani, H. Takahashi, A. Vire, J. Percival, J. Xiang, and C Pain. Verification and validation of a coarse grain model of the dem in a bubbling fluidized bed. *Chemical Engineering Journal*, 244:33–43, 2014.

[19] W. Zhong, A. Yu, X. Liu, Z. Tong, and H. Zhang. Dem/cfd-dem modelling of non-spherical particulate systems: Theoretical developments and applications. *Powder Technology*, 302:108–152, 2016.

[20] K. Chu, J. Chen, and A. Yu. Applicability of a coarse-grained cfd–dem model on dense medium cyclone. *Minerals Engineering*, 90:43–54, 2016.

[21] Z. Tong, W. Zhong, A. Yu, H. Chan, and R. Yang. Cfd–dem investigation of the effect of agglomerate–agglomerate collision on dry powder aerosolisation. *Journal of Aerosol Science*, 92:109–121, 2016.

[22] H. Xu, W. Zhong, Z. Yuan, and A. Yu. Cfd-dem study on cohesive particles in a spouted bed. *Powder Technology*, 2016. http://dx.doi.org/10.1016/j.powtec.2016.09.006.

[23] A.E. Carlos Varas, E.A.J.F. Peters, and J.A.M. Kuipers. Cfd-dem simulations and experimental validation of clustering phenomena and riser hydrodynamics. *Chemical Engineering Science*, In Press. http://dx.doi.org/10.1016/j.ces.2016.08.030.

[24] A.V. Patil, E.A.J.F. Peters, and J.A.M. Kuipers. Comparison of cfd–dem heat transfer simulations with infrared-visual measurements. *Chemical Engineering Journal*, 277:388–401, 2015.

[25] V. Salikov, S. Antonyuk, S. Heinrich, V. S. Sutkar, N. G. Deen, and J.A.M. Kuipers. Characterization and cfd-dem modelling of a prismatic spouted bed. *Powder Technology*, 270:622–636, 2015.

[26] V. S. Sutkar, N. G. Deen, A. V. Patil, V. Salikov, S. Antonyuk, S. Heinrich, and J.A.M. Kuipers. Cfd–dem model for coupled heat and mass transfer in a spout fluidized bed with liquid injection. *Chemical Engineering Journal*, 288:185–197, 2016.

[27] H. Hertz. Über die Berührung fester elastischer Körper. *Journal für die reine und angewandte Mathematik*, 92:156–171, 1881.

[28] Kasra Samiei. *Assessment of implicit and explicit algorithms in numerical simulation of granular matter*. PhD thesis, University of Luxembourg, 2012.

[29] T. Ishida Y. Tsuji, T. Tanaka. Lagrangian numerical simulation of plug flow of cohesionless particles in a horizontal pipe. *Powder Technology*, 71:239–250, September 1992.

[30] D. Zhang and W.J. Whitten. The calculation of contact forces between particle using spring and damping models. *Powder Technology*, 88:59–64, 1996.

[31] Y. Tsuji, T. Kawaguchi, and T. Tanaka. Discrete particle simulation of two-dimensional fluidized bed. *Powder Technology*, 77:79–87, 1993.

[32] J. Hager, M. Hermansson, and R. Wimmerstedt. Modelling steam drying of a single porous ceramic sphere experiments and simulations. *Chemical Engineering Science*, 52:1253–1264, 1997.

[33] M. Bellais. *Modelling of the pyrolysis of large wood particles*. PhD thesis, Royal Institute of Technology (KTH), 2007.

[34] M. Gronli. *A Theoretical and Experimental Study of the Thermal Degradation of Biomass*. PhD thesis, The Norwegian University of Science and Technology, 1996.

[35] B. Peters, A. Džiugys, and R. Navakas. Simulation of thermal conversion of solid fuel by the discrete particle method. *Lithuanian Journal of Physics*, 51:91–105, 2011.

[36] Mohammad Mohseni and Bernhard Peters. Effects of particle size distribution on drying characteristics in a drum by xdem: A case study. *Chemical Engineering Science*, 152:689–698, 2016.

[37] R.B. Bird, W.E. Stewart, and E.N. Lightfoot. *Transport Phenomena*. John Wiley & Sons, 1960.

[38] W. Du, X. Bao, J. Xu, and W. Wei. Computational fluid dynamics (cfd) modeling of spouted bed: Assessment of drag coefficient correlations. *Chemical Engineering Science*, 61:1401–1420, 2006.

[39] Dimitry Gidaspow. *Multiphase Flow and Fluidization; Continuum and Kinetic Theory Descriptions*. Academic Press, 1994.

[40] C. D. Blasi. 45 dynamic behaviour of stratified downdraft gasifiers. *Chemical Engineering Science*, 55:2931–2944, 2000.

[41] J. Wiese, F. Wissing, D. Hohner, S. Wirtz, V. Scherer, U. Ley, and H. M. Behr. Dem/cfd modeling of the fuel conversion in a pellet stove. *Fuel Processing Technology*, 152:223–239, 2016.

[42] R. Johansson, H. Thunman, and B. Leckner. Influence of intraparticle gradients in modeling of fixed bed combustion. *Combustion and Flame*, 149:49–62, 2007.

[43] D. D. Evans and H. W. Emmons. Combustion of wood charcoal. *Fire Safety Journal*, 1(1):57–66, March 1977.

[44] C. D. Blasi and C. Branca. Kinetics of primary product formation from wood pyrolysis. *Ind. Eng. Chem. Res.*, 40:5547–5556, 2001.

[45] G. Groppi, E. Tronconi, P. Forzatti, and M. Berg. Mathematical modelling of catalytic combustors fuelled by gasified biomasses. *Catalysis Today*, 59:151–162, 2000.

[46] Kenneth M. Bryden and Kenneth W. Ragland. Numerical modeling of a deep, fixed bed combustor. *Energy and Fuels*, 10:269–275, 1996.

[47] Arun S. Mujumdar. *Handbook of Industrial Drying 4th Ed.* CRS Press, 2006.

[48] L. Fagernas, J. Brammer, C. Wilen, M. Lauer, and F. Verhoeff. Drying of biomass for second generation synfuel production. *biomass and bioenergy*, 34:1267–1277, 2010.

[49] E. Achenbach. Heat and flow characteristics of packed beds, review. *Experimental Thermal and Fluid Science*, 10:17–27, 1995.

[50] L.K. Stroem, D.K. Desai, and A.F.A. Hoadley. Superheated steam drying of brewer's spent grain in a rotary drum. *Advanced Powder Technology*, 20:240–244, 2009.

[51] L. Fagernas. Drying of biomass for second generation synfuel production. *Biomass and Bioenergy*, 34:1267–1277, 2010.

[52] Hugo Perazzini, Fabio Bentes Freire, and Jose Teixeira Freire. Prediction of residence time distribution of solid wastes in a rotary dryer. *Drying Technology*, 32: 428–436, 2014.

[53] W.L. McCabe, J.C. Smith, and P. Harriott. *Unit Operations of Chemical Engineering 4th Ed.* McGraw-Hill, New York, 1987.

[54] F. T. Ademiluyi, M. F. N. Abowei, Y. T. Puyate, and S. C. Achinewhu. Effects of drying parameters on heat transfer during drying of fermented ground cassava in a rotary dryer. *Drying Technology*, 28:550–561, 2010.

[55] H. Abbasfard, H. H. Rafsanjani, S. Ghader, and M. Ghanbari. Mathematical modeling and simulation of an industrial rotary dryer: A case study of ammonium nitrate plant. *Powder Technology*, 239:499–505, 2013.

[56] Q. Xu and S. Pang. Mathematical modeling of rotary drying of woody biomass. *Drying Technology*, 26:1344–1350, 2008.

[57] A. Iguaz, A. Esnoz, G. Martinez, A. Lopez, and P. Virseda. Mathematical modelling and simulation for the drying process of vegetable wholesale by-products in a rotary dryer. *Journal of Food Engineering*, 59:151–160, 2003.

[58] P. Johnson, J. Paliwal, and S. Cenkowski. Analysing the effect of particle size on the disintegration of distiller's spent grain compacts while drying in superheated steam medium. *Biosystems Engineering*, 134:105–116, 2015.

[59] F. Castano, F. R. Rubio, and M. G. Ortega. Modeling of a cocurrent rotary dryer. *Drying Technology*, 30:839–849, 2012.

[60] A.Y. Looi, K. Golonka, and M. Rhodes. Drying kinetics of single porous particles in superheated steam under pressure. *Chemical Engineering Journal*, 87:329–338, 2002.

[61] Robert H. Perry. *Perry's Chemical Engineers Handbook.* McGraw-Hill, 1997.

[62] Joaquin Martinez and Apolinar Picado. Mathematical modeling of continuous vibrating fluidized bed dryer for grain. *Drying Technology*, 30:1469–1481, 2012.

[63] Milan Stakic and Tijana Urosevic. Experimental study and simulation of vibrated fluidized bed drying. *Chemical Engineering and Processing: Process Intensification*, 50:428–437, 2011.

[64] M. Syamlal and T. J. O'Brien. The derivation of a drag coefficient formula from velocity-voidage correlations. Unpublished report, April 1987.

[65] J. F. Richardson and W. N. Zaki. Sedimentation and fluidization: Part i. *Trans. Inst. Chem. Eng.*, 32:35–53, 1954.

[66] R. Di Felice. The voidage function for fluid-particle interaction systems. *International Journal of Multiphase Flow*, 20:153–159, 1994.

[67] H. Arastoopour, P. Pakdel, and M. Adewumi. Hydrodynamic analysis of dilute gas-solids flow in a vertical pipe. *Powder Technology*, 62:163–170, 1990.

[68] A. Rao, J. S. Curtis, B. C. Hancock, and C. Wassgren. The effect of column diameter and bed heighton minimum fluidization velocity. *AIChE Journal*, 56(9):2304–2311, 2010.

[69] F. P. Incropera, D. P. Dewitt, T. L. Bergman, and A. S. Lavine. *Fundamentals of heat and mass transfer*. John Wiley and Sons, 2007.

[70] Roland B. Stull. *An Introduction to Boundary Layer Meteorology*. Kluwer Academic Publishers, first edition, 1988.

[71] J. Solsvik, Z. Chao, R. A. Sanchez, and H. A. Jakobsen. Numerical investigation of steam methane reforming with co2-capture in bubbling fluidized bed reactors. *Fuel Processing Technology*, 125:290–300, 2014.

[72] A. Tremel and H. Spliethoff. Gasification kinetics during entrained flow gasification – part i; devolatilisation and char deactivation. *Fuel*, 103:663–671, 2013.

[73] D. Baruah and D.C. Baruah. Modeling of biomass gasification: A review. *Renewable and Sustainable Energy Reviews*, 39:806–815, 2014.

[74] B.V. Babu and P. N. Sheth. Modeling and simulation of reduction zone of downdraft biomass gasifier: Effect of char reactivity factor. *Energy Conversion and Management*, 47:2602, 2611 2006.

[75] A. Melgar, J. F. Perez, H. Laget, and A. Horillo. Thermochemical equilibrium modelling of a gasifying process. *Energy Conversion and Management*, 48:59–67, 2007.

[76] N. Gao and A. Li. Modeling and simulation of combined pyrolysis and reduction zone for a downdraft biomass gasifier. *Energy Conversion and Management*, 49: 3483–3490, 2008.

[77] E. Azzone, M. Morini, and M. Pinelli. Development of an equilibrium model for the simulation of thermochemical gasification and application to agricultural residues. *Renewable Energy*, 46:248–254, 2012.

[78] G. Lu, J.R. Third, and C.R. Müller. Discrete element models for non-spherical particle systems: From theoretical developments to applications. *Chemical Engineering Science*, 127:425–465, 2015.

[79] Wenqi Zhong, Aibing Yu, Xuejiao Liu, Zhenbo Tong, and Hao Zhang. Dem/cfd-dem modelling of non-spherical particulate systems: Theoretical developments and applications. *Powder Technology*, 302:108–152, 2016.

[80] A. Dziugys and B. Peters. A new approach to detect the contact of two-dimensional elliptical particles. *International Journal for Numerical and Analytical Methods in Geomechanics*, 45:1487–1500, 2001.

[81] G.T. Nolan and P.E. Kavanagh. Random packing of nonspherical particles. *Powder Technology*, 84:199–205, 1995.

[82] B. Peters, A. Džiugys, and R. Navakas. A shrinking model for combustion/gasification of char based on transport and reaction time scales. *MECHANIKA*, 18(2): 177–185, 2012.

[83] N. Wakao and S. Kaguei. *Heat And Mass Transfer In Packed Beds*. Gordon and Breach Science Publishers, New York, NY, 364, 1982.